2013

ACCOMPLISHMENTS *and* OPPORTUNITIES

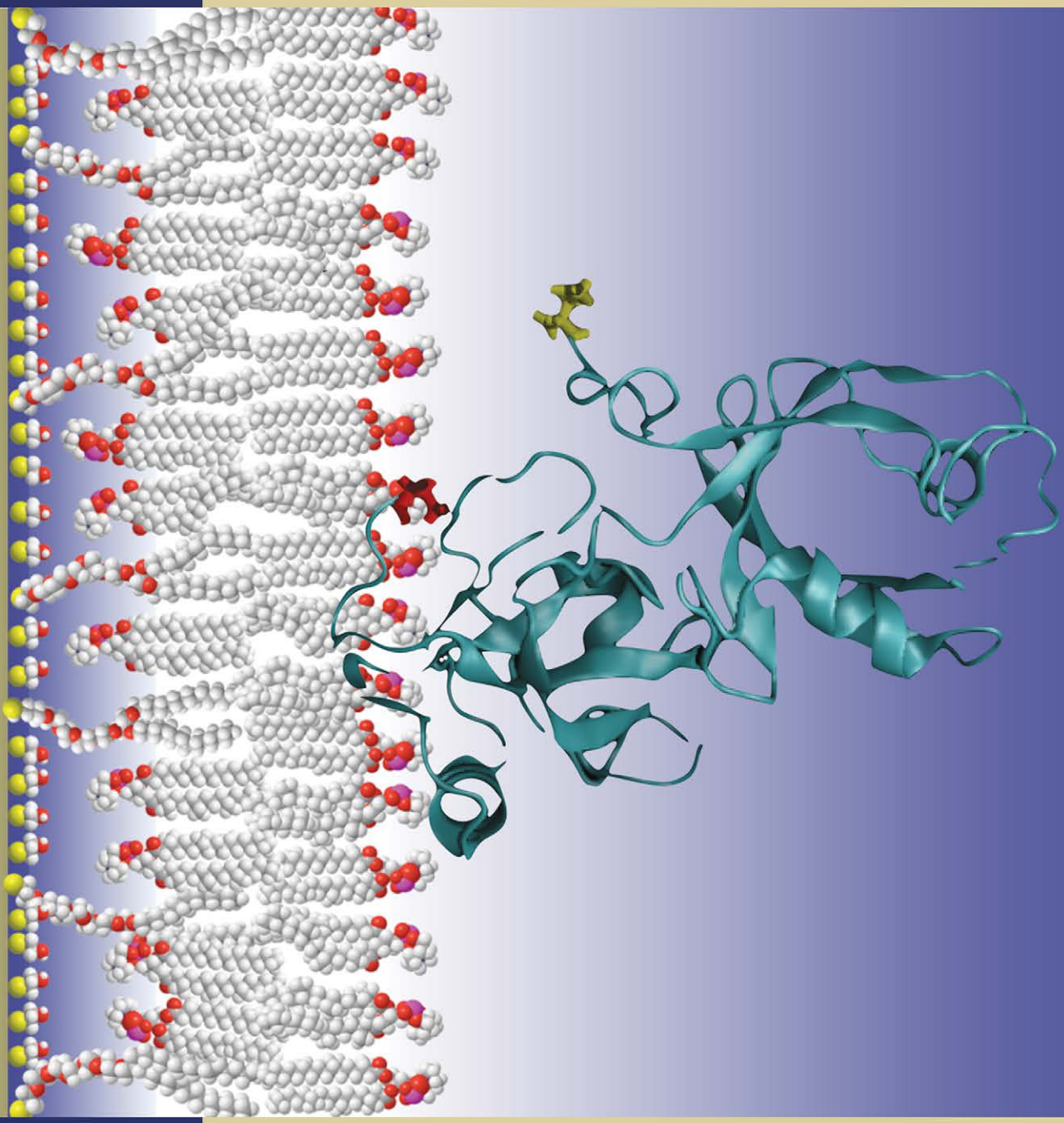

NIST CENTER FOR NEUTRON RESEARCH

NIST

National Institute of Standards and Technology
U.S. Department of Commerce

NIST SP 1168

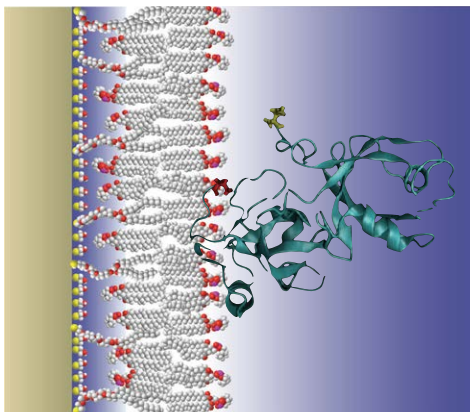

ON THE COVER

The penetration depth and orientation of a single myristoylated GRASP protein bound to a lipid membrane as determined by neutron reflectometry. See the highlight article by Zan *et al.* on p.12.

2013 Accomplishments and Opportunities

NIST Special Publication 1168

Robert M. Dimeo, Director

Steven R. Kline, Editor

December 2013

National Institute of Standards and Technology
Patrick Gallagher, Under Secretary of Commerce
for Standards and Technology and Director

U.S. Department of Commerce
Penny Pritzker, Secretary

DISCLAIMER

Certain commercial entities, equipment, or materials may be identified in this document in order to describe an experimental procedure or concept adequately. Such identification is not intended to imply recommendation or endorsement by the National Institute of Standards and Technology, nor is it intended to imply that the entities, materials, or equipment are necessarily the best available for the purpose.

National Institute of Standards and Technology
Special Publications 1168

Natl. Inst. Stand. Technol. Spec. Publ. 1168, 84 pages
(December 2013)

http://dx.doi.org/10.6028/NIST.SP.1168
CODEN: NSPUE2

U.S. GOVERNMENT PRINTING OFFICE-
WASHINGTON: 2013

For sale by the Superintendent of Documents,
U.S. Government Printing Office

Internet: bookstore.gpo.gov
Phone: 1.866.512.1800
Fax: 202.512.2104
Mail: Stop SSOP
Washington, DC 20402-0001

Table of Contents

Table of Contents

Foreword

I am pleased to present this year's annual report for the NIST Center for Neutron Research. This year marked the first full year of reactor operations since the facility outage that was completed in 2012. The combination of robust user operations and facility developments contributed to a highly productive year. The reactor operated for 238 days out of a scheduled 240 days in FY2013. In past years I have reported the operational reliability of *the* cold source. However, in addition to the cold source that now serves 12 neutron guides, this year we began operations of the new cold source that serves the MACS spectrometer. I am pleased to report that *both* cold sources operated reliably and delivered neutrons 99 % of the scheduled operating time. The long tradition of the reliable operations of the reactor source and cold neutron source have been key factors in the scientific productivity of the NCNR. In fact, the American Nuclear Society recently recognized the NCNR with the Nuclear Historic Landmark Award *for the development of the first internationally competitive user facility for cold neutron research in the USA*.

This was an extremely active year for facility developments. In this year alone the new 10 meter SANS instrument was installed and commissioned on a new neutron guide, becoming operational and supporting nSoft consortium users. The upgraded MACS instrument was installed on a beamport with its own dedicated cold neutron source, commencing user operations and performing as predicted. The new Prompt Gamma Activation Analysis instrument was installed on a new neutron guide. The Neutron Spin-Echo instrument is being relocated to the guide hall extension where it will be much further away from high magnetic field experiments and can operate more robustly. We have taken advantage of this move to improve the neutron polarizer and upgrade the power supplies. You can read more details about these facility enhancements in this report.

Finally, the result of our facility operations is in the research carried out by the scientific community. This report contains a collection of these research highlights. I invite you to read through the report and see for yourself the fascinating work that took place here in the last year. I believe that these highlights speak for themselves.

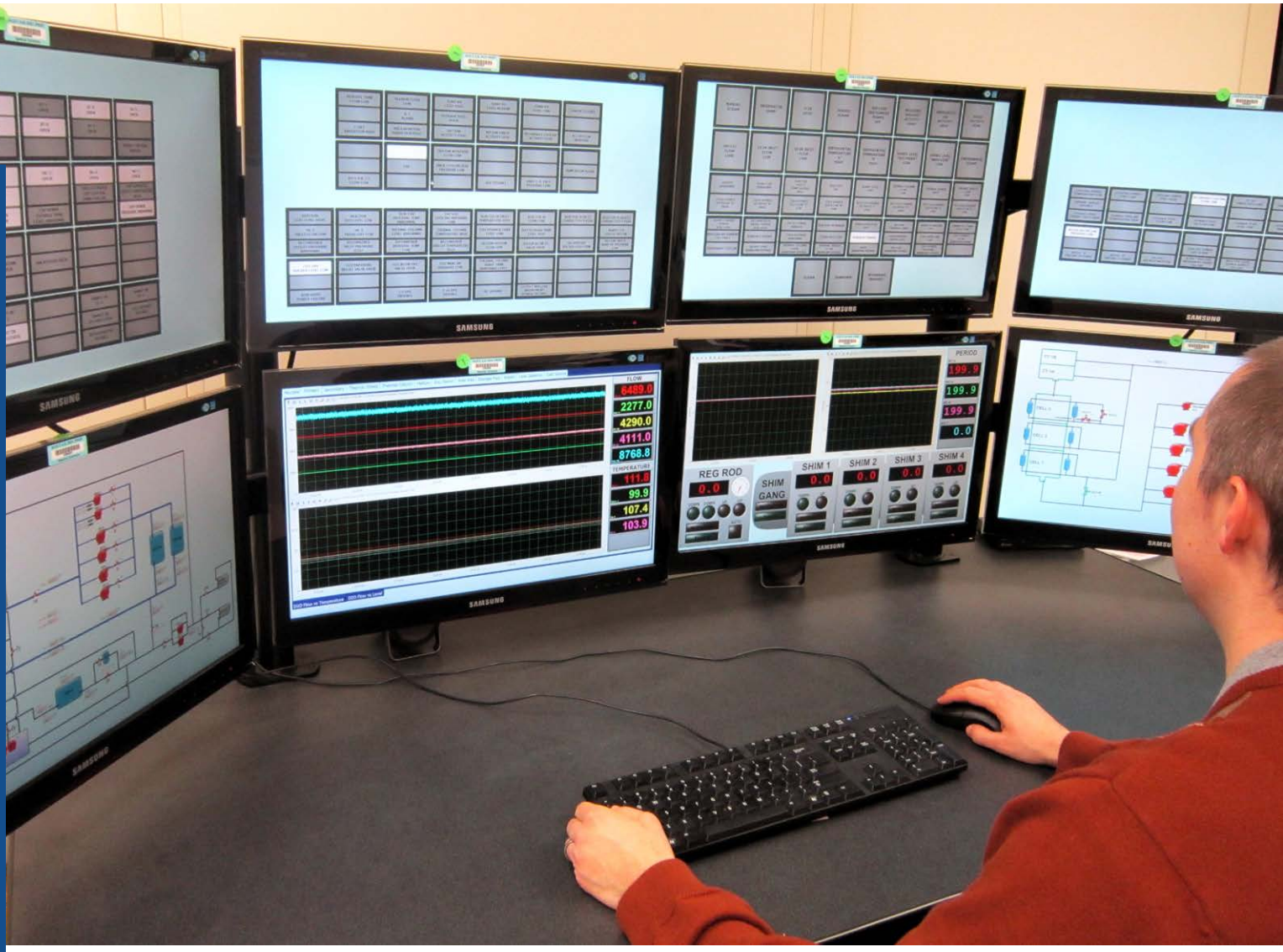

Reactor operator Sam MacDavid is overseeing the wealth of information on the newly upgraded instrumentation console. This upgrade is part of a larger long-term project to modernize the entire reactor control room. Real-time telemetry of all of the major systems of the source operation is now available in a unified display, providing remote process monitoring and trending capability with no reactor control or safety function. As the result of key Summer Undergraduate Research Fellowship (SURF) projects, these trends are also accessible to engineering staff, increasing the ease in viewing and analyzing data. The ability to view trends in process values has been invaluable in identifying issues and allowing their repairs before they become an issue.

The NIST Center for Neutron Research

Neutrons provide a uniquely effective probe of the structure and dynamics of materials ranging from water moving near the surface of proteins to magnetic domains in memory storage materials. The properties of neutrons (outlined below) can be exploited using a variety of measurement techniques to provide information not otherwise available. The positions of atomic nuclei in crystals, especially of those of light atoms, can be determined precisely. Atomic motion can be directly measured and monitored as a function of temperature or pressure. Neutrons are especially sensitive to hydrogen, so that hydrogen motion can be followed in H-storage materials and water flow in fuel cells can be imaged. Residual stresses such as those deep within oil pipelines or in highway trusses can be mapped. Neutron-based measurements contribute to a broad spectrum of activities including engineering, materials development, polymer dynamics, chemical technology, medicine, and physics.

The NCNR's neutron source provides the intense, conditioned beams of neutrons required for these types of measurements. In addition to the thermal neutron beams from the heavy water or graphite moderators, the NCNR has a large area liquid hydrogen moderator, or cold source, that provides long wavelength guided neutron beams for the major cold neutron facility in the U.S.

There are currently 28 experiment stations: 12 provide high neutron flux positions for physics, chemistry, or imaging, and 16 are beam facilities for neutron scattering research. The subsequent pages provide a schematic description of our instruments. More complete descriptions can be found at www.ncnr.nist.gov/instruments/. The second guide hall is currently populated with five instruments, with three new instruments under development.

The Center supports important NIST measurement needs, but is also operated as a major national user facility with merit-based access made available to the entire U.S. technological community. Each year, about 2000 research participants from government, industry, and academia from all areas of the country are served by the facility (see p. 55). Beam time for research to be published in the open literature is without cost to the user, but full operating costs are recovered for proprietary research. Access is gained mainly through a web-based, peer-reviewed proposal system with user time allotted by a beamtime allocation committee twice a year. For details see www.ncnr.nist.gov/beamtime.html. The National Science Foundation and NIST co-fund the Center for High Resolution Neutron Scattering (CHRNS) that operates six of the world's most advanced instruments (see p. 57). Time on CHRNS instruments is made available through the proposal system. Some access to beam time for collaborative measurements with the NIST science staff can also be arranged on other instruments.

WHY NEUTRONS?

Neutrons reveal properties not readily probed by photons or electrons. They are electrically neutral and therefore easily penetrate ordinary matter. They behave like microscopic magnets, propagate as waves, can set particles into motion, losing or gaining energy and momentum in the process, and they can be absorbed with subsequent emission of radiation to uniquely fingerprint chemical elements.

WAVELENGTHS – in practice range from ≈ 0.01 nm (thermal) to ≈ 1.5 nm (cold) (1 nm = 10 Å), allowing the formation of observable interference patterns when scattered from structures as small as atoms to as large as biological cells.

ENERGIES – of millielectronvolts, the same magnitude as atomic motions. Exchanges of energy as small as nanoelectronvolts and as large as tenths of electronvolts can be detected between samples and neutrons, allowing motions in folding proteins, melting glasses and diffusing hydrogen to be measured.

SELECTIVITY – in scattering power varies from nucleus to nucleus somewhat randomly. Specific isotopes can stand out from other isotopes of the same kind of atom. Specific light atoms, difficult to observe with x-rays, are revealed by neutrons. Hydrogen, especially, can be distinguished from chemically equivalent deuterium, allowing a variety of powerful contrast techniques.

MAGNETISM – makes the neutron sensitive to the magnetic moments of both nuclei and electrons, allowing the structure and behavior of ordinary and exotic magnetic materials to be detailed precisely.

NEUTRALITY – of the uncharged neutrons allows them to penetrate deeply without destroying samples, passing through walls that condition a sample's environment, permitting measurements under extreme conditions of temperature and pressure.

CAPTURE – characteristic radiation emanating from specific nuclei capturing incident neutrons can be used to identify and quantify minute amounts of elements in samples as diverse as ancient pottery shards and lake water pollutants.

NIST Center for Neutron Research Instruments

[1] BT-5 Perfect Crystal Ultra-Small Angle Neutron Scattering (USANS) Diffractometer for microstructure up to 10^4 nm.

[2] BT-4 Filter Analyzer Neutron Spectrometer with cooled Be/Graphite filter analyzer for chemical spectroscopy and thermal triple axis spectrometer.

[3] BT-2 Neutron Imaging Facility for imaging hydrogenous matter in large components such as water in fuel cells and lubricants in engines, in partnership with General Motors and DOE.

[4] BT-1 Powder Diffractometer with 32 detectors; incident wavelengths of 0.208 nm, 0.154 nm, and 0.159 nm, with resolution up to $\Delta d/d \cong 8 \times 10^{-4}$.

[5] BT-9 Multi Axis Crystal Spectrometer (MACS II), a cold neutron spectrometer for ultra high sensitivity access to dynamic correlations in condensed matter on length scales from 0.1 nm to 50 nm and energy scales from 2.2 meV to 20 meV.

[6] BT-8 Residual Stress Diffractometer optimized for depth profiling of residual stresses in large components.

[7] BT-7 Thermal Triple Axis Spectrometer with large double focusing monochromator, and interchangeable analyzer/detectors systems.

[8] VT-5 Thermal Neutron Capture Prompt Gamma-ray Activation Analysis Instrument with a neutron fluence rate of 3×10^8 cm^{-2} s^{-1} used for quantitative elemental analysis of bulk materials. Generally used for the analysis of highly hydrogenous materials (≅ 1 % H) such as foods, oils and biological materials.

[9] NG-A Neutron Spin-Echo Spectrometer (NSE) for measuring dynamics from 5 ps to 100 ns.

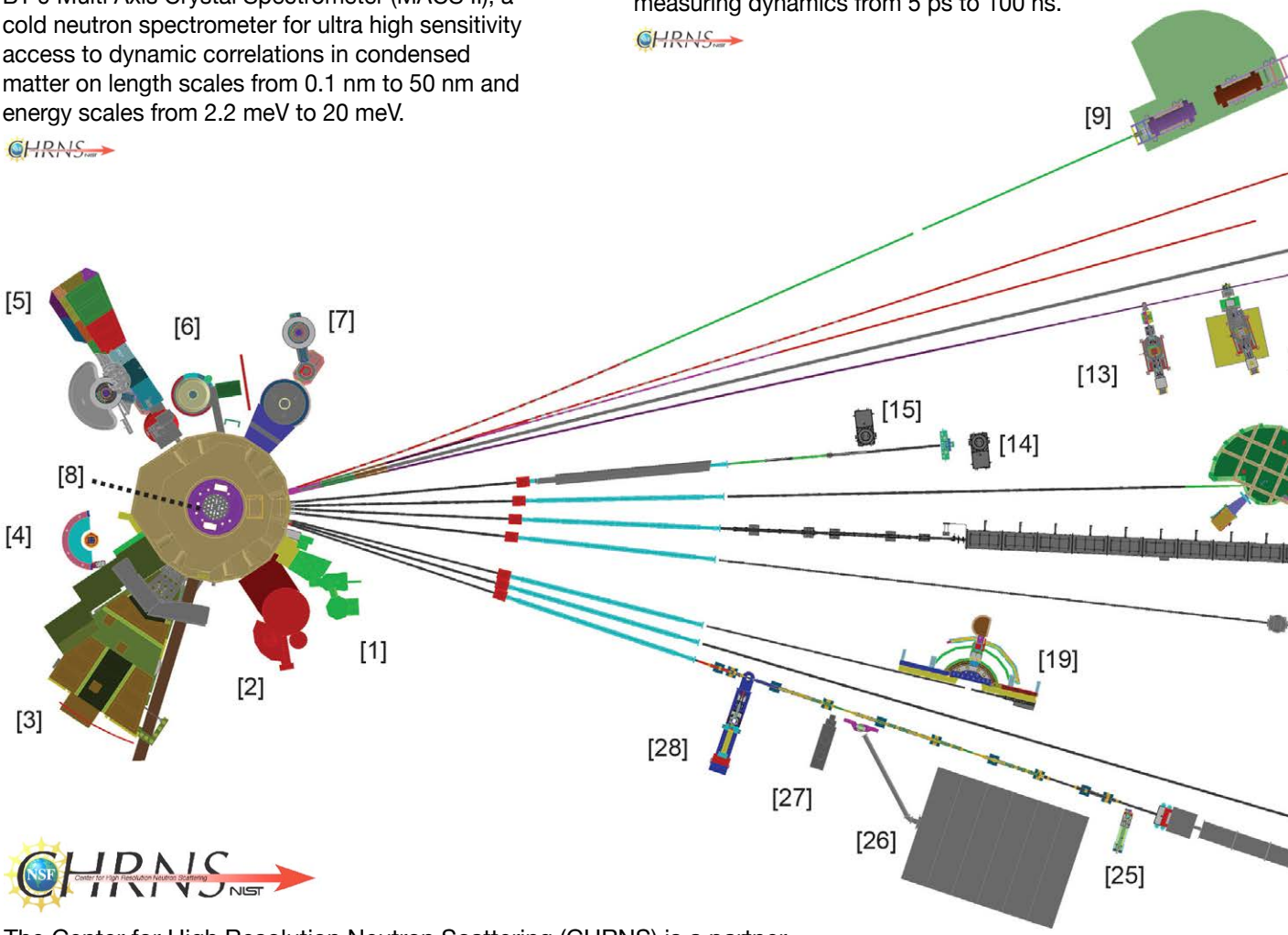

The Center for High Resolution Neutron Scattering (CHRNS) is a partnership between NIST and the National Science Foundation that develops and operates neutron scattering instrumentation for use by the scientific community. The following instruments are part of the Center: 1 (USANS), 5 (MACS II), 9 (NSE), 16 (HFBS), 17 (NG-3 SANS), 18 (DCS).

NIST CENTER FOR NEUTRON RESEARCH INSTRUMENT

(as of Dec. 2013)

[10] NG-BI 10 m SANS for macromolecular structure measurments. *n*Soft

[11] NG-D Cold neutron capture Prompt Gamma Activation Analysis, for quantitative elemental analysis of bulk materials, expecially of hydrogenous ones.

[12] NG-D MAGIk off-spectular reflectometer for studies of thin-film samples with in-plane structure.

[13] NG-D Polarized Beam Reflectometer (PBR) for measuring reflectivities as low as 10^{-8} to determine susurface structure.

[14] NG-1 Cold Neutron Depth Profiling for profiling of subsurface elemental composition.

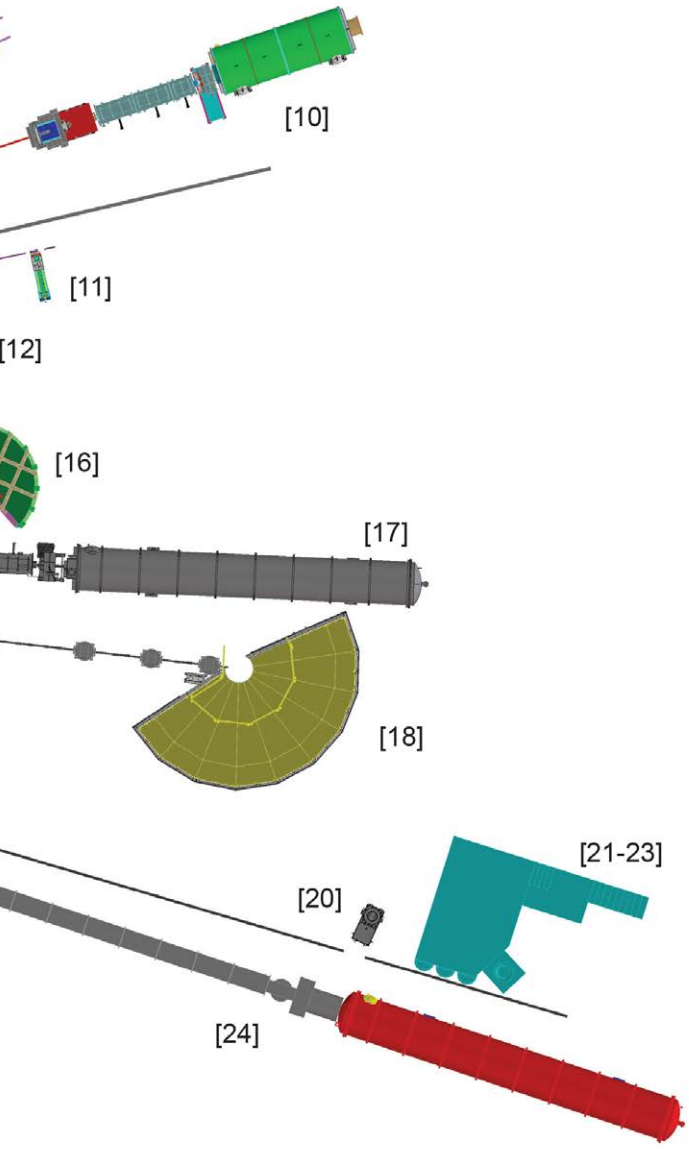

[15] NG-1 Detector development station.

[16] NG-2 Backscattering Spectrometer (HFBS) high intensity inelastic scattering instrument with energy resolution < 1 μeV, for studies of motion in molecular and biological systems.

CHRNS

[17] NG-3 30 m SANS for microstructure measurements. CHRNS

[18] NG-4 Disk Chopper Time-of-Flight Spectrometer for diffusive motions and low energy dynamics. Wavelengths from ≅ 0.18 nm to 2.0 nm and energy resolutions from ≅ 2 μeV to < 10 μeV.

CHRNS

[19] NG-5 Spin-Polarized Triple Axis Spectrometer (SPINS) using cold neutrons with position sensitive detector capability for high-resolution studies.

[20] NG-6A Neutron Physics Test Bed for developing accurate techniques for measurement of the neutron magnetic dipole moment.

[21-23] NG-6 Neutron Physics Station offering three cold neutron beams having wavelengths of 0.5 nm, 0.9 nm, and "white" for neutron physics experiments, including aCORN.

[24] NG-7 30 m SANS for microstructure measurements, in partnership with ExxonMobil and University of Minnesota's IPrime.

[25] NG-7 Cold neutron capture Prompt Gamma Activation Analysis, for quantitative elemental analsis of bulk materials.

[26] NG-7 Neutron Interferometry and Optics Station with perfect crystal silicon interferometer. A vibration isolation system provides exceptional phase stability and fringe visibility.

[27] NG-7 Neutron Physics Interferometry Test Bed for developing novel interferometry techniques.

[28] NG-7 Horizontal Sample Reflectometer allows reflectivity measurements of free surfaces, liquid/vapor interfaces, as well as polymer coatings.

NCNR Images 2013

Paula Lampen (USF) and Kathryn Krycka (NCNR) test out the improvements to polarized SANS at NG7.

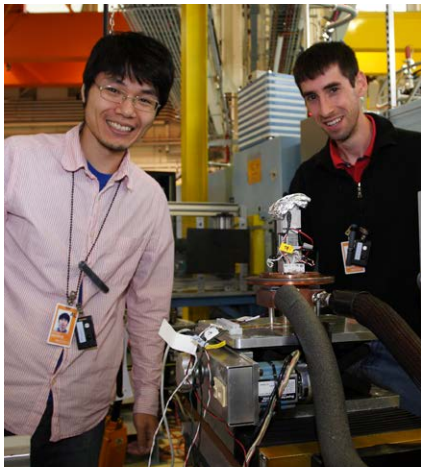

Kiyotaka Akabori and Michael Jablin (CMU) are ready to make some "MAGIk" happen.

Jiajia Wen (JHU) and Kate Ross measure their quantum spin ice at DCS.

Amber Larson (UMd) is ready to collect data at BT1.

Aaron Eberle (ExxonMobil) gathers top-secret SANS data.

Ryan Murphy (Solvay) and Ron Jones (nSOFT) inspect their samples at the 10m-SANS.

NCNR's William Ratcliff and Charles Brooks (Cornell) make some adjustments to their sample environment at BT4.

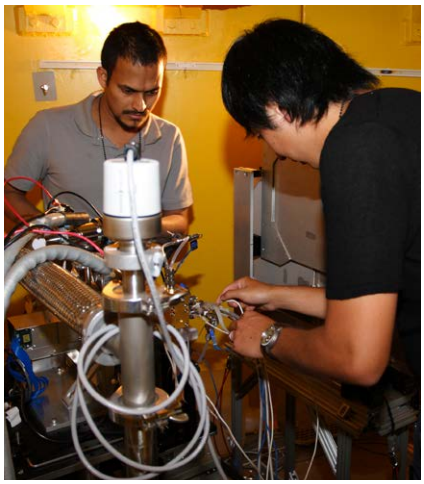

Aman Uddin (U. Conn) and Toshikazu Kotaka (Nissan) align a hydrogen fuel cell for neutron imaging at BT2.

Joshua Cardiel (UW) carefully loads his surfactant samples at USANS.

Jason Gardner (NSRRC), Tsung Yu Ou Yang and Je Wei Lin (Nat. Taiwan U) and Rafael Sa De Freita (Uni. de Sao Paulo) make plans for a DCS experiment.

Summer school students get hands-on experience mounting samples for measurement at DCS while NCNR's Craig Brown supervises.

Summer school students anxiously await the start of their SANS experiment under the watchful eye of NCNR's Matt Wasbrough.

Dan Neumann entertains a tour of undergraduate students from WVU.

Tao Hong (ORNL) prepares for a measurement at MACS II.

David Jacobson (NIST) and Greg Hutchings (UDel) start a tomography scan of a lithium-air battery at the Neutron Imaging Facility.

Dan Phelan (UMN) and NCNR's Daniel Pajerowski change the field on the 10 T magnet during their DCS experiment.

Analytical applications of delayed neutron activation analysis at the NCNR

K. P. Grogan[1], D. J. O'Kelly[1], R. M. Lindstrom[1], and G. P. Lamaze[1]

Delayed neutron activation analysis (DNAA) is a method for measuring fissile elements (e.g., ^{235}U, ^{233}U, and ^{239}Pu) in materials. This technique has been applied to two challenges of national need. The first challenge is nuclear forensics. In today's climate, the threat of illicit and clandestine nuclear activities has become a major concern for Homeland Security and has enhanced the necessity for accurate, sensitive, and rapid analytical and forensic techniques to detect and characterize nuclear materials. The second challenge is the identification and quantification of rare earth elements (REE). REE's are utilized as critical components in a number of industrial applications including automobiles, lasers, solid-oxide fuel cells, and defense technologies [1]. Several REEs, including cerium (Ce), lanthanum (La), and neodymium (Nd), are listed as critical or near-critical with regard to the risk for supply interruption by the U.S. Department of Energy 2011 Critical Materials Strategy Summary [2]. The identification and measurement of these REEs in new domestic sources is an emerging priority.

When uranium (U) is subjected to a neutron flux and fissions, the majority of fission products β^--decay to stable nuclei. A small percentage of fission products, however, remain neutron-rich and are known as delayed neutron precursors. Delayed neutron precursors will β^--decay with half-lives ranging from less than 1 s to about 1 min. This decay occurs with a corresponding delayed neutron emission (as compared to the prompt neutrons emitted during the original fission reaction). This process is illustrated in Fig. 1. A typical DNAA procedure consists of irradiating a sample containing fissile elements for approximately 1 min, followed by rapid transfer of the sample from the irradiation facility to a neutron detection system for a counting time of a few minutes. The delayed neutrons emitted from the sample are compared to those generated from irradiated known standards for quantification of the fissile content in the sample. Advantages of DNAA include the potential for rapid measurements (5 min or less), non-destructive and matrix-independent analyses, and selective and sensitive (sub-nanogram detection limits for ^{235}U) measurements of fissile elements. The DNAA system at the NCNR is one of the world's premier facilities for DNAA measurements. Due to the highly thermalized and stable neutron flux from the RT2 facility at the NBSR reactor, the DNAA system is ideal for making rapid and sensitive measurements of U in materials of interest for nuclear forensics and for REEs.

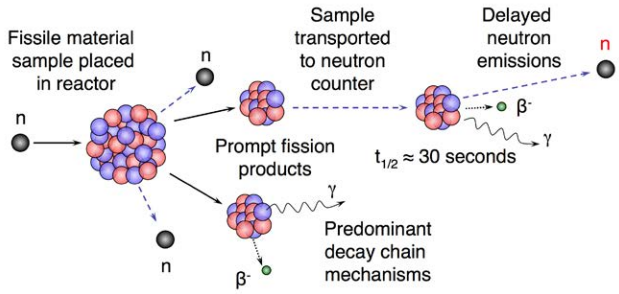

FIGURE 1: Process of delayed neutron production.

The present work describes two applications of DNAA. DNAA is first utilized to determine the natural U content in two NIST Standard Reference Materials (SRM) 1547 Peach Leaves and 1573a Tomato Leaves, which represent potential baseline materials for identifying elevated U concentrations for nuclear forensics. The second application involves the use of instrumental neutron activation analysis (INAA) to quantify REEs in NIST SRM 2586 Trace Elements in Soil Containing Lead from Paint. Several REEs including Ce, La, and Nd are produced as fission products of U during INAA and interfere with the measurement of the natural REE content of the material [3]. These interferences can be corrected by the use of appropriate correction factors based on the amount of U present in a sample [3]. Thus, DNAA is used in tandem with INAA to quantify the U mass fraction in SRM 2586 in order to correct for the REE fission products produced during analysis of Ce, La, and Nd.

The DNAA system was calibrated with eight U standards. The result of the calibration was a highly linear curve with a y-intercept of 1321.8 counts as shown in Fig. 2. Based on the intercept of the calibration and a modification of the Currie equation [4], the minimum number of detectable counts is 1494. This result corresponds to a minimum detectable mass of 17 ng natural U (120 pg ^{235}U) when compared to the calibration curve.

[1]National Institute of Standards and Technology, Chemical Sciences Division, Inorganic Chemical Metrology Group, Gaithersburg, MD 20899

Table 1: INAA Measurements of REEs for SRM 2586.

Element	INAA Value (mg/kg)	U Correction Factor (M_x/M_U)	Corrected INAA Value (mg/kg)	Reference Value (mg/kg)
Ce	64.98 ± 2.52	0.287	64.35 ± 2.50	58 ± 8
La	29.22 ± 1.14	0.0028 x [$e^{0.85893*T}$-1]	28.42 ± 0.98	29.7 ± 4.8
Nd	30.04 ± 3.86	0.21	29.57 ± 3.83	26.4 ± 2.9

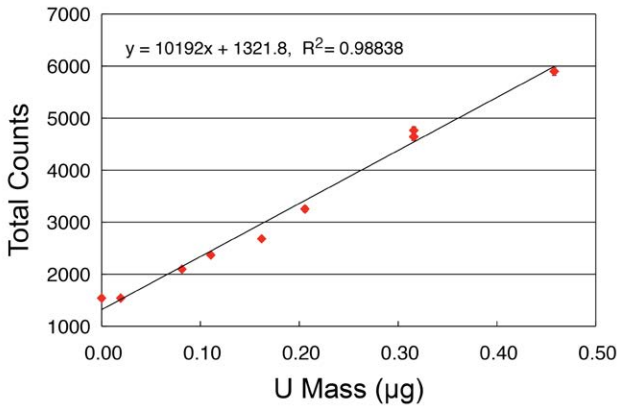

FIGURE 2: Uranium standard calibration curve.

Samples of SRM 1547 and SRM 1573a were analyzed by DNAA for total U content. The DNAA results for these two SRMs are shown in Fig. 3 where the solid lines represent the non-certified mass fractions listed on the certificate for each material, respectively. The average measured U mass fractions were 0.0174 mg/kg ± 0.0006 mg/kg and 0.0412 mg/kg ± 0.0014 mg/kg for SRM 1547 and SRM 1573a, respectively. These values are comparable to the non-certified values (with no associated uncertainty value) of 0.015 mg/kg for SRM 1547 and 0.035 mg/kg for SRM 1573a. These results demonstrate the utility of DNAA for identifying and quantifying trace level U mass fractions in environmental samples that would be desirable in a nuclear forensics application.

Samples of SRM 2586 were analyzed by DNAA and the results are also displayed in Fig. 3. There is no certificate value for U in SRM 2586. The average measured U mass fraction was 2.20 mg/kg ± 0.06 mg/kg. For validation, SRM 1632a, Trace Elements in Coal (Bituminous) was analyzed by DNAA resulting in an average U mass fraction of 1.27 mg/kg ± 0.07 mg/kg, which is in agreement with the certified U mass fraction of 1.28 mg/kg ± 0.02 mg/kg. These results demonstrate the utility of DNAA for measurements of fissile elements and provide a U mass fraction that may be used to correct for U fission products in the analysis of REEs by INAA. The application of this U mass fraction for the correction of Ce, La, and Nd mass fractions as determined by INAA for samples of SRM 2586 is shown in Table 1. The U correction factors were applied by multiplying the measured uranium mass fraction by the correction factor (M_X/M_U). The result of this calculation is the apparent measured mass fraction of the REE of interest generated from U fission during the INAA irradiation. Thus, subtracting this result from the initially measured INAA value for each REE gives the true value of the REE of interest in the sample prior to the generation of fission products. In all cases the measured average mass fractions for the REEs are in good agreement with certificate values for SRM 2586.

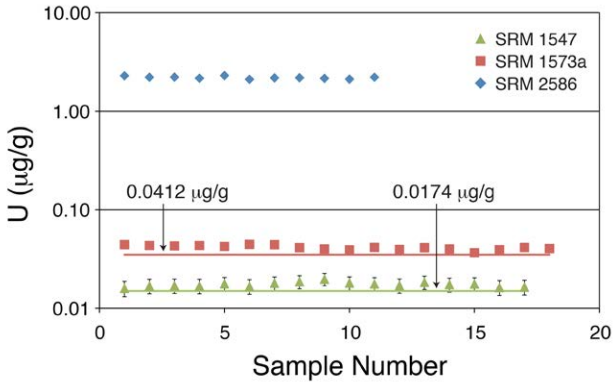

FIGURE 3: Uranium mass fractions in SRM 1547, SRM 1573a, and SRM 2586 as measured by DNAA. Lines are the non-certified mass fraction values of U in the SRM. There is no certificate value for U in SRM 2586.

The DNAA method provided rapid (5 min per sample) analyses with minimal sample preparation and a high degree of accuracy and sensitivity. The presented analyses are useful for validating the use of DNAA as a tool for nuclear forensics and, when coupled with INAA, as a method to more accurately measure rare earth elements. Thus, these methods have the potential to improve the current state of nuclear of forensics and to support the efforts to identify REEs in a variety of domestic materials to address the critical supply risks that have been projected for the near future.

References

[1] X. Du, T. E. Graedel, Environ. Sci. Technol. **45**, 4096-4101 (2011).
[2] U.S. Department of Energy. 2011 Critical Materials Strategy Summary, (2011).
[3] M. D. Glascock, P. I. Nabelek, D. D. Weinrick, R. M. Coveney, Jr., J. Radioanal. Nucl. Chem. **99**, 121 (1986).
[4] L. A. Currie, Anal. Chem. **40**, 586 (1968).

Sealing biomembranes via bio-mimetic polymers: A structural and dynamics study

J.-Y. Wang[1], W. Chen[2], M. Nagao[3,4], J. M. Henderson[1], B. A. G. Hammer[5], L. He[6], B. Akgun[3,7], T. Emrick[5], and K. Y. C. Lee[1]

The cell membrane is essentially an integral lipid bilayer decorated with membrane proteins and carbohydrates. Due to its fragility, traumatic events can disrupt its barrier function. While sealing cell membranes is a naturally occurring repair process, it can be impeded or too slow to cope with the sudden loss of membrane integrity following acute injury. Recently, we developed a new membrane-sealing polymer [1] containing phosphorylcholine (PC) pendant groups that mimic phospholipids, rendering them highly biocompatible [2]. When applied to neurons with ischemia-induced injury, this polymer shows great promise as a membrane sealant, preventing the leakage of intracellular contents and significantly enhancing neuronal survival [3]. To fulfill the potential of this family of polymers as membrane sealing agents, a thorough understanding of the fundamental mechanism responsible for the sealing action is thus the key.

Using neutron reflectivity (NR), small angle neutron scattering (SANS) and neutron spin echo (NSE) techniques, we can explore polymer-induced alterations in membrane structure and dynamics. Fig. 1a shows the NR profile of 1,2-dipalmitoyl (d_{62})-*sn*-glycero-3-phosphocholine-1,1,2,2-d_4-N,N,N-trimethyl-d_9 (d_{75}-DPPC) monolayers on D_2O at surface pressure π = 30 mN/m, and temperature, T = 25 °C. Using a two layer model to analyze the data, the best fit suggests the layer thickness of the head group and tail to be 6.2 Å and 15.9 Å, respectively, with their corresponding scattering length densities (SLD) to be 6.16×10^{-6} Å^{-2} and 7.3×10^{-6} Å^{-2}, and an interfacial roughness, R, of 3 Å (R is the standard deviation of the error function). Adding our biocompatible polymer with pendant PC groups [M_W = 27,000 g/mol, where M_W is the mass average molecular mass, hereafter denoted as HP_27K] to the subphase of a d_{75}-DPPC monolayer under otherwise identical experimental conditions gives rise to the NR profile shown in Fig. 1b. As the SLD of d_{75}-DPPC is fairly close to that of D_2O, this contrast matching strategy increases the sensitivity of the technique in detecting structural changes if the polymer penetrates the lipid film. However, comparison of the NR profiles between d_{75}-DPPC and d_{75}-DPPC+HP_27K shows little difference, indicating that the polymer has little, if any, effect on the structure of the lipid film. It should be noted that at π = 30 mN/m and T = 25 °C, DPPC lipids are in the condensed phase; this high lipid packing density could therefore limit the ability of the PC-polymer to interact with the lipids, thus resulting in little change to the NR profile of d_{75}- DPPC+HP_27K.

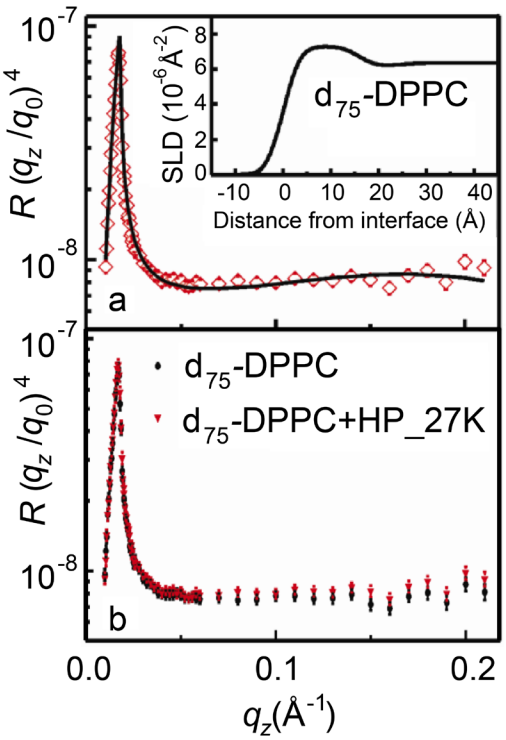

FIGURE 1: (a) NR profile of d_{75}- DPPC on D_2O at π = 30 mN/m and T = 25 °C. Symbols experimental data; (—) best-fit using two layer model. Inset: scattering length density of the best fit to the NR data generated via Motofit. **(b)** NR profiles of d_{75}- DPPC and d_{75}- DPPC+HP_27K on D_2O at surface pressure π = 30 mN/m and T = 25 °C. Measurements were taken at areas $A_{d_{75}\text{-DPPC}}$ = 47.0 Å^2 and $A_{d_{75}\text{-DPPC+HP\_27K}}$ = 46.0 Å^2. The polymer concentration in the subphase is 100 µmol/L.

To further explore possible effects of HP_27K on the structure of lipid membranes, SANS experiments were performed on 1,2-dimyristoyl-sn-glycero-3-phosphocholine (DMPC) large

[1]Department of Chemistry, Institute for Biophysical Dynamics & James Franck Institute, The University of Chicago, Chicago, IL 60637
[2]Argonne National Laboratory, Argonne, IL 60439 and Institute for Molecular Engineering, The University of Chicago, Chicago, IL 60637
[3]NIST Center for Neutron Research, National Institute of Standards and Technology, Gaithersburg, MD 20899
[4]Indiana University, Bloomington, IN 47408
[5]University of Massachusetts, Amherst, MA 01003
[6]Oak Ridge National Laboratory, Oak Ridge, TN 37831
[7]University of Maryland, College Park, MD 20742

unilamellar vesicles (LUVs) at 37 °C, 25 °C, 23 °C, and 15 °C. The main transition temperature, T_m, of DMPC is 23 °C, meaning the lipids are in the fluid phase at 37 °C and 25 °C, and in the gel phase at 23 °C and 15 °C. SANS data of DMPC LUVs at the four temperatures are presented in Fig. 2 (left). The scattering from the bilayer is modeled as vesicles with a Schulz distribution of radii and composed of three layers, each with a corresponding scattering length density. The black lines in the figures are the best fits, yielding lipid membrane dimensions consistent with the NR results. Upon introducing HP_27K (Fig. 2, right) the SANS profiles show little change when compared to the pure LUVs, further confirming that the polymer, regardless of lipid packing density, has little if any qualitative or quantitative influence on the structure of lipid membranes.

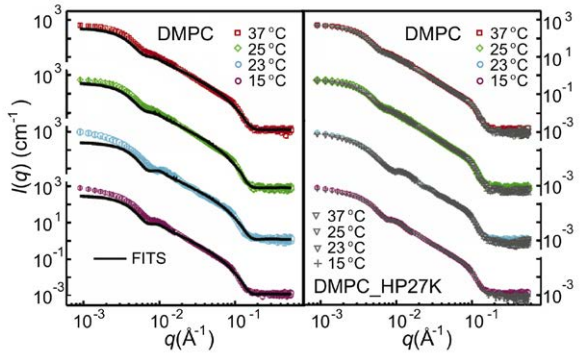

FIGURE 2: SANS of DMPC LUVs at 10 mg/mL (left) and DMPC LUVs in the presence of 200 µmol/L HP_27K (right) at T = 37 °C =, 25 °C, 23 °C, and 15 °C. For profiles of DMPC in the presence of HP_27K, scattering contribution from the polymer was subtracted. The asymmetric three-shell vesicle model was used to fit DMPC profiles (black lines).

Considering that HP_27K behaves as a membrane sealant and yet imparts little influence on the structure of lipid membranes, we hypothesize that the protective effect of the polymer comes from its ability to affect membrane undulations. To test this hypothesis, NSE measurements were employed to examine the dynamics of polymer-induced shape fluctuations of nearly spherical DMPC LUVs; analysis of the data allows us to extract mechanical constants of the lipid bilayer in the absence or presence of the polymer. Fig. 3 shows the normalized intermediate scattering function $I(q,t)/I(q,0)$ originating from the fluctuations of lipid membranes in the absence (Fig. 3a), and in the presence of 200 µmol/L HP_27K (Fig. 3b), as well as from the polymer chains (Fig. 3c) at 37 °C. The $I(q,t)/I(q,0)$ of lipid membranes in the presence of HP_27K has a contribution from both lipid membranes and polymer chains, which can be expressed as:

$$\frac{I(q,t)}{I(q,0)} = (1-f)\left[\frac{I(q,t)}{I(q,0)}\right]_{ZG} + f\left[\frac{I(q,t)}{I(q,0)}\right]_{Zimm}$$

where f is the fraction of the contribution from polymer chain dynamics in solution. The first term originates from the Zilman and Granek model [4] for lipid membranes, which provides the bending modulus, κ, of the lipid bilayer, and the second term from the Zimm model for polymer chain dynamics in dilute solution [5]. As shown in Fig. 3d, κ of DMPC LUVs is found to be (12 to 15) $k_B T$ at temperatures above T_m and (70 to 80) $k_B T$ below T_m. With the presence of HP_27K, κ is increased at all temperatures. These increases in membrane rigidity suggest that HP_27K interacts with lipid membranes through PC-PC head groups, and thereby suppresses membrane fluctuations.

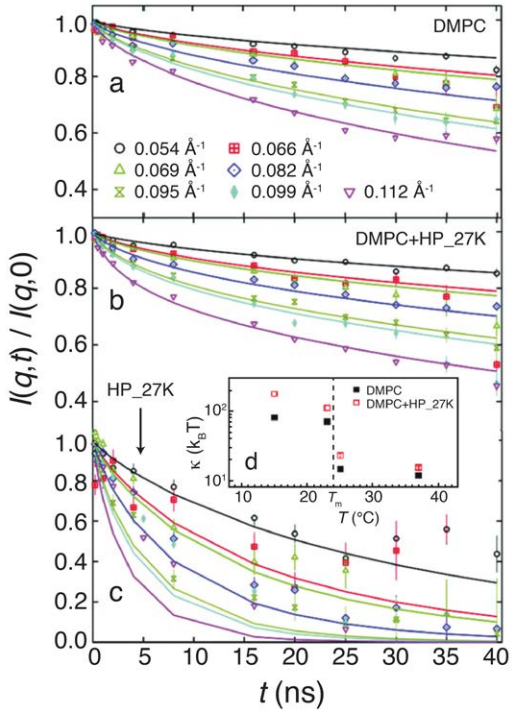

FIGURE 3: Normalized intermediate scattering function for various values of q for (a) DMPC LUVs, (b) LUVs in the presence of HP_27K, and (c) HP_27K with a polymer concentration of 200 µmol/L, all at 37 °C. Fits are to the linear combination of membrane undulation and polymer dynamics for (a) and (b) and polymer dynamics for (c). The bending modulus, κ, as a function of temperature for the lipid membrane of (■) DMPC and (□) DMPC in the presence of HP_27K is shown in the inset (d).

In summary, this neutron scattering study demonstrates that our membrane sealing PC-containing polymer actually has little effect on membrane structures, but greatly slows down membrane undulations, rigidifying the bilayers. The observed influence of the polymer on membrane rigidity only, rather than on the membrane static structure, implies that this PC-polymer influences the membrane through weak, non-intrusive interactions. The information obtained through these studies, in particular NSE, allows us to gain unprecedented insight into the intrinsic molecular aspects of these polymers as membrane sealants.

References

[1] X. Chen, S. McRae, S. Parelkar, T. Emrick, Bioconjugate Chem. **20**, 2331 (2009).
[2] S. Monge, B. Canniccioni, A. Graillot, J. Robin, Biomacromolecules **12**, 1973 (2009).
[3] J.-Y. Wang, W. Chen, K. Y. Lee, *et al.*, manuscript submitted.
[4] A. G. Zilman, R. Granek, Phys. Rev. Lett. **77**, 4788 (1996).
[5] E. D. Violette, P. G. DeGennes, Physics **3**, 181 (1967).

Direct observation of small reversible clusters in concentrated monoclonal antibody solutions

E. J. Yearly[1,2], P. D. Godfrin[1,2], T. Perevozchikova[1,2], H. Zhang[1,3], P. Falus[4], L. Porcar[4], M. Nagao[1,5], J. Curtis[1], P. Gawande[6], R. Taing[7], I. E. Zarraga[7], N. J. Wagner[1], and Y. Liu[1,2]

Therapeutic monoclonal antibodies (mAb) have been found to be highly effective agents in the treatment of immunological and allergic disorders as well as malignant growths with a high level of success due to their structure specificity and low toxicity in contrast to many traditional small molecule drug options. During the last several decades, over 20 mAbs have been approved by the Food and Drug Administration for clinical use and several hundred are currently in development. Because of their success and effectiveness, mAbs are one of the fastest growing therapeutic agents on the market.

The importance of mAb-based drugs motivates fundamental research into problems related to their manufacture and ease of clinical uses. In particular, the pharmaceutical industry is proposing to use subcutaneous injection (SC) delivery methods for some mAbs for convenience and reduced number/frequency of administrations. A high concentration of mAbs (> 100 mg/mL) is often required to attain the effective dosage, which sometimes is associated with an undesired large solution viscosity. Though there is no industrial standard for the upper limit of the viscosity where SC is feasible, it is widely believed that the solution viscosity should be below 50 mPa s. However, the viscosity of many mAb proteins at high concentrations is much higher than this value. The formation of reversible/dissociable clusters at relatively high protein concentrations has been hypothesized to cause the high viscosities observed for some mAb solutions. One important characteristic of reversible clusters is that the clusters form at high concentration and reversibly dissociate into monomers at sufficiently low concentrations. However, to date, it has been difficult to directly observe these mAb dynamic clusters and quantitatively characterize their microstructure in crowded environments. Here, we combine the methods of small-angle neutron/x-ray scattering (SANS/SAXS), neutron spin echo (NSE), and computer simulations to conclusively identify the formation of dynamic clusters and their morphology in highly concentrated and viscous mAb solutions [1,2]. In particular, NSE allows the estimation of the hydrodynamic radius and characterization of the dynamic properties in concentrated solutions.

Two mAbs with markedly different solution viscosities, denoted as mAb1 and mAb2, are used as model systems. Both mAbs have been widely investigated. They are constructed with the same human IgG1 framework, and thus, have nearly the same molecular mass (≈ 150 kDa) and primary sequence, with differences only in the complementarity determining region. Lyophilized forms of these mAbs are reconstituted into D_2O-based buffers to reduce the incoherent background during neutron scattering experiments. Both mAbs have a positive net charge, +17 for mAb1 and +27 for mAb2. The reconstituted protein solutions have the ionic strength of the solvent of ≈ 17 mmol/L. Fig. 1 shows the solution viscosity, η, for these mAbs as a function of concentration, C, at 25 ˚C. Note that η of mAb1 has an anomalously large viscosity of 310 mPa s at 150 mg/mL compared to many other mAbs that have much lower viscosity. For example, η for mAb2 is only 18 mPa s at 150 mg/mL. Even though the η of mAb1 does not seem unusually high compared with many other materials such as polymer blends or colloidal glass/gel systems, this viscosity limits the allowable concentration for bulk manufacturing as well as delivery through thin needles.

The low concentration mAb solutions are first analyzed by SAXS and DLS. The combined analyses of the apparent radius of gyration and the apparent hydrodynamic radius demonstrate that at 1 mg/mL, both mAb1 and mAb2 exist as only monomers. However, when the concentration increases to about 10 mg/mL, the mAb1 solution is dominated by clusters while mAb2 exists still as monomers. The average molecular mass of mAb1 clusters at 10 mg/mL is estimated to be about that of a dimer. It should be noted that this cluster formation in mAb1 solutions is fully reversible upon dilution. Therefore, the microstructure of mAb1 in solution progresses from dispersed monomers to an increasing proportion of

[1]NIST Center for Neutron Research, National Institute of Standards and Technology, Gaithersburg, MD 20899
[2]University of Delaware, Newark, DE 19716
[3]University of Maryland, College Park, MD 20740
[4]Institut Laue-Langevin, Grenoble, France
[5]Indiana University, Bloomington, IN 47405
[6]Theranos Inc., Palo Alto, CA 94304
[7]Late Stage Pharmaceutical Development, Genentech Inc, South San Francisco, CA 94080

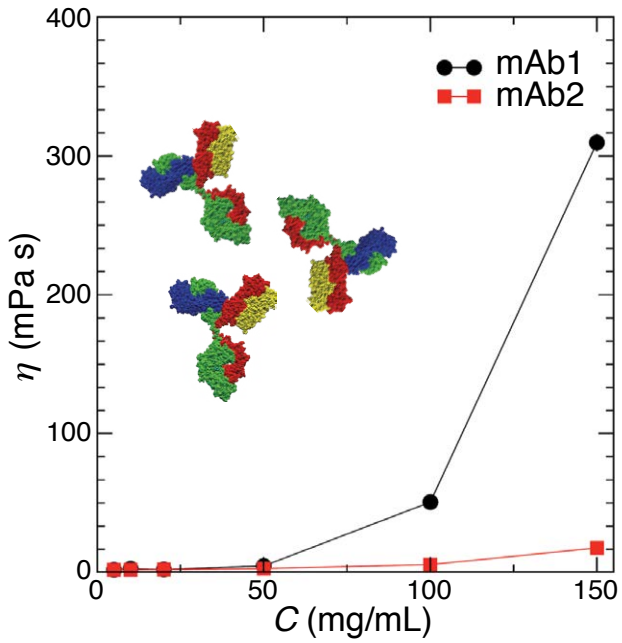

FIGURE 1: The viscosity of mAb1 and mAb2 as a function of concentration. The inset represents a cluster of mAb1 that is responsible for the increased viscosity.

reversible clusters as concentration increases from 1 mg/mL to 10 mg/mL. However, at higher concentrations (> 10 mg/mL), it is very difficult to accurately determine the evolution of clusters using DLS or SANS/SAXS due to the effect of the inter-particle structure factor and collective diffusion.

To extract a more quantitatively accurate cluster size in the highly concentrated protein solutions, we use NSE and measure the short-time self-diffusion coefficient, D_s, of proteins in solution, which is related to the hydrodynamic radius of the clusters. NSE measures the normalized intermediate scattering function, $S(Q,t)/S(Q)$, which can be expressed as $e^{-D_c(Q)Q^2t}$ in the short-time limit, where $D_c(Q)$ is the short-time collective diffusion coefficient with the asymptotic value in the high Q limit being the short-time self-diffusion coefficient, D_s, through which the apparent hydrodynamic radius can be estimated [3]. Because $R_h \sim 1/D_s$, the ratio of $1/D_s$ between mAb1 and mAb2 is an estimate of the average size of the dynamic clusters in mAb1 solutions relative to mAb2. It has been shown that mAb2 remains dispersed as monomers through the studied concentration range [1]. Thus this ratio is an indicator of the relative size of reversible clusters in mAb1 solutions. Fig. 2 shows the ratio of $1/D_s$ between mAb1 and mAb2 as a function of C. Note that when $C \leq 10$ mg/mL (star symbols in Fig. 2), D_s is approximated with the results obtained by DLS while at higher concentrations, D_s is obtained by NSE. At 1 mg/mL, the ratio is one, as both mAb1 and mAb2 exist as monomers in solutions. At 10 mg/mL, the ratio reaches about 1.7. It is intriguing to observe that this ratio does not change substantially with further increases in concentration up to 150 mg/mL. This suggests that mAb1 protein clusters form at relatively low concentrations, and their size remains relatively constant up to high concentrations. This behavior is akin to that of self-assembled micellization in surfactant solutions, where above a critical micelle concentration, additional surfactant added to the system goes into micelle formation. The NSE diffusivity results here suggest the critical monomer concentration for mAb1 is around 10 mg/mL. Therefore, at high concentrations, such as 150 mg/mL, the dominating fraction of mAb1 species is the small reversible clusters. Therefore, the formation of small clusters is the driving force for the large viscosity in our samples.

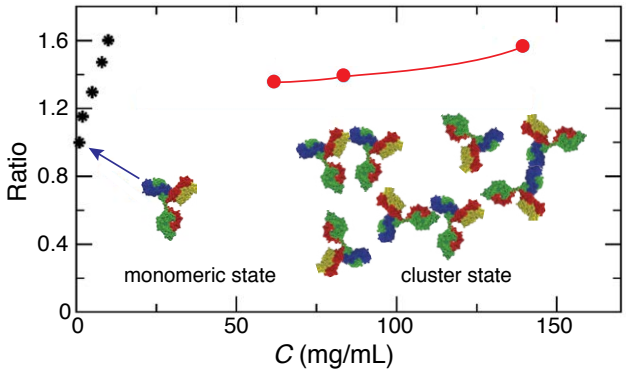

FIGURE 2: The ratio of the self-diffusion coefficient between mAb2 and mAb1 as determined from DLS (black) and NSE (red). The ratio is the relative cluster size of mAb1 compared to mAb2.

In conclusion, using NSE to measure diffusivity and SANS to probe the microstructure of two model mAb proteins in solution over a broad concentration range, we demonstrate that the formation of a large fraction of reversible clusters in solution substantially increases the viscosity of mAb solutions. The average cluster size remains almost identical over a wide range of concentrations. The insights obtained here on mAb clustering behavior and its impact on bulk properties such as viscosity are useful in the development of mAbs and their formulations with desired solution properties. These in turn aid in their efficient production and their effective delivery in the clinic.

References

[1] E. J. Yearley, I. E. Zarraga, S. J. Shire, T. M. Scherer, Y. Gokarn, N. J. Wagner, Y. Liu, Biophys. J. **105** (30) 720 (2013).
[2] E. J. Yearley, P. D. Godfrin, T. Perevozchikova, H. Zhang, P. Falus, L. Porcar, M. Nagao, J. Curtis, P. Gawande, R. Taing, I. E. Zarraga, N. J. Wagner, Y. Liu, submitted, (2013).
[3] Y. Liu, L. Porcar, J. Chen, W.-R. Chen, P. Falus, A. Faraone, E. Fratini, K. Hong, P. Baglioni, J. Phys. Chem. B **115**, 7238 (2011).

How does the GRASP protein tether the membrane stacks in the Golgi apparatus?

G. H. Zan[1], C. Bachert[2], F. Heinrich[1,4], M. Lösche[1,3,4], and A. D. Linstedt[2]

BIOLOGY

In the Golgi apparatus of a mammalian cell, freshly synthesized proteins are modified, sorted, and packaged for shipping to destinations within or outside the cell. The large Golgi apparatus can be easily recognized under a light microscope by its elongated, ribbon-like membrane network. Golgi membranes form stacks of sub-compartments, called cisternae, in which the various functions of the Golgi are performed. A membrane protein family, suitably named GRASP, tethers these stacks of membranes giving the Golgi structural integrity. With neutron scattering methods available at the NIST Center for Neutron Research our collaboration investigated the structural basis for membrane tethering by the GRASP protein.

Golgi cisternae are either linked by self-associating GRASP55 or GRASP65 proteins [1,2]. At each tether point two GRASP molecules that are located on adjacent membrane surfaces form one structural unit, or homo-dimer. Each GRASP protein contains two PDZ-like domains and an internal PDZ ligand that protrudes from the surface of the molecule. PDZ domains are globular protein-protein interaction modules found in a large number of proteins. Self-association of GRASP occurs via the intermolecular insertion of the ligand into the binding groove of the first PDZ domain. The GRASP proteins are anchored to their respective Golgi cisternae by a combination of an N-terminal myristic acid and interaction with a Golgi-localized binding partner. In the case of GRASP65, this binding partner is GM130, which contains a C-terminal PDZ ligand that binds the second PDZ domain. Such dual anchoring of the GRASP appears to be required not only for its stable membrane association but also for its membrane tethering activity. Stable, singly anchored versions of GRASP proteins have been created using transmembrane domains but these fail to tether, whereas similar dually anchored constructs retain full activity. Immuno-precipitation of these constructs suggests that the function of dual anchoring is to prevent cis interactions within the same membrane that might interfere with the tethering function. These observations, together with the relative positions of the internal ligand and the PDZ binding groove on the surface of the molecule, suggest that orientation on the membrane may be the mechanism that favors GRASP interactions in trans relative to those in cis. Orientation-dependent control could have broad implications towards understanding the many important membrane cross-bridging interactions.

For our studies we prepared GRASP55 in either its myristoylated or non-myristoylated form. Both forms contain a C-terminal hexa-histidine tag that binds to N-nitrilotriacetic acid (NTA)-functionalized lipids in the bilayer, mimicking the Golgi-localized binding partner of GRASP55. With a functional assay we showed that the dually anchored form retains tethering activity, while the singly anchored form does not. With neutron reflectometry, we directly determined the orientations of the singly and dually anchored proteins at the membrane. As lipid membrane mimics, sparsely tethered bilayer lipid membranes [3] were used. Here, the tether molecules that anchor the membrane to the solid support create a nanometer-thick hydrated layer between the solid surface and the lipid bilayer that keeps the bilayer in the physiologically relevant in-plane fluid state, while allowing neutron scattering analysis of the associated proteins [4,5]. Fig. 1 shows the measured reflectivity for the myristoylated GRASP55.

The structural envelope of the membrane-associated GRASP domain was modeled using a free-form spline, and by means of rigid body rotations of the GRASP crystal structure [7] (see Fig. 2, for the myristoylated GRASP 55). Both modeling approaches are in agreement with each other, and show a clear dependence of the protein orientation on myristoylation. Whereas the envelope of the non-myristoylated GRASP is compatible with several orientations, all of them present both PDZ domains to the membrane. On the other hand, the data

[1]Department of Physics, Carnegie Mellon University, Pittsburgh, PA 15213
[2]Department of Biological Sciences, Carnegie Mellon University, Pittsburgh, PA 15213
[3]Department of Biomedical Engineering, Carnegie Mellon University, Pittsburgh, PA 15213
[4]NIST Center for Neutron Research, National Institute of Standards and Technology, Gaithersburg, MD 20899

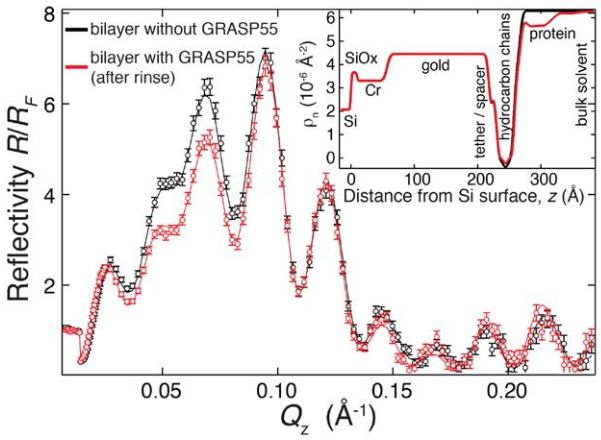

FIGURE 1: Neutron reflectometry curves with best fit, and scattering length density profile of the entire sample with and without GRASP protein bound to the lipid membrane. Only reflectivity measurements taken with D_2O-based bulk solvent are shown. The scattering length density profile was determined using a co-refinement of all measured reflectivity curves in D_2O and H_2O-based buffer and a composition-space model [6]. Error bars on the data represent one standard deviation.

for the myristoylated version could be fit only with a single orientation (see Fig. 3). There, the protein assumes an upright orientation in which only one PDZ domain interfaces with the membrane and presents the myristoyl group to the membrane interface.

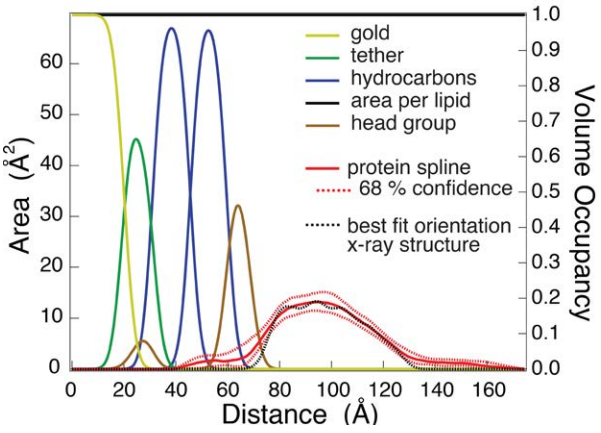

FIGURE 2: Composition-space model [6] for the lipid bilayer and the envelope of the bound myristoylated GRASP protein. The protein envelope was determined using a free-form spline model. Uncertainties were calculated using a Monte Carlo Markov Chain method [8]. For comparison, the protein envelope shown is from the best-fit orientation of the x-ray solution structure of GRASP after reintroducing residues that were not crystallized.

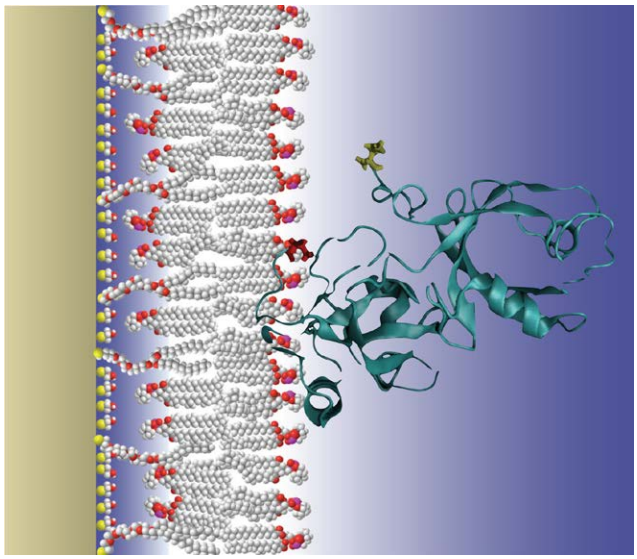

FIGURE 3: The penetration depth and orientation of a single myristoylated GRASP protein bound to a lipid membrane as determined by neutron reflectometry.

The presented work provides direct evidence that protein orientation on the membrane depends critically on protein myristoylation, thus giving a structural explanation to the experimental observation that dual anchoring is required for membrane tethering of GRASP [9]. Based on the protein orientation found from neutron reflectometry, molecular modeling will be used to construct a model of the trans tethering complex to help understand and visualize the tethering process.

References

[1] J. Shorter, R. Watson, M. E. Giannakou, M. Clarke, G. Warren, F. A. Barr, EMBO J. **18**, 4949 (1999).

[2] F. A. Barr, M. Puype, J. Vandekerckhove, G. Warren, Cell **91**, 253 (1997).

[3] D. J. McGillivray, G. Valincius, D. J. Vanderah, W. Febo-Ayala, J. T. Woodward, F. Heinrich, J. J. Kasianowicz, M. Lösche, Biointerphases **2**, 21 (2007).

[4] H. Nanda, S. A. K. Datta, F. Heinrich, M. Lösche, A. Rein, S. Krueger, J. E. Curtis, Biophys. J. **99**, 2516 (2010).

[5] S. Shenoy, P. Shekhar, F. Heinrich, M. C. Daou, A. Gericke, A. H. Ross, M. Lösche, PLoS ONE **7**, e32591 (2012).

[6] P. Shekhar, H. Nanda, M. Lösche, F. Heinrich, J. Appl. Phys. **110**, 102216 (2011).

[7] S. T. Truschel, D. Sengupta, A. Foote, A. Heroux, M. R. Macbeth, A. D. Linstedt, J. Biol. Chem. **286**, 20125 (2011).

[8] B. J. Kirby, P. A. Kienzle, B. B. Maranville, N. F. Berk, J. Krycka, F. Heinrich, C. F. Majkrzak, Curr. Opinion Coll. Interface Sci. **17**, 44 (2012).

[9] H. -Z. Goh, C. Bachert, F. Heinrich, H. Nanda, M. Lösche, A. D. Linstedt, J. Biol. Chem. (in preparation).

More efficient petroleum refining using a highly hexane-selective Metal-Organic Framework

M. R. Hudson[1], C. M. Brown[1,2], Z. R. Herm[3], B. M. Weirs[3], J. A. Mason[3], J. M. van Baten[4], P. Zajdel[5], N. Masciocchi[6], R. Krishna[4], and J. R. Long[3]

Metal-organic frameworks (MOFs) constitute a large family of microporous solids exhibiting high surface areas, tunable pore dimensions, and adjustable surface functionality. The possibility of creating pore characteristics in MOFs that cannot readily be achieved in zeolites or carbons expands the opportunities for molecular recognition [1]. The efficient separation of alkane isomers by adsorption is especially challenging because the molecules are chemically inert and have similar polarizabilities, leaving shape as the method of differentiation. This separation is critical to the production of gasoline, which includes ≈ 10 % pentanes and hexanes. We have recently [2] reported a MOF whose structure and n-hexane adsorption properties were characterized with neutron diffraction, and features sharply angled pore walls capable of fractionating alkane isomers according to the degree of branching.

Hexanes of formula C_6H_{14} are generated at enormous scale through a catalytic isomerization reaction that results in a thermodynamically controlled product stream composed of (10 to 30) % mole fraction of each of the 5 possible isomers. The value of a particular isomer as a component in the gasoline pool is related to its research octane number (RON) and is highest for the dibranched hexanes 2,3-dimethylbutane (2,3-DMB) and 2,2-dimethylbutane (2,2-DMB), which have values of 105 and 94, respectively. The RONs for the monobranched isomers 2-methylpentane (2-MP) and 3-methylpentane (3-MP) are substantially lower, at 74 and 75, respectively, while the value for linear n-hexane is only 30. To achieve higher octane number blends, current processes sieve n-hexane by using zeolites, generating a mixture of the other four isomers with a final RON of nearly 83 while returning n-hexane to the isomerization reactor. Some separation processes achieve higher-grade mixtures by subsequently distilling the monobranched isomers away from the valuable DMB products. An improved hexane-separation process would selectively isolate the most valuable products, 2,3-DMB and 2,2-DMB, while returning the less valuable monobranched isomers to the isomerization reactor along with n-hexane (Fig. 1). It would potentially benefit public health, because it could reduce the usage of toxic aromatics, which are currently added to boost the octane number of gasoline.

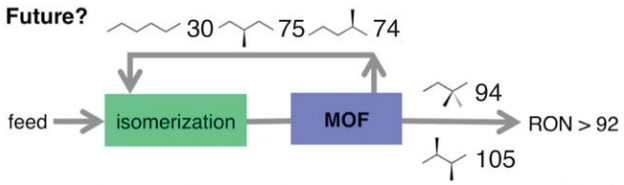

FIGURE 1: Proposed hexane isomer separation processes including the research octane numbers and final product RON. $Fe_2(BDP)_3$ may make it viable to isolate only the two most valuable isomers.

In comparing the structures of zeolites to those possible in MOFs, a prominent distinction lies in the angles that can be obtained for the internal pore walls. Whereas the pore contours defined by a zeolite scaffolding are necessarily obtuse, the higher coordination numbers possible for the metal nodes within a MOF can give rise to flat pore surfaces that intersect at acute angles. This is apparent in the structure of the new MOF $Fe_2(BDP)_3$ (Fig. 2). The rigid, nearly planar 1,4-benzenedipyrazole anionic ligands define a channel structure featuring sharply angled crevices running along the triangle corners with chains of octahedral iron(III) centers forming the vertices of the triangles. The strong iron(III)-pyrazolate bonds and highly connected architecture of $Fe_2(BDP)_3$ lend it exceptional chemical and thermal stability. The material can be boiled in aqueous solutions at pH = 2 to pH = 10 for 2 weeks or heated in air to at least 280 °C without losing crystallinity. Pure-component equilibrium adsorption isotherms for the 5 different hexane isomers were measured for $Fe_2(BDP)_3$ at 3 temperatures within the range relevant to the industrial separation. In contrast to zeolite 5A, a sieve for n-hexane, the dimensions of the channels in the evacuated structure of $Fe_2(BDP)_3$ are large enough to accommodate all 5 hexane isomers. At 100 mbar and 200 °C, $Fe_2(BDP)_3$ adsorbs 60 % more n-hexane by volume and 100 % more by mass than zeolite 5A. This enhancement renders $Fe_2(BDP)_3$ a more efficient adsorbent than zeolite 5A for the n-hexane separation presently carried out in industry. Complementary to the ordered adsorption of dibranched isomers, neutron diffraction data demonstrate the lack of a preferred arrangement of n-hexane molecules within the

[1]NIST Center for Neutron Research, National Institute of Standards and Technology, Gaithersburg, MD 20899
[2]University of Delaware, Newark, DE 19716
[3]University of California, Berkeley, CA 94720
[4]Van't Hoff Institute for Molecular Sciences, University of Amsterdam, Science Park 904, 1098 XH Amsterdam, Netherlands
[5]Institute of Physics, University of Silesia, ul. Uniwersytecka 4, 40-007 Katowice, Poland
[6]Dipartimento di Scienza e Alta Tecnologia, Università dell'Insubria, via Valleggio 11, I-22100 Como, Italy

pores of $Fe_2(BDP)_3$ when dosed with perdeuterated n-hexane. Attempts to refine the position of the n-hexane molecules in both samples were thoroughly exhausted by using several different refinement approaches, suggesting that there is unlikely any correlation between the positions of guests adsorbed in each pore.

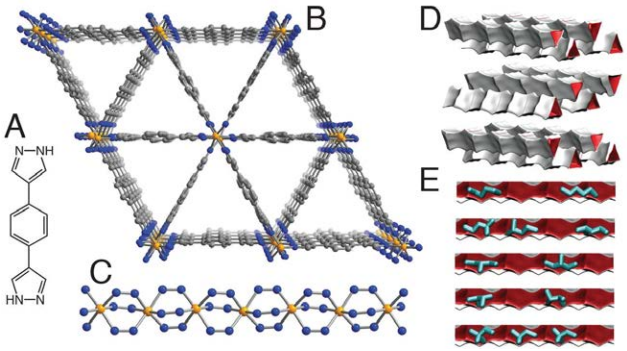

FIGURE 2: (A) H_2BDP ligand; **(B)** the [001] direction in $Fe_2(BDP)_3$ structure, (Fe- orange, N- blue, and C- gray with H omitted); **(C)** chains of pyrazolate-bridged FeII octahedra; **(D/E)** van der Waals surfaces with snapshots of hexane isomers from simulations.

In addition to entropic differences, the enthalpies of adsorption among the 5 hexane isomers in $Fe_2(BDP)_3$ are dependent on the degree of branching as well. Isosteric heats of adsorption were calculated by differentiation of the temperature-independent fits to the isotherm data (Fig. 3). The linear n-hexane isomer has the strongest interaction with the framework, because a greater fraction of its surface can interact with the triangular channel pore surface than the other isomers, while the more compact DMB isomers are not flexible enough to maximize van der Waals interactions with the pore surfaces and have the lowest enthalpies at all loadings. The isomers are all interacting with the same, relatively homogeneous surface differently. This trend has also been observed in other MOFs for a selected subset of hexane isomers but never for all 5 isomers. The trends in the enthalpy and entropy of adsorption for the 5 hexane isomers conspire to generate a free energy hierarchy of linear < monobranched < dibranched isomer adsorption. Although separate enthalpy and entropy trends of this type have been established previously, the combined contributions of both within $Fe_2(BDP)_3$ offers exceptional potential for separating the valuable dibranched hexanes from the other isomers. The hexane isomer separation ability of $Fe_2(BDP)_3$ was evaluated with a breakthrough experiment in which an equimolar mixture of all 5 isomers in N_2 was passed over a bed of the material heated at 160 °C (Fig. 3). Pure 2,2-DMB eluted first, followed by 2,3-DMB, those with high RON values, then 2-MP eluted subsequently, immediately followed by 3-MP and finally, much later, n-hexane. During the beginning of the experiment, the RON of the eluted mixture rises to greater than 90, significantly higher than the value of 83 that is typical for industrially refined hexane blends. The shape of the breakthrough curve for each isomer is informative with regard to the separation. The steepness of the DMB breakthrough events suggests that the separations for these isomers result from essentially equilibrium processes and are not diffusion controlled. The two MPs and n-hexane display more gradual breakthrough events, suggesting that diffusion is a contributory factor in the elution dynamics.

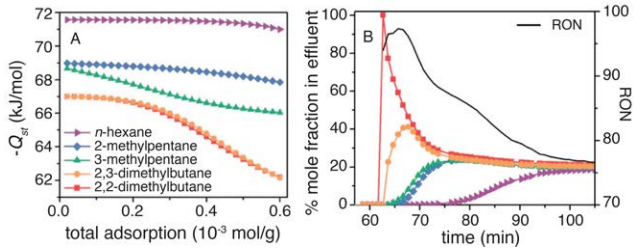

FIGURE 3: (A) Isosteric heats of adsorption vs. hexane loading; **(B)** Experimental breakthrough data with calculated RON for 5 hexanes eluting through $Fe_2(BDP)_3$ at 160°C.

Pulse chromatography simulations were performed to further probe the separation properties and indicate that the material can separate a mixture of hexane isomers into three fractions: 2 DMB isomers, 2 MP isomers, and n-hexane. These 3 fractions could potentially serve independent purposes: the DMB added to gasoline, the n-hexane reintroduced to the isomerization reactor, and the MP isomers returned to the isomerization reactor downstream, allowing for better conversion. Such a staged recycling scheme could significantly boost the efficiency of the isomerization process. A relevant comparison is obtained by comparing the number of moles of 92 RON product that can be obtained per liter of adsorbent in a packed bed adsorber from published data and Configurational-bias Monte Carlo (CBMC) simulations. These comparisons show that for $Fe_2(BDP)_3$ the 92 RON productivity is 0.54 mol/L, whereas the values obtained for other adsorbents are consistently lower. Our CBMC calculations suggest that the size of the channels in $Fe_2(BDP)_3$ is nearly optimal for hexane separation. Narrower triangular channels cannot accommodate all 5 isomers, whereas wider channels do not maximize the differences in van der Waals contacts.

We have determined that the adsorption selectivity and structural stability of $Fe_2(BDP)_3$ may make it viable to isolate only the two most valuable isomers from the other three leading the way to cheaper, more energy efficient gasoline production in the future.

References

[1] E. D. Bloch, W. L. Queen, R. Krishna, J. M. Zadrozny, C. M. Brown, J. R. Long, Science **335**, 1606 (2012).

[2] Z. R. Herm, B. M. Weirs, J. A. Mason, J. M. van Baten, M. R. Hudson, P. Zajdel, C. M. Brown, N. Masciocchi, R. Krishna, and J. R. Long, Science **340**, 960 (2013).

The role of random electric fields in relaxors

D. Phelan[1], C. Stock[2], J. A. Rodriguez-Rivera[1,3], J. Leao[1], S. Chi[1,3], X. Long[4], Y. Xie[4], A. A. Bokov[4], Z.-G. Ye[4], P. Ganesh[5], and P. M. Gehring[1]

The remarkable electromechanical properties of lead-oxide, perovskite $PbBO_3$ relaxors such as $Pb(Mg_{1/3}Nb_{2/3})_{1-x}Ti_xO_3$ (PMN-*x*PT) and $Pb(Zn_{1/3}Nb_{2/3})_{1-x}Ti_xO_3$ (PZN-*x*PT) have inspired numerous attempts to understand the piezoelectricity in terms of the structural phase diagram. The diagram contains a steep morphotropic phase boundary (MPB) separating pseudo-rhombohedral and tetragonal states over a narrow compositional range where the piezoelectricity is maximal. These materials exhibit very low hysteresis, extremely large dielectric constants, and record-setting piezoelectric coefficients at room temperature that form an unusually appealing set of properties. These have the potential to revolutionize a myriad of important technological applications spanning medical diagnostic sonography, military sonar, energy harvesting, and high-precision actuators. Many researchers have argued that quenched random electric fields (REFs) play a central role in establishing the relaxor phase, in part because the *B*-sites of all known lead-oxide perovskite relaxors are occupied by random mixtures of heterovalent cations. However recent theoretical work suggests relaxor behavior can occur in the absence of REFs [1,2]. In fact, it has not been proven that REFs are essential to the relaxor state or if they play any role in the ultrahigh piezoelectricity. These basic questions persist in the face of decades of research because no rigorous definition of a relaxor exits, *i.e.*, there is no precise mathematical formulation of the relaxor order parameter. To date any material for which the real component of the dielectric permittivity $\varepsilon'(\omega,T)$ exhibits a broad peak at a temperature T_{max} that depends strongly (and in some cases only weakly) on the measuring frequency is classified as a relaxor. This definition has been applied equally to PMN and PZN, which possess strong REFs, as well as to specific compositions of $K(Ta_{1-x}Nb_x)O_3$ (KTN), $(K_{1-x}Li_x)TiO_3$ (KLT), $Ba(Zr_{1-x}Ti_x)O_3$ (BZT), and $Ba(Sn_{1-x}Ti_x)O_3$ (BST), all of which possess comparatively weak REFs.

To identify REF-specific properties uniquely one must compare identical systems that differ only in the strength of the REFs. While such an idealized situation does not exist, the recent breakthrough in the growth of millimeter-size, high-quality, single crystals of $Pb(Zr_{1-x}Ti_x)O_3$ (PZT) has finally provided experimentalists with a nearly perfect model system with which such a comparison can be made to classic relaxor systems such as PMN-*x*PT. Both PZT and PMN-*x*PT are disordered, lead-oxide perovskites, and both exhibit phase diagrams as a function of Ti composition that contain an MPB near which exceedingly large piezoelectric coefficients are observed. Moreover, both materials possess nearly identical average *B*-site ionic radii; the average *B*-site ionic radius of PMN is equal to that of PZT with an atomic fraction of 46 % Ti. But whereas PMN possesses strong REFs, PZT is composed of homovalent Zr^{4+} and Ti^{4+} *B*-site cations and thus is representative of the weak REF limit.

Fig. 1(a) shows the temperature and frequency dependence of the real part of the dielectric permittivity of PMN. From 10^2 Hz to 10^5 Hz the peak permittivity shifts to higher temperature by 18 K; this behavior is the hallmark of all relaxors [3]. The same measurement made over the same frequency range on a single crystal specimen of PZT with $x = 0.325$ is shown in Fig. 1b, and no shift in temperature is evident. This dielectric response is consistent with that of a conventional ferroelectric phase transition near 600 K and shows that, despite the many similarities between PZT and PMN, PZT is not a relaxor. It is also consistent with the theoretical work of Grinberg *et al.* who used density functional theory to parameterize a phenomenological Landau model of the dielectric frequency dispersion. The parameters are the average *B*-site cation displacement from the high-symmetry cubic structure, D_B, and the second moment of the valence of the two *B*-site-cation nearest neighbors of each oxygen atom, $\langle V^2 \rangle$, which is a measure of the REF strength [2]. Using only these two input parameters, Grinberg *et al.* obtain quantitative agreement with all lead-based, perovskite relaxor systems for which both the local cation order and dielectric response have been measured. Interestingly, their model permits a frequency-dependent dielectric response even for materials where $\langle V^2 \rangle = 0$ (*i.e.*, for vanishingly small REF strength) provided that the average *B*-site cation displacement is not too large ($D_B < 0.11$ Å). In the case of PZT there is no frequency dependence, because D_B is large enough to stabilize long-range ferroelectric order. But there exist other disordered perovskite materials composed of homovalent *B*-site cations for which $\langle V^2 \rangle = 0$ and D_B is small that do exhibit a strongly frequency-dependent dielectric response. Examples include compositions of BZT with $0.25 < x < 0.42$ and BST with $0.20 < x < 0.50$, which retain an average cubic symmetry at all temperatures studied. The fundamental questions are then: (1) are REFs essential to the relaxor phase observed in the lead oxides, (2) what is the relaxor

[1]NIST Center for Neutron Research, National Institute of Standards and Technology, Gaithersburg, MD 20899
[2]University of Edinburgh, Edinburgh EH9 3JZ, UK
[3]University of Maryland, College Park, MD 20742
[4]Simon Fraser University, Burnaby, British Columbia V5A 1S6, Canada
[5]Oak Ridge National Laboratory, Oak Ridge, TN 37831

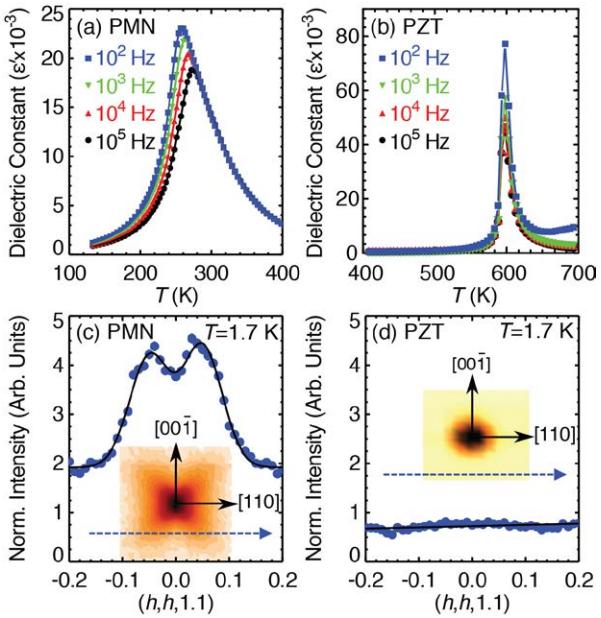

FIGURE 1: Temperature dependence of the real part of the dielectric permittivity measured along [001] for (a) PMN and (b) PZT ($x = 0.325$) at various frequencies. Neutron elastic diffuse scattering intensity measured at 1.7 K along [110] in the (HHL) scattering plane for (c) PMN and (d) PZT. The insets to (c) and (d) illustrate the shape of constant elastic-scattering-intensity contours measured near (001) in the (HHL) scattering plane for the same PMN and PZT crystals at, respectively, 300 K and 10 K, and are plotted on a log-intensity scale.

order parameter, and (3) do REFs play a role in the ultrahigh piezoelectric response?

We examined the neutron diffuse scattering from single crystals of PZT and PMN under exactly the same conditions to study the influence of REFs on the nanometer-scale structure of lead-oxide perovskite relaxors. To account precisely for the differences in crystal size and beam illumination, the diffuse scattering data from both crystals were normalized by the integrated intensity of a transverse acoustic (TA) phonon also measured under identical conditions. The data in Fig. 1(d) shows that the diffuse scattering for the non-relaxor PZT is at least a factor of 20 weaker than that in PMN. The inset in panel (d) shows a log-scale intensity map of the elastic scattering from the same PZT crystal at 10 K in the same (*HHL*) scattering plane near (001), and no evidence of diffuse scattering is present. As the dominant difference between PMN and PZT lies in the huge difference in REF strength, these neutron data establish a direct causal link between strong REFs and the temperature-dependent, anisotropic diffuse scattering from lead-oxide, perovskite relaxors shown in the inset to panel (c). In the same vein, the dielectric permittivity data demonstrate that strong REFs are responsible for the relaxor-like behavior. Together these results imply the existence of a fundamental connection between the relaxor phase and the anomalous temperature-dependent diffuse scattering. We thus identify the relaxor order parameter with the static, anisotropic diffuse scattering associated with short-range polar order, as it marks the transition temperature from the high-temperature paraelectric phase (where it is zero) into the low-temperature relaxor state (where it is non-zero). This identification is consistent with the ideas of Imry and Ma who showed that magnetic systems with continuous symmetry break up into short-range ordered domains in the presence of random magnetic fields. In relaxors like PMN long-range ferroelectric order is stifled by the formation of analogous polar domains on cooling. By contrast our data show that no such domains form in ferroelectric PZT because the REFs are too weak (or absent).

It is well known that pseudo-rhombohedral compositions of PMN-*x*PT and PZN-*x*PT located near the MPB exhibit enormous piezoelectric coefficients; the values of the longitudinal piezoelectric coefficient d_{33} for single-crystal MPB compositions poled along [001] can exceed 2500 pC/N and are the largest known. The concepts of polarization rotation and adaptive phases were proposed to explain the ultrahigh electromechanical response in MPB systems like PZT and PMN-*x*PT. However it has been shown that the integrated neutron elastic diffuse scattering intensity in PMN-*x*PT, which from the fluctuation-dissipation theorem is a measure of the static susceptibility, and d_{33} share a similar composition dependence; both properties peak near the MPB and then drop precipitously in the tetragonal (Ti-rich) regime in which the relaxor phase is replaced by a conventional ferroelectric phase. Given our finding that PZT exhibits essentially no such diffuse scattering, one might expect that the corresponding value of d_{33} in PZT should be significantly smaller than that in PMN-*x*PT. We find that this is indeed true; the maximum value of d_{33} we measured for MPB compositions of [001]-poled PZT single crystals is 1,200 pC/N [3]. Thus the optimal values of d_{33} in single-crystal PMN-*x*PT and PZN-*x*PT are approximately 100 % greater than those in single-crystal PZT. Insofar as PZT and PMN-*x*PT are highly similar save for the strength of the REFs, our results indicate that the underlying nanometer-scale, static, polar order in relaxors that is associated with the temperature-dependent diffuse scattering plays a seminal role in greatly amplifying the piezoelectric response beyond that in the non-relaxor PZT, which does not exhibit an equivalent nanometer-scale polar order. This behavior is not without precedent. In single crystals of highly magnetostrictive Galfenol (an alloy of magnetic Fe and non-magnetic Ga), a material that is often likened to a magnetic relaxor, both the neutron elastic diffuse scattering intensity and the longitudinal magnetostrictive coefficient λ_{100} increase dramatically as the system is doped towards a phase boundary and then decrease sharply as the boundary is crossed [4].

References

[1] I. Grinberg, P. Juhàs, P. K. Davies, A. M. Rappe, Phys. Rev. Lett. **99**, 267603 (2007).
[2] A. R., Akbarzadeh, S. Prosandeev, E. J. Walter, A. Al-Barakaty, L. Bellaiche, Phys. Rev. B **108**, 257601 (2012).
[3] D. Phelan *et al.*, Proc. Natl. Acad. Sci. USA, in press.
[4] H. Cao *et al.*, Phys. Rev. Lett. **102**, 127201 (2009).

BH_4^- reorientational dynamics in $LiBH_4$: effects of iodide substitution and nanoconfinement

N. Verdal[1,2], T. J. Udovic[1], and J. J. Rush[1,2]

The tetrahydroborate anion, BH_4^-, has been actively investigated as a potential entity for hydrogen storage on-board hydrogen fuel cell powered vehicles due to an inherently favorable hydrogen mass fraction. As such, the lighter-metal borohydrides have undergone particularly intense scrutiny, although in their pristine states they display generally unfavorable hydrogen-cycling behavior. It has been a goal of a number of recent quasielastic neutron scattering (QENS) and NMR experiments to better understand this behavior and unravel the mechanistic details of BH_4^- reorientations in these materials in their pristine as well as chemically or morphologically altered states. For $LiBH_4$, the lightest and best studied metal borohydride, there are lingering uncertainties with respect to how the reorientational mechanisms and mobilities are perturbed by either halide anion substitution (most notably, I^-) or confinement in nanopores, two potential strategies for ameliorating the thermodynamics, kinetics, and reversibility of dehydrogenation/hydrogenation. QENS, vibrational spectroscopy, and diffraction probes have been recently used at the NCNR over a wide range of wavevector and temperature to clarify reorientational behavior in these modified systems [1,2].

Whereas orthorhombic $LiBH_4$ exhibits a transition at 385 K to a hexagonal structure with much more rapid reorientational dynamics, the mixed salts maintain such a structure to very low temperatures with even more rapid reorientations. We have synthesized a $^7Li^{11}BH_4$-LiI solid solution, verified its hexagonal structure down to 4 K, and measured QENS spectra using both the DCS and HFBS spectrometers over a momentum transfer (Q) range of 0.2 $Å^{-1}$ to 6.5 $Å^{-1}$ and at resolutions between 0.8 μeV and 1000 μeV. Results have been compared with similar measurements for pure a $^7Li^{11}BH_4$. Elastic scattering scans measured on HFBS for $LiBH_4$ and $LiBH_4$-LiI are shown in Fig. 1, which illustrate the great change in the onset of neutron sensitive ($10^{-9}s^{-1}$) reorientational dynamics with iodide substitution. In fact, the very broad dynamical range of the 1:1 mixed salt allows us to probe reorientations within the hexagonal phase down to very low temperatures.

The incoherent scattering function, $S(Q,\omega)$, for $LiBH_4$-LiI (and for $LiBH_4$) includes a combination of elastic, $A_0(Q)$, and quasielastic, $A_i(Q)$, scattering as described by the expression:

$$S(Q,\omega) = A_0(Q)\delta(\omega) + \sum A_i(Q)L_i(\omega), \quad (1)$$

whose functional forms are determined by the geometric details of the reorientational (or translational) motions of the BH_4^- ions [1,2]. The elastic and quasielastic lineshapes can be represented by delta, $\delta(\omega)$, and Lorentzian, $L_i(\omega)$, functions respectively. The measured spectrum at 125 K is shown in Fig. 2a, which can best be fitted using two Lorentzian components, combined with an elastic peak. The elastic incoherent structure factor, $A_0(Q)$, for these results shows a dramatic change in reorientational mechanism over a narrow temperature range, from a one-dimensional delocalized "orbit" motion of the three trigonal H atoms, with the fourth axial BH_4^- proton "immobile" (orbit model) at 125 K, to the additional "jump-exchange" of the axial protons with the orbiting trigonal H atoms (orbit-exchange model) by 200 K (Fig. 2b). This ability to track changes in reorientational motions is a vivid illustration of the power of the QENS technique. Raising the temperature to 250 K and measuring the $A_0(Q)$with 1.7 Å neutrons to provide an extended Q range up to 6.4 $Å^{-1}$ allows us to corroborate the more delocalized nature of the orbiting trigonal H atoms (green), ruling out the more discrete six-fold C_6-localized orbit-exchange model (maroon). Also shown is the measured $A_0(Q)$ for $LiBH_4$ at a much higher temperature, which closely resembles the mixed-salt result.

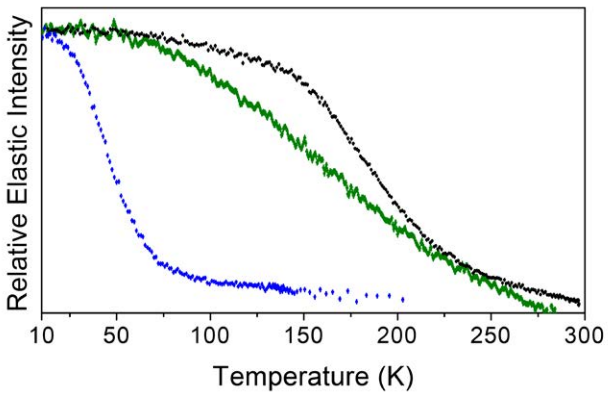

FIGURE 1: The elastic scattering intensity of bulk $LiBH_4$ (black), $LiBH_4$-LiI (blue), and $LiBH_4$ in 4 nm carbon pores (green) as a function of temperature. Vertical error bars in all figures denote ± 1σ.

[1] NIST Center for Neutron Research, National Institute of Standards and Technology, Gaithersburg, MD 20899
[2] University of Maryland, College Park, MD 20742

In addition to $LiBH_4$ in a mixed crystal, we have recently extended our measurements to a study of $LiBH_4$ confined in nanoporous carbon (NPC) materials, including NPCs possessing 4 nm diameter, hexagonally arranged, cylindrical pores [1]. The neutron vibrational spectra measured for the $LiBH_4$ in NPCs show a distinct broadening of the BH_4^- torsional band compared to bulk $LiBH_4$, which clearly indicates a change in reorientational dynamics. Moreover, the measurement of quasielastic spectra on the NPCs using both HFBS and DCS spectrometers again allowed us to follow the BH_4^- reorientational behavior over a wider range of temperature. As shown in Fig. 1, the temperature region for "neutron sensitive" reorientational dynamics of $LiBH_4$ in 4 nm NPC begins lower and is more extensive than for pure $LiBH_4$.

The nature of the BH_4^- quasielastic scattering in the NPC is different from either pure $LiBH_4$ or the $LiBH_4$-LiI compound. The best fit to the quasielastic data requires two Lorentzian components, roughly an order of magnitude apart in width. It is thus most probable that they represent two independent populations of BH_4^- anions in very different environments. In Fig. 3a, we plot the $A_0(Q)$ derived from the results at 330 K, a temperature at which the two quasielastic components have about the same intensity. This strongly suggests that the two BH_4^- populations are associated with a bulk-like interior region reorienting at a slower rate and an interfacial layer reorienting at a significantly greater rate (see Fig. 3a inset), with an average thickness of ≈ 0.6 nm. The $A_0(Q)$ at 330 K (diamonds) is well fit by a model describing two-fold or three-fold jumps around a single axis; while at 400 K (stars), it is best fit by a three-dimensional rotational diffusion model. As the temperature is raised above 330 K, both components become more rotationally diffusive. Moreover, at 400 K, the fraction of faster reorientations increases, suggesting either an increased 1 nm interfacial thickness, or the transition of some of the interior $LiBH_4$ from a reorientationally slow orthorhombic structure to a reorientationally more rapid hexagonal structure. Finally, in Fig. 3b we show the Arrhenius plots of the linewidths for both quasielastic features of $LiBH_4$ confined in a 4 nm pore, compared to the results for pure $LiBH_4$. The linewidth for the broader quasielastic component is distinct from the narrower component and similar in width to the limited results shown for the high-temperature hexagonal phase of $LiBH_4$. The reorientational activation energies determined from an Arrhenius fit for $LiBH_4$ in 4 nm NPC are (16 ± 1) kJ/mol and (10.6 ± 0.7) kJ/ mol, demonstrating the great change in BH_4^- dynamics from the core to interfacial region, and somewhat reduced from the (19.2 ± 0.8) kJ/mol determined for the bulk.

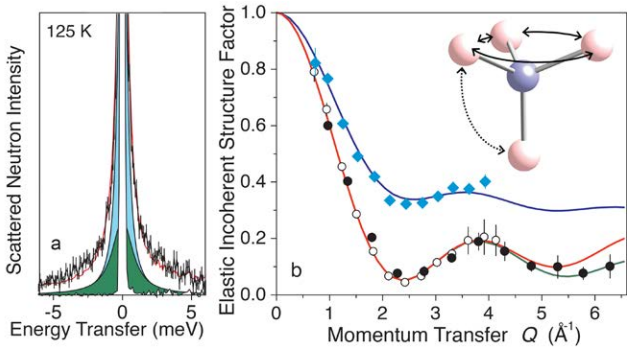

FIGURE 2: a) The QENS spectrum of $LiBH_4$-LiI at 125 K with 2.75 Å wavelength neutrons collected at $Q = 2.4$ Å^{-1} (black), with the fitted function (red), consisting of a delta (white) and two Lorentzian (blue and green) functions. **b)** The observed $A_0(Q)$ for $LiBH_4$-LiI at 125 K (blue diamonds), and 250 K (black circles), compared with the orbit model (blue line), the orbit-exchange model (green line), and the C_6-localized orbit-exchange model (maroon line). A schematic of BH_4 reorientational jumps is depicted in the inset. The observed $A_0(Q)$ for bulk $LiBH_4$ at 400 K (open circles) is shown for comparison.

These results exemplify the utility of high-Q QENS measurements to track the mechanistic evolution of molecular reorientations in general. For the current systems, modified BH_4^- dynamics turns out to be a sensitive indicator of non-bulk-like $LiBH_4$ perturbations due to either iodide substitution or nanoconfinement. The relationship between these perturbations and modified hydrogen storage and release properties is yet to be determined.

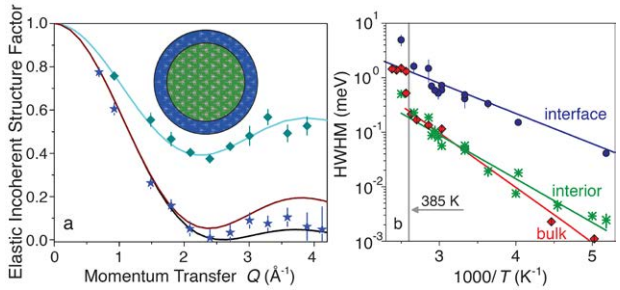

FIGURE 3: a) The $A_0(Q)$ of $LiBH_4$ confined in a 4 nm carbon pore at 330 K (dark cyan diamonds) compared with a $C_2|C_3$ reorientational jump model (cyan), and at 400 K (blue stars) compared with the C_6-localized orbit-exchange model (maroon) and isotropic rotational diffusion (black). The inset is a schematic of $LiBH_4$ confined in a 4 nm pore carbon scaffold. **b)** An Arrhenius plot of quasielastic linewidths of $LiBH_4$ at the interface (blue), and the interior (green) of a 4 nm carbon pore are compared with bulk $LiBH_4$ (red).

References

[1]. N. Verdal, T.J. Udovic, J.J. Rush, X. Liu, E.H. Majzoub, M.R. Hartman, J.J. Vajo, A.F. Gross, J. Phys. Chem. C **117** (35) 17983 (2013).

[2]. N. Verdal, T.J. Udovic, J.J. Rush, H. Wu, A.V. Skripov, J. Phys. Chem. C **117**, 12010 (2013).

Fractionalized excitations in a spin-1/2 kagome lattice antiferromagnet

T.-H. Han[1], J. S. Helton[2], S. Chu[1], D. G. Nocera[1], J. A. Rodriguez-Rivera[2,3], C. Broholm[2,4], and Y. S. Lee[1]

Materials with atomic magnetic moments arranged on a crystalline lattice are ubiquitous in nature and have numerous technological applications. Typically these materials will display long range magnetic order at low temperatures. However, some two-dimensional lattices instead give rise to a new state of quantum magnetic matter: the spin liquid. A quantum spin liquid has a magnetic ground state that displays strong short range fluctuating spin correlations but no static order down to low temperatures, despite strong antiferromagnetic interactions between neighboring spins. Neutron scattering measurements on $ZnCu_3(OD)_6Cl_2$, also known as herbertsmithite, have revealed a continuous energy spectrum of magnetic fluctuations [1] – evidence of fractionalized quasiparticles in the spin liquid ground state of this frustrated magnet.

Quantum spin liquids have attracted a great deal of attention in condensed matter physics since Anderson's seminal proposal of the "resonating valence bond" state four decades ago [2], yet real materials displaying this ground state are rare. A particularly promising system in which to search for spin liquid physics is the spin-1/2 kagome lattice antiferromagnet. The strong quantum fluctuations inherent to spin-1/2 moments and the extensive ground state degeneracy of antiferromagnetically interacting spins on the kagome lattice (Fig. 1) combine to destabilize long range order. The mineral herbertsmithite, $ZnCu_3(OD)_6Cl_2$, features spin-1/2 Cu^{2+} ions arranged on a kagome lattice with successive layers magnetically isolated by layers of diamagnetic Zn^{2+} ions. Magnetic susceptibility measurements display a Curie-Weiss temperature of -300 K, which indicates strong nearest neighbor antiferromagnetic interactions ($J \approx 17$ meV). Previous work on powder samples of herbertsmithite [3] revealed short range dynamic spin correlations with no sign of an energy gap in the excitation spectrum or of long range magnetic order down to mK temperatures. While the low energy dynamics of herbertsmithite appear to be complicated by magnetic Cu^{2+} impurities occupying sites in the nominally diamagnetic Zn layers, this material remains the best realization of the spin-1/2 kagome lattice available for experimental study and one of only a few materials with a quantum spin liquid ground state.

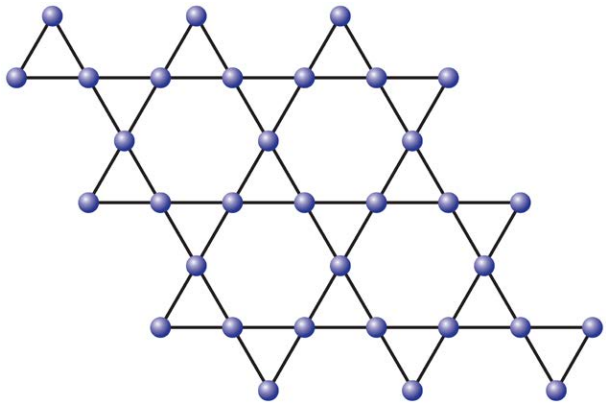

FIGURE 1: The kagome lattice, consisting of corner-sharing triangles. In herbertsmithite, spin-1/2 copper ions are arranged on a kagome lattice with an antiferromagnetic ($J \approx 17$ meV) interaction between nearest-neighbor spins.

Many early neutron spectroscopy measurements on $ZnCu_3(OD)_6Cl_2$ were carried out on powder samples. However, powder experiments can be ambiguous because the direction of the neutron's momentum change with respect to the crystalline lattice is unknown. In order to carry out more precise measurements, single crystal samples of herbertsmithite were synthesized through a new chemical process that involved tubes of dissolved precursor material subjected to slight temperature gradients where the sample synthesis was allowed to proceed for up to 10 months. This method succeeded in producing multiple single crystal samples of herbertsmithite with masses up to 320 mg. Fifteen samples were co-aligned on an aluminum sample holder, producing a total sample of 1.2 g suitable for neutron spectroscopy.

Neutron spectroscopy measurements on this single crystal sample were carried out using the Multi-Axis Crystal Spectrometer (MACS). MACS allows researchers to map out short range spin correlations by measuring the dynamic

[1]Massachusetts Institute of Technology, Cambridge, MA 02139
[2]NIST Center for Neutron Research, National Institute of Standards and Technology, Gaithersburg, MD 20899
[3]University of Maryland, College Park, MD 20742
[4]The Johns Hopkins University, Baltimore, MD 21218

structure factor, $S(Q, \omega)$, over a broad swath of reciprocal space, Q, at a few fixed energy transfers ($\hbar\omega$). The dynamic structure for herbertsmithite, cooled to 1.6 K, is shown for energy transfers of 6 meV (Fig. 2a) and 2 meV (Fig. 2b). These data confirm that the ground state of herbertsmithite features dynamic short-range correlations, as they lack the sharp spin wave dispersion features that would arise for an ordered magnet. Even non-frustrated magnets without long range magnetic order at low temperatures, such as the spin-1/2 square lattice antiferromagnet La_2CuO_4, develop significant antiferromagnetic correlations and display low energy scattering that is peaked near specific points in Q space. The low energy spin dynamics in herbertsmithite, however, give rise to broad ridges of magnetic neutron scattering that extend over several Brillouin zones. The neutron scattering pattern is quite similar to that expected from uncorrelated nearest-neighbor antiferromagnetic dimers (Fig. 3), though the experimental ridges are narrower in Q space suggesting spin-correlations beyond the nearest neighbor.

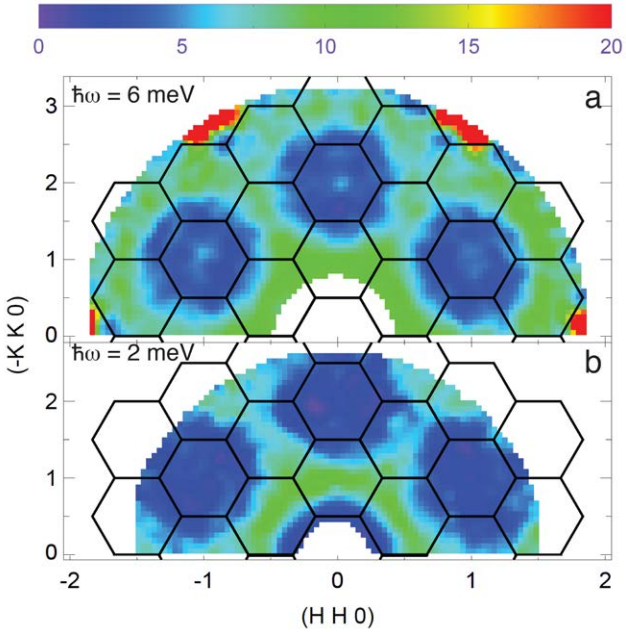

FIGURE 2: Dynamic structure factor of herbertsmithite at 1.6 K measured on the MACS spectrometer, with energy transfers of 6 meV (a) and 2 meV (b). The color scale is given by the bar on top, in units of barn/(eV steradian formula unit).

A further hallmark of a quantum spin liquid is the presence of exotic quasiparticle spin excitations carrying fractional quantum numbers. While the conventional spin wave excitations of an ordered magnet carry a spin quantum number of $S = 1$, the spinon excitations predicted for a quantum spin liquid consist of multiple spin-half ($S = 1/2$) excitations into which spin waves fractionalize. These exotic excitations have been previously observed in one-dimensional spin chains such as $KCuF_3$, but have not been observed in two-dimensional magnetic systems. Since a neutron scattering experiment which generates $\Delta S = \pm 1$ excitations based on quantum selection rules will excite multiple spinons simultaneously, the resulting spectrum will feature a broad continuum of scattering extending over energy transfers from zero up to a maximum comparable to the exchange interaction J. The measured spectrum of $ZnCu_3(OD)_6Cl_2$ fits this prediction, as a continuum of inelastic scattering is observed with a Q-space pattern similar to that shown in Fig. 2 stretching up to energy transfers of at least 11 meV.

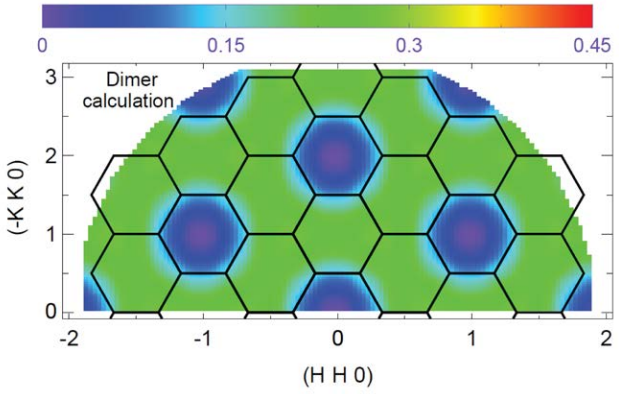

FIGURE 3: Calculated structure factor for uncorrelated nearest-neighbor dimer singlets on a kagome lattice.

In two-dimensional antiferromagnets the combination of geometric frustration where the triangular plaquettes of the lattice prevent any simple collinear order and strong quantum fluctuations can lead to novel ground states of quantum magnetic matter such as the spin liquid. The spin-1/2 Heisenberg antiferromagnet on the kagome lattice is a well-studied theoretical model expected to display such an exotic ground state. We conclude that the mineral $ZnCu_3(OD)_6Cl_2$ (herbertsmithite) is well described by this model and displays a spin liquid ground state with fluctuating short range correlations and no long range order down to the lowest temperatures measured. The spectrum of neutron scattering at fixed momentum transfer is a broad continuum extending to at least 11 meV. This is arguably the first experimental evidence for fractionalized excitations in a two-dimensional magnet, confirming an important prediction regarding quantum spin liquids and providing a starting point for further theories on quantum magnetism.

References

[1] T.-H. Han, *et al.*, Nature **492**, 406 (2012).
[2] P. W. Anderson, Mater. Res. Bull. **8**, 153 (1973).
[3] J. S. Helton, *et al.*, Phys. Rev. Lett. **98**, 107204 (2007); P. Mendels, *et al.*, Phys. Rev. Lett. **98**, 077204 (2007).

Novel coexistence of half-metallic itinerant ferromagnetism with local-moment antiferromagnetism in $Ba_{0.60}K_{0.40}Mn_2As_2$

A. Pandey[1], B. G. Ueland[1], S. Yeninas[1], A. Kreyssig[1], A. Sapkota[1], Y. Zhao[2,3], J. S. Helton[2], J. W. Lynn[2], R. J. McQueeney[1], Y. Furukawa[1], A. I. Goldman[1], and D. C. Johnston[1]

The discovery of high-temperature superconductivity in iron pnictides in 2008 [1] opened up an entirely new system for exploring insulating or narrow-band metallic behavior since some of these materials display aspects of both local-moment and itinerant magnetism. An important related material is $BaMn_2As_2$, which has the same tetragonal crystal structure as the high-temperature superconductor parent compound $BaFe_2As_2$. $BaMn_2As_2$ has an insulating ground state exhibiting collinear local-moment antiferromagnetic (AFM) order below $T_N = 625$ K. Each isotropic, $S = 5/2$ Mn^{2+} ion has an ordered magnetic moment $\mu = 3.9\ \mu_B$/Mn which is oppositely directed to the moment of each of its nearest-neighbor Mn^{2+} ions [2]. $BaMn_2As_2$ can be made metallic by substituting K for Ba to form hole-doped $Ba_{1-x}K_xMn_2As_2$ [3,4]. In this system we have discovered a novel magnetic structure at low temperatures in single crystals of metallic $Ba_{0.60}K_{0.40}Mn_2As_2$ [5]. This structure consists of ferromagnetism (FM) of the itinerant doped holes below a Curie temperature $T_C \approx 100$ K along with collinear Mn local-moment AFM ($T_N = 480$ K), where the ordered moments in the two magnetic structures are aligned *perpendicular* to each other. Furthermore, the FM at $T \rightarrow 0$ arises from complete spin polarization of the doped holes, called half-metallic FM. This FM component was not present in the previously studied samples of $Ba_{1-x}K_xMn_2As_2$ with K concentrations of $x = 0.016$ and $x = 0.05$ [3]. It is qualitatively different from the half-metallic FM in $La_{1-x}Ca_xMnO_3$, for example, [6] where the conduction electron moments are polarized by strong coupling to the FM-ordered local Mn moments and hence align *parallel* to them.

The local-moment magnetism of $Ba_{1-x}K_xMn_2As_2$ is very robust, with an ordered moment that is nearly constant at $\mu \approx 4.0\ \mu_B$/Mn as the doping level changes from the insulating composition $x = 0$ to metallic compositions from $x = 0.016$ to $x = 0.40$ (the range studied). The moments are oriented along the c-axis throughout the doping series [7]. Furthermore, the T_N associated with the Mn local moments decreases by only 20 % from 625 K for $x = 0$ to 480 K for $x = 0.40$. Due to this robust nature of the Mn local-moment AFM, the anisotropy of the magnetic susceptibility $\chi(T)$ of $Ba_{0.60}K_{0.40}Mn_2As_2$ was expected to be small and similar to that of undoped $BaMn_2As_2$ [2]. Surprisingly, the χ_{ab} with H || *ab*-plane instead exhibits a huge enhancement on cooling

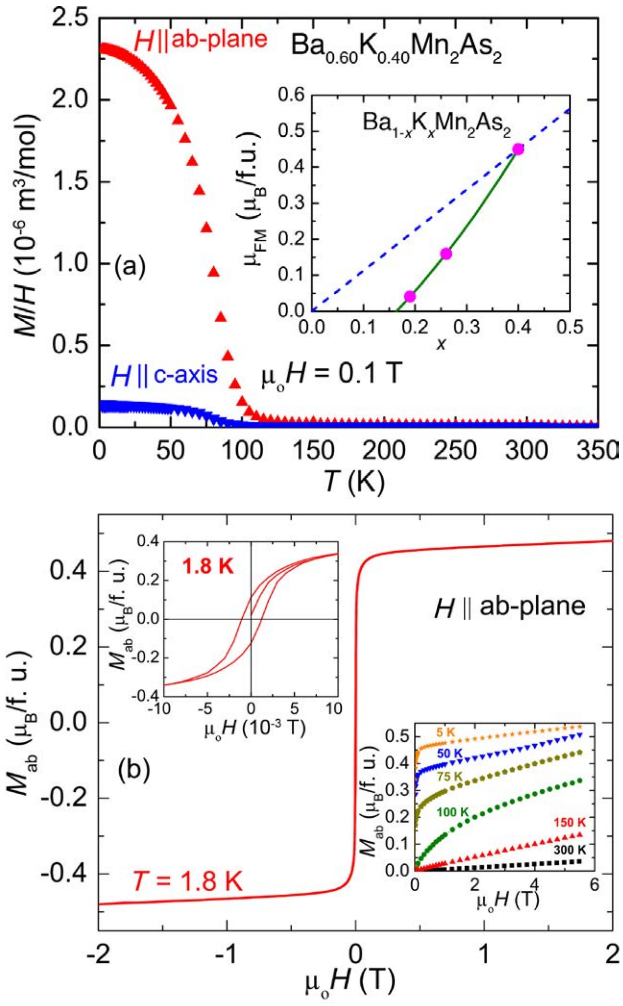

FIGURE 1: (a) Magnetic susceptibility $\chi = M/H$ versus T of $Ba_{0.60}K_{0.40}Mn_2As_2$ [5]. Inset: FM ordered moment μ_{FM} at low T versus x in $Ba_{1-x}K_xMn_2As_2$ [5,6]. The dashed line is the expected behavior for full doped-hole spin polarization with $\mu_{FM} = xgS\ \mu_B$/f.u., $g = 2.25$ and $S = 1/2$ (f.u. means formula unit). **(b)** M_{ab} versus H at 1.8 K [5]. Upper inset: Expanded plot of $M_{ab}(H)$ at 1.8 K. Lower inset: $M_{ab}(H)$ isotherms between 5 K and 300 K.

[1]Ames Laboratory and Iowa State University, Ames, IA 50011
[2]NIST Center for Neutron Research, National Institute of Standards and Technology, Gaithersburg, MD 20899
[3]University of Maryland, College Park, MD 20742

below 100 K as shown in Fig. 1(a), indicating the occurrence of a FM transition below $T_C \approx 100$ K with the FM ordered moments oriented in the *ab*-plane [the $\chi_c(T \rightarrow 0)$ value is attributed to a small ($\approx 4^\circ$) misalignment of the field with the *c*-axis of the crystal]. This FM below 100 K coexists with the AFM ordering of the Mn spins that exhibit AFM ordering below $T_N = 480$ K.

The FM is confirmed in Fig. 1(b) from $M_{ab}(H)$ measurements at 1.8 K. The data show that $M_{ab}(H)$ very quickly saturates to a nearly constant value at fields above about 10 mT. Extrapolating the high-field linear behavior to zero gives $\mu_{FM}(T = 1.8\ \text{K}) = 0.45(1)\ \mu_B$/f.u. The expanded plot in the upper inset shows that the FM is extremely soft since the saturation is nearly complete at 10 mT and the coercive field is only about 1 mT. $M_{ab}(H)$ isotherms obtained both above and below 100 K are shown in the lower inset of Fig. 1(b). The FM spontaneous magnetization is clearly visible in the isotherms at 75 K and below.

One possible explanation for the in-plane FM below T_C in $Ba_{0.60}K_{0.40}Mn_2As_2$ originates from canting (tilting) of the already-established Mn ordered moments ($T_N = 480$ K) along the *c*-axis towards the *ab*-plane. However, ^{75}As NMR data argue against this possibility [5], and such a canting would also require a lattice distortion to remove the inversion center between the Mn atoms, which is not detected in high-resolution x-ray diffraction measurements down to 10 K [5]. To rule out this canting possibility unambiguously and to directly observe this new FM, field-dependent neutron diffraction data were obtained on BT-7, and the data for $T = 5$ K are shown in Fig. 2 [5]. Similar intensity increases are observed for a number of reflections, but the (101) peak seen in Fig. 2(d) is of special importance since FM ordering of the Mn local moments will only contribute to Bragg peaks with $h + k$ even and ℓ even. Thus the increase in these intensities cannot be due to a canting of the Mn moments, and therefore must be due to FM ordering of the itinerant doped holes. As shown in the inset of Fig. 1(a), the saturation moment of all the doped hole spins agrees quantitatively with the observed value for $T \rightarrow 0$. This type of itinerant FM is called half-metallic, which interpretation is also supported by a fit to the electrical resistivity measurements.

In summary, our magnetization, NMR, electrical resistivity, and x-ray and neutron diffraction measurements of $Ba_{0.60}K_{0.40}Mn_2As_2$ crystals reveal that this compound exhibits a novel magnetic structure in which half-metallic FM coexists with local-moment AFM of the Mn spin lattice, where the ordered moments of these two magnetic substructures are perpendicular to each other. The microscopic origin of the surprising half-metallic itinerant FM, and the mechanism behind the perpendicular alignment of the FM and AFM ordered magnetic structures, are interesting new questions to be explored.

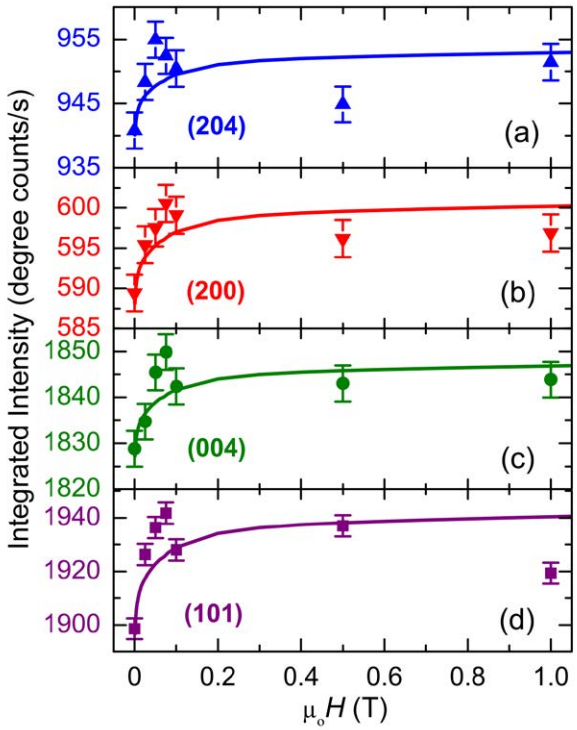

FIGURE 2: Integrated intensity versus *H* for four Bragg peaks at $T = 5$ K. The curves are fits to the $M_{ab}^2(H)$ data in Fig. 1(b). Uncertainties are statistical in origin and represent one standard deviation.

References

[1] D. C. Johnston, Adv. Phys. **59**, 803 (2010).

[2] D. C. Johnston, R. J. McQueeney, B. Lake, A. Honecker, M. E. Zhitomirsky, R. Nath, Y. Furukawa, V. P. Antropov, Y. Singh, Phys. Rev. B **84**, 094445 (2011).

[3] A. Pandey, R. S. Dhaka, J. Lamsal, Y. Lee, V. K. Anand, A. Kreyssig, T. W. Heitmann, R. J. McQueeney, A. I. Goldman, B. N. Harmon, A. Kaminski, D. C. Johnston, Phys. Rev. Lett. **108**, 087005 (2012).

[4] J.-K. Bao, H. Jiang, Y.L. Sun, W.-H. Jiao, C.-Y. Shen, H.-J. Guo, Y. Chen, C.M. Feng, H.-Q. Yuan, Z.-A. Xu, G.-H. Cao, R. Sasaki, T. Tanaka, K. Matsubayashi, Y. Uwatoko, Phys. Rev. B **85**, 144523 (2012).

[5] A. Pandey, B. G. Ueland, S. Yeninas, A. Kreyssig, A. Sapkota, Y. Zhao, J. S. Helton, J. W. Lynn, R. J. McQueeney, Y. Furukawa, A. I. Goldman, D. C. Johnston, Phys. Rev. Lett. **111**, 047001 (2013).

[6] Y. Tokura, Rep. Prog. Phys. **69**, 797 (2006).

[7] J. Lamsal, G. S. Tucker, T. W. Heitmann, A. Kreyssig, A. Jesche, A. Pandey, W. Tian, R. J. McQueeney, D. C. Johnston, A. I. Goldman, Phys. Rev. B **87**, 144418 (2013).

Phonon-driven superconductivity in the vicinity of ferroelectric and charge density wave (CDW) ordering in $La(O,F)BiS_2$

T. Yildirim[1, 2]

Superconductivity – a phenomenon first documented in 1911 – remains one of the most challenging subjects of condensed matter physics. Very recently a new family of layered materials containing BiS_2 planes [1] was discovered to be superconducting at temperatures up to 10 K. These new systems $REO_xF_{1-x}BiS_2$ (RE=La, Nd, Pr, and Ce) are structurally similar to the layered, iron-based superconductors $LaO_xF_{1-x}FeAs$, and in both cases the superconductivity is achieved by F-doping. This similarity has raised the exciting question of whether or not the superconducting mechanism in the BiS_2 system is related to that in the iron pnictides.

The fundamental question is whether or not the observed T_c in this new system can be understood within a conventional electron-phonon (el-ph) coupling framework, or is a more exotic mechanism responsible for the superconducting pairing? In this study, [2] we present state-of-the-art first principles calculations that directly address this question. We find that BiS_2 is a strong electron-phonon coupled superconductor in close proximity to competing ferroelectric and CDW phases. Our results suggest new directions with which to tune the balance between these phases and increase T_c in this new class of materials.

Fig. 1 shows the tetragonal cell of $LaO_xF_{1-x}BiS_2$, which consists of two types of atomic layers; namely the LaO spacer and electronically active BiS_2 bilayer. Upon replacing some of the oxygen atoms in the LaO layer with F, one can control the charge transfer to BiS_2 bilayer and thus tune the electronic properties as shown in Fig. 1. The undoped parent compound is a band-insulator with a gap of ≈ 1 eV. Upon electron doping, we start to fill the empty states in a rigid-band fashion, turning the insulating parent compound into a metallic system. The density of states (DOS) at the Fermi level, $N(E_F)$, increases with increasing electron doping and becomes maximal at the half filling $x = 0.5$.

One of the most interesting results shown in Fig. 1 is that $N(E_F)$ is quite high at half-filling ($x = 0.5$) and E_F coincides with a peak in the density of states. This usually suggests some sort of instability due to a Van Hove singularity. In order to check this, we calculated [2] phonon dispersion curves of the parent ($x = 0$) and half doped ($x = 0.5$) systems. To our

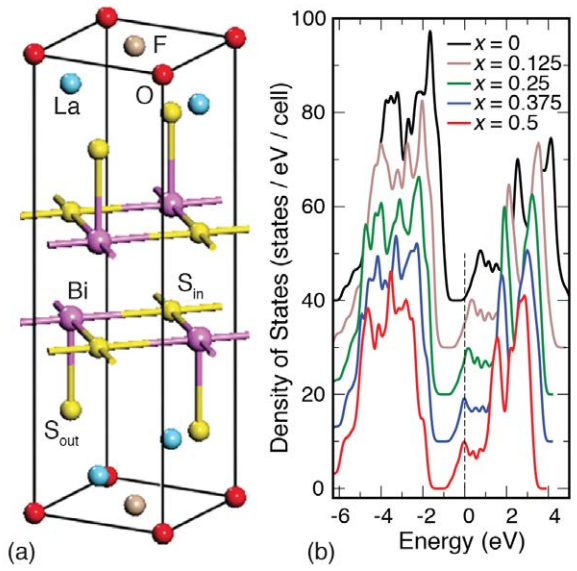

FIGURE 1: (a) Crystal structure of $LaO_xF_{1-x}BiS_2$ ($x = 0.5$). (b) Electronic DOS of $LaO_xF_{1-x}BiS_2$ as a function of F-doping x. For clarity the curves are shifted vertically except $x = 0.5$.

surprise, we find that the undoped system shows instability near the center of the Brillouin zone while the doped system has instabilities at $M(\pi, \pi)$. In order to have a better insight into the nature of these unstable phonons, we carried out total energy calculations as the system was distorted by the modes having the most negative energy. Fig. 2a shows the most unstable soft phonon $\boldsymbol{E_u}$ at the center of the Brillouin zone for $x = 0$. The S atoms move towards Bi atoms along a- or b-axis (two –fold degenerate) and slightly lower the energy of the system by ≈ 1 meV. It is remarkable that in the distorted phase, the inversion symmetry is broken and a large spontaneous polarization of $P = 9.9\ \mu C/cm^2$ is induced despite the rather small displacements. However, solving the Schrödinger equation for this shallow potential, we obtained energy levels that are above the potential minimum. Hence, the system should be dynamically disordered due to zero-point motions and should appear as tetragonal.

Fig. 2b shows the total energy in the $\sqrt{2} \times \sqrt{2}$ cell of the tetragonal structure for $x = 0.5$ as it is distorted according to the most negative energy phonon at (π, π). Unlike the

[1]NIST Center for Neutron Research, National Institute of Standards and Technology, Gaithersburg, MD 20899
[2]University of Pennsylvania, Philadelphia, PA 19104

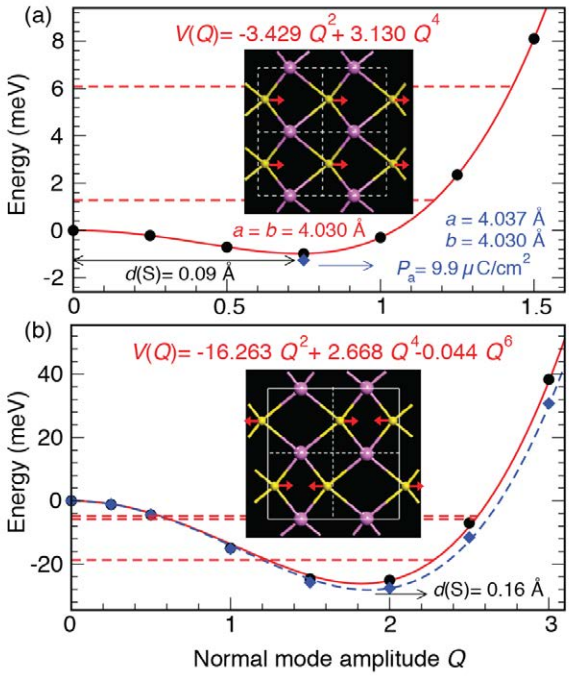

FIGURE 2: Total energy as the system is distorted by the most negative energy phonons in the tetragonal cell of $LaOBiS_2$ at the center of the Brillouin zone (top) and in the $\sqrt{2} \times \sqrt{2}$ cell of $LaO_{0.5}F_{0.5}BiS_2$ (bottom). The insets show the sketch of the unstable phonons. Horizontal dashed red lines show the energy levels of the one-dimensional potential (red curve). The calculated polarization, lattice parameters and the displacement of S atom are also indicated.

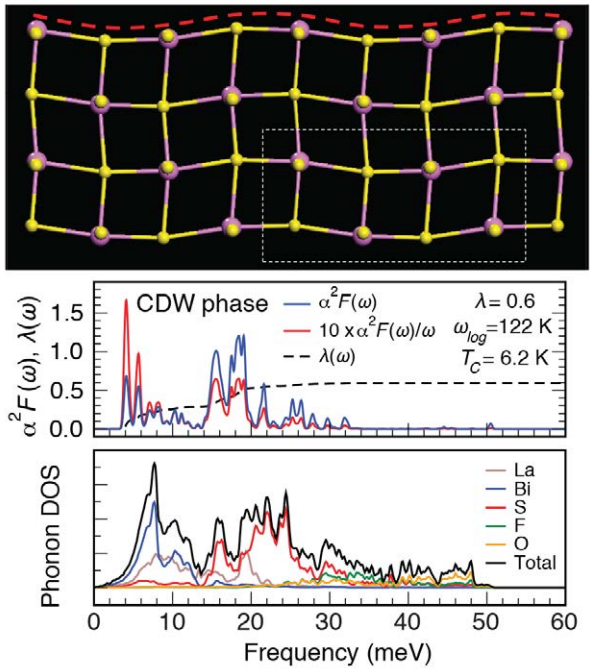

FIGURE 3: Top: The optimized structure of the BiS_2 plane in the $\sqrt{2} \times \sqrt{2}$ CDW phase of $LaO_{0.5}F_{0.5}BiS_2$. Large pink and small yellow spheres are Bi and S, respectively. Dashed red line is to guide the eye, indicating the sinusoidal distortion of the atoms. The white rectangle indicates the unit cell of the CDW phase. Middle: Eliashberg functions in the fully optimized CDW structure (top). El-ph coupling constant, λ, T_c, and ω_{log} are also given. The total and atomic-projected phonon DOS are shown in the bottom panel.

parent compound, the distortion lowers the system energy significantly, causing S atoms to move away by 0.16 Å from the high symmetry site. Solving the resulting one-dimensional potential curve numerically, we obtained the energy levels, which are bound to the local minimum of the distortion. Hence, unlike the $x = 0$ case, DFT calculations predict that the $x = 0.5$ system should distort from tetragonal symmetry. Indeed, we determined that the fully stable optimized structure has the $\sqrt{2} \times \sqrt{2}$ unit cell with symmetry $P2212$ and that it shows a rather interesting rearrangement of Bi and S atoms in the BiS_2 plane, as shown in Fig. 3. We denote this distorted structure as the CDW phase, due to the sinusoidal distortion of the Bi and S atoms as shown by red dashed lines in Fig. 3.

We next address the nature of superconductivity found in these BiS_2 layered systems. We calculate the el-ph coupling in the CDW phase by the frozen-phonon method. The results are summarized in Fig. 3. We obtain quite large electron-phonon coupling $\lambda = 0.6$ and a logarithmic frequency average $\omega_{log} = 122$ K, which gives a T_c of 6 K. This value is in excellent agreement with the reported experimental values of T_c that vary from 3 K to 10 K, depending on the level of doping. Inspecting the modes which give the highest el-ph coupling, we estimate that about 90 % of λ comes from in-plane Bi and S phonons while the remaining 10 % is due to phonons along the c-axis. There are two bands of phonons near (5 to 10) meV and (15 to 25) meV. The phonons in the lower energy band are due to coupled Bi and S motion while the phonons in the high energy bands are due to almost pure S oscillations. In Fig. 3, we also show the total phonon density of states along with the atomic-projections of the DOS.

In conclusion, we have discovered rather unusual structural and dynamical properties of $LaOBiS_2$ with electron doping. The large-amplitude in-plane S-atom displacement controls the structural properties and gives rise to large el-ph coupling. It would be interesting to measure the isotope effect for the S atom, which may be unconventional. Our results also suggest that thin films of BiS_2 on various substrates may exhibit unusual properties due to epitaxial strain at the interface. New materials with similar structures but with BiS_2 plane could be quite interesting due to smaller mass of oxygen atom, which gives higher phonon energies, and in turn higher T_c. It is too early to say which of these predictions from our calculations will be demonstrated experimentally. However it is clear that the BiS_2 based layered systems are very rich in physics, involving nearly ferroelectric soft phonons and CDW ordering along with strongly coupled electron-phonon superconductivity.

References

[1] Y. Mizuguchi, *et al.*, Phys. Rev. B **86**, 220510 (R) (2012).
[2] T. Yildirim, Phys. Rev. B **87**, 020506 (R) (2013).

Interfacial ferromagnetism in $CaRuO_3$ / $CaMnO_3$

C. He[1], A. J. Grutter[1,2], M. Gu[3], N. D. Browning[3], Y. Takamura[3], B. J. Kirby[4], J. A. Borchers[4], J. W. Kim[5], M. R. Fitzsimmons[5], X. Zhai[1], V. V. Mehta[1,2], F. J. Wong[1], and Y. Suzuki[1,2,6]

There is a wide spectrum of phenomena that occur at the interface between dissimilar materials. In particular, the interface between two distinct but strongly correlated materials can constitute an environment very different from that corresponding to either of the materials alone, leading to emergent properties [1]. Among these is ferromagnetism that emerges at the interface between thin layers of non-ferromagnetic complex oxides. Such emergent ferromagnetism is fascinating from a fundamental perspective, and also holds great potential for applications in electronic devices. Only a few examples of this type of emergent ferromagnetism have been reported, typically dealing with interfaces between two different types of antiferromagnetic insulators [1,2]. Alternatively, ferromagnetism has also been observed for multilayers comprised of a paramagnetic metal $CaRuO_3$ (CRO) and an insulating antiferromagnet $CaMnO_3$ (CMO) [3]. Theory based on the double exchange mechanism predicts that this ferromagnetism arises from just one unit cell (u.c.) of ferromagnetic CMO at each CMO/CRO interface [4]. However, actually determining the origin of ferromagnetism in these materials is problematic using only common laboratory magnetometry instruments, which measure just the total magnetic moment of the entire sample, with no spatial information. Thus, to experimentally test the double exchange model of interfacial ferromagnetism for this system, we have fabricated a series of high quality $[CRO_3 / CMO_N]_{10}$ superlattices (N = 3 to N = 12) on (001) $SrTiO_3$ (STO) substrates, and studied them with several techniques that probe the collective magnetic behavior, and the depth resolved structure and magnetization, including superconducting quantum interference device (SQUID) magnetometry, scanning transmission electron microscopy (TEM), and polarized neutron reflectometry (PNR) [5].

The superlattices of CRO/CMO were grown by pulsed laser deposition with a KrF laser. The atomic abruptness of the interfaces in the superlattices was probed via x-ray reflectivity (XRR) and transmission electron microscopy (TEM). Fig. 1(a) shows a representative XRR scan for a CRO_3 / CMO_{12} superlattice. The low and high frequency oscillations correspond to the superlattice period and the total thickness, respectively. Fig. 1(b) shows an atomic resolution Z-contrast TEM image

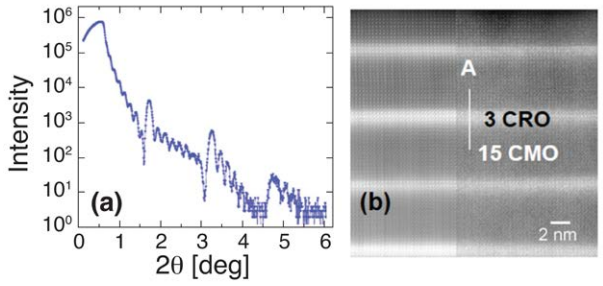

FIGURE 1: (a) X-ray reflectivity scan of CRO_3 / CMO_{12}. **(b)** cross sectional atomic resolution Z-contrast TEM image of CRO_3 / CMO_{15} (the left half of the image is noise reduced using the principle component analysis).

where the CRO layers appear brighter due to the localization of the heavy element Ru. Both XRR and TEM measurements indicate high quality CRO / CMO interfaces with minimal diffusion.

To directly probe the interfacial magnetic profile, we used the NG-1 Reflectometer to perform PNR experiments on an N = 10 superlattice after the sample had been cooled to 5 K in 0.82 T. The neutron beam was polarized alternately up or down with respect to a magnetic field H applied to the sample, and the spin-dependent specular reflectivity was measured as a function of wavevector transfer Q_z. For this scattering geometry, the spin-up and spin-down non-spin-flip reflectivities are functions of the depth profiles $\rho(z)$, the nuclear scattering length density, and $M(z)$, the magnetization component parallel to H. Thus $\rho(z)$ and $M(z)$ were deduced by model fitting the PNR spectra using the Refl1D software package. Fig. 2(a) shows the fitted non-spin-flip PNR data for the N =10 superlattice plotted as Fresnel normalized reflectivity (reflectivity scaled by the theoretical reflectivity of the bare STO substrate). The salient features of the spectra are the low Q_z oscillatory spin splitting, and the spin splitting of the first-order superlattice Bragg peak near $Q_z \approx 1.4$ nm^{-1}. The data are well fit by a model where ferromagnetism is assumed to arise solely from one u.c. of interfacial CMO, as shown in Figs. 2(b) and 2(c). This solution is not unique, as models featuring 2 magnetized u.c. of interfacial CMO, or uniformly magnetized CRO yield qualitatively similar fits to the data. However, we can strictly rule

[1]University of California, Berkeley, CA 94720
[2]Lawrence Berkeley National Laboratory, Berkeley, CA 94720
[3]University of California, Davis, CA 95616
[4]NIST Center for Neutron Research, National Institute of Standards and Technology, Gaithersburg, MD 20899
[5]Los Alamos National Laboratory, Los Alamos, NM 87545
[6]Stanford University, Stanford, CA 94305

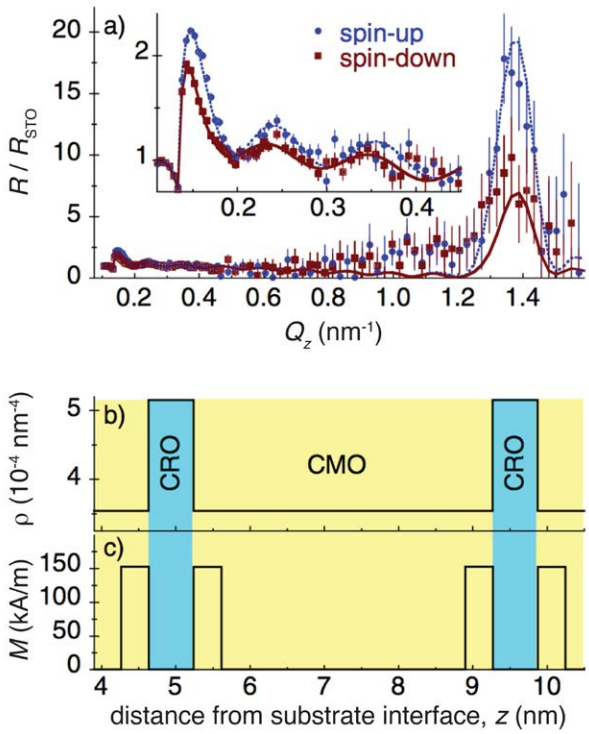

FIGURE 2: (a) PNR spectra for CRO_3 / CMO_{10} measured at 5 K in 0.82 T after field cooling. Inset highlights low Q_Z scattering. Lines are model fits to the data and error bars on the data are one standard deviation. **(b)** Nuclear depth profile. **(c)** Magnetic depth profile corresponding to 1 u.c. interfacial CMO magnetization.

out other competing models, including those featuring magnetic moment that arises from a uniformly magnetized superlattice and uniformly magnetized CMO layers. These models cannot reproduce the spin dependence of the Bragg peak and the spin splitting at low Q_z. Therefore, the PNR data are consistent with magnetic moment arising from 1 u.c. of CMO at the CMO/CRO interfaces, and conclusively confirm a periodic distribution of moment. Similar PNR measurements of an N =11 sample measured using Asterix at the Los Alamos Neutron Science Center gave consistent results.

Having confirmed the interfacial nature of the ferromagnetism, we now consider magnetometry measurements. Fig. 3 shows the hysteresis loops of four representative samples (N = 3, 4, 8, 10) measured at a temperature of 10 K, after cooling in either a positive or negative 5 T magnetic field. For the N = 3 superlattice [Fig. 3(a)], the +5 T and -5 T field cooled loops are basically identical, and are both centered about H = 0. For the N = 4 superlattice [Fig. 3(b)], the positive and negative field cooled loops exhibit small but distinct shifts of -/+ 0.018 T, respectively, and are no longer precisely centered about H = 0. These shifts are indicative of *exchange bias*, a phenomenon most often observed in systems containing ferromagnetic/anitferromagnetic interfaces where uncompensated spins in the antiferromagnetic layer couple to spins in the ferromagnetic layer, biasing them along a particular direction. For superlattices with N = 8 [Fig. 3(c)] and N = 10 [Fig. 3(d)], the exchange bias

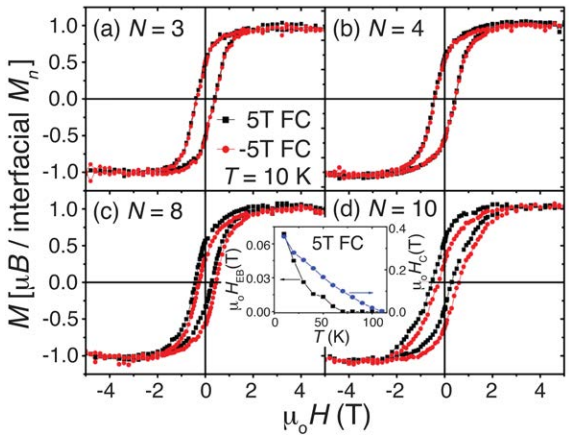

FIGURE 3: Field dependent magnetic moment of (a) N = 3, (b) N = 4, (c) N = 8, and (d) N = 10 CRO_3 / CMO_N superlattices. The measurements were done after +5 T (black squares) and -5 T (red circles) field cooling from 300 K.

field (H_{EB}, the magnitude of the horizontal shift) increases to 0.09 T and 0.12 T, respectively. Our observation of exchange bias implies the presence of a ferromagnetic layer strongly magnetically coupled to an adjacent antiferromagnetic layer. Thus, the onset of exchange bias in the N = 4 superlattice indicates the presence of antiferromagnetic ordering in the 4 CMO layers. If we make a reasonable assumption that at least 2 u.c. of CMO is necessary for antiferromagnetic ordering, that leaves only one u.c. of ferromagnetic CMO at each interface in the N = 4 superlattice to contribute to the ferromagnetism. For the N = 8 and N = 10 superlattices, H_{EB} increases due to the increased pinning force from thicker adjacent antiferromagnetic CMO layers. However, the saturation (*i.e.*, maximum) magnetic moment is similar to that of the N = 4 superlattice, indicating that the number of layers contributing to the ferromagnetism (*i.e.* 1) does not change from N = 4 to N = 10. These results indicate that the interfacial ferromagnetism identified by PNR indeed originates from only 1 u.c. of CMO at each interface.

In summary, we have found ferromagnetism in CRO_3 / CMO_N superlattices on STO (001) substrates, and have demonstrated that it arises from a solitary unit cell of magnetized CMO at each interface. This finding is consistent with density functional theory calculations that attribute the ferromagnetism to double exchange arising from CRO - CMO charge transfer at the interfaces.

References

[1] A. Bhattacharya, S. J. May, S. G. E. te Velthuis, M. Warusawithana, X. Zhai, Bin Jiang, J.-M. Zuo, M. R. Fitzsimmons, S. D. Bader, and J. N. Eckstein, Phys. Rev. Lett. **100**, 257203 (2008).
[2] K. Ueda, H. Tabata, and T. Kawai, Science **280**, 1064 (1998).
[3] K. S. Takahashi, *et al.*, Appl. Phys. Lett. **79**, 1324 (2001).
[4] B. R. K. Nanda, *et al.*, Phys. Rev. Lett. **98**, 216804 (2007).
[5] C. He, A. J. Grutter, M. Gu, N. D. Browning, Y. Takamura, B. J. Kirby, J. A. Borchers, J. W. Kim, M. R. Fitzsimmons, X. Zhai, V. V. Mehta, F. J. Wong, and Y. Suzuki, Phys. Rev. Lett. **109**, 197202 (2012).

Searching for magnetism across the metal-insulator phase transition of a doped J_{eff} = 1/2 Mott insulator

C. Dhital[1], T. Hogan[1], X. Chen[1], Z. Ren[1], M. Pokharel[1], W. Tian[2], Z. Yamani[3], C. Opeil[1], J. S. Helton[4], J. W. Lynn[4], Z. Wang[1], and S. D. Wilson[1]

A new frontier for materials discovery has recently been uncovered within a special class of 5d-electron compounds. These materials incorporate Ir^{4+} ions capable of stabilizing an effective spin one-half electronic ground state (J_{eff} = ½), where quantum fluctuations are maximal [1]. Electrons in this J_{eff} = 1/2 state are subject to a delicate balance between competing on-site Coulomb repulsion, electronic bandwidth, and spin-orbit coupling energy scales [1] whose subsequent interplay gives rise to a range of phenomena from unconventional superconducting states [2], to topologically-protected correlated electronic phases [3], to novel manifestations of Mott physics [4]. In particular, the search has begun for new electronic phases emergent once the insulating J_{eff} = 1/2 parent state in these 5d iridates is destabilized. In this highlight, we detail our recent neutron scattering-based exploration of the magnetic properties in a member of these new J_{eff} = 1/2 Mott insulating materials, $Sr_3Ir_2O_7$ (Sr-327), as it is driven from an insulator into a metal via carrier doping.

$Sr_3Ir_2O_7$ is the bilayer member of the Ruddelsden-Popper iridate series (Fig. 1) and is known to possess a dramatically reduced charge gap, which rests very close to the metal-insulator boundary. Undoped, Sr-327 is a semiconducting two-sublattice antiferromagnet whose moments orient along the c-axis. One way of driving Sr-327 from an insulator into a metal is by gradually replacing Ir^{4+} ($5d^5$) ions with Ru^{4+} ($4d^4$) ions thereby introducing holes into the system and reducing the spin-orbit coupling necessary to stabilize the J_{eff} ground state. Upon replacing ≈ 35 % of Ir^{4+} atoms with Ru^{4+}, charge transport shows that the system becomes a metal [6], but transport measurements cannot reveal the fate of the parent magnetic phase once the system enters the metallic regime.

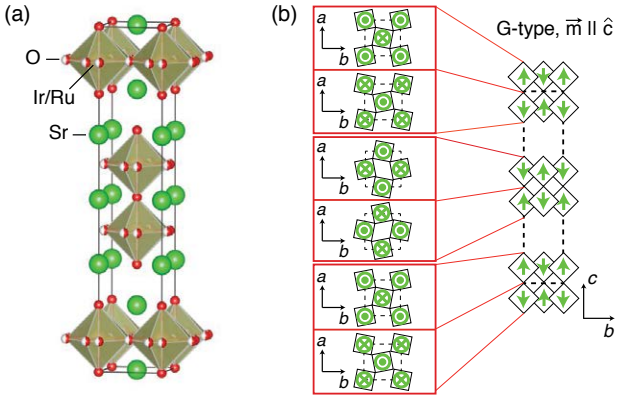

FIGURE 1: (a) Crystal structure of $Sr_3Ir_2O_7$. Each (Ir/Ru) ion is surrounded by an octahedron of oxygen atoms. The fundamental building blocks of the system are IrO_2 planes grouped into bilayers and separated by the A-site Sr atoms. Oxygen octahedra are rotated by ± 10 degrees within the *ab*-plane. **(b)** Magnetic structure of Sr-327 with moments pointing along the c-axis and antiferromagnetically coupled both within the ab-plane and between bilayers.

Our recent neutron scattering work studying the evolution of magnetic order in this Ru-doped Sr-327 system has uncovered that, contrary to the picture painted by bulk magnetization and charge transport, an unexpected long-range itinerant, antiferromagnetic order survives deep into the metallic phase (Fig. 2) [6]. The persistence of magnetic order across the metal-insulator transition (MIT) calls into doubt competing theories that model this system as a magnetic band insulator. Instead, the mechanism for charge gap formation is likely tied to the proposed J_{eff} = 1/2 Mott mechanism along with a high temperature structural distortion we recently discovered.

[1]Boston College, Chestnut Hill, MA 02467
[2]Oak Ridge National Laboratory, Oak Ridge, TN 37831
[3]Chalk River Laboratories, Chalk River, Ontario K0J 1P0, Canada
[4]NIST Center for Neutron Research, National Institute of Standards and Technology, Gaithersburg, MD 20899

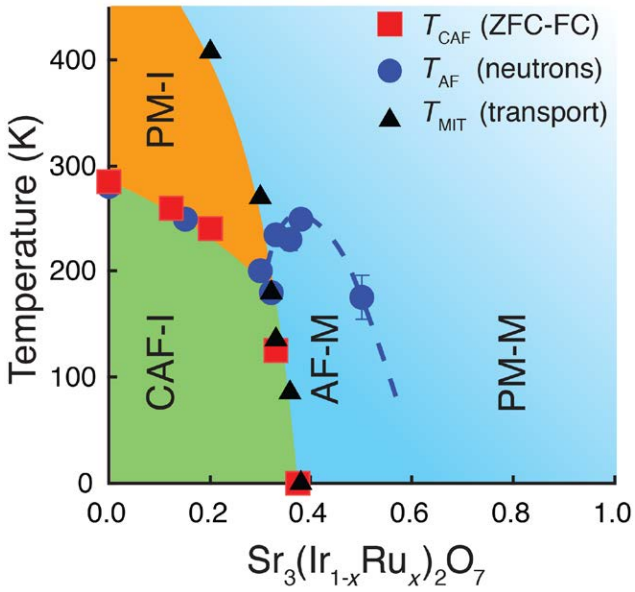

FIGURE 2: Electronic phase diagram of $Sr_3(Ir_{1-x}Ru_x)_2O_7$. Symbols denote the boundaries between canted antiferromagnetic-insulating (CAF-I), antiferromagnetic-metallic (AF-M), paramagnetic-insulating (PM-I), and paramagnetic-metallic (PM-M) phases. Triangles and squares denote the results of bulk transport and magnetization measurements, respectively, while circles show neutron scattering results determining the onset temperatures of long-range antiferromagnetic order.

In using the combined power of a position-sensitive detector and ^{3}He-neutron polarization, we were also able to unambiguously separate magnetic and nonmagnetic scattering arising at the same scattering angles in the *undoped* Sr-327 compound and to identify structural superlattice peaks (Fig. 3) that violate the nominal *Bbcb* space group of this system [5]. This high temperature structural distortion is suggestive of a tilting of the oxygen octahedra into the *ab*-plane, and it raises questions regarding the distortion's role in the charge gap formation of this class of materials. Future studies on *doped* samples on BT-7 will continue to explore the relationship between this distortion and the electronic ground state of this system.

Through combined unpolarized and polarized neutron scattering investigations of the properties of the hole-doped J_{eff} = 1/2 system $Sr_3(Ir_{1-x}Ru_x)_2O_7$, we were able to show that antiferromagnetism survives into the metallic regime once the J_{eff} = 1/2 Mott phase is

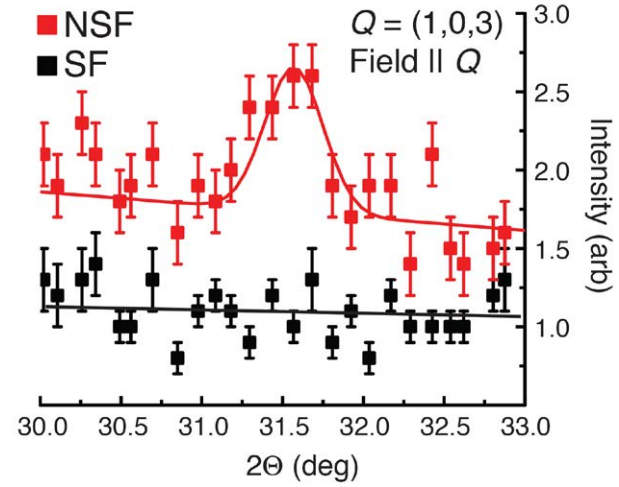

FIGURE 3: Spin-flip (SF) and non-spin-flip (NSF) polarized neutron scattering data collected on the BT-7 triple-axis spectrometer. Data were collected at 300 K with the magnetic guide field oriented parallel to the scattering wave vector. The Bragg peak appears only in the non-spin-flip channel, demonstrating the structural origin of the superlattice and the violation of the *Bbcb* space group. Uncertaintes on the data are one standard deviation.

quenched. This emergent, itinerant magnetic phase arises from the delicate interplay between Ru^{4+} S = 1 ions and the residual correlations of the J_{eff}= 1/2 Mott phase, and presents a new system for probing the magnetic interactions inherent to this 5d Mott phase. We also uncovered a surprising high temperature structural distortion in the undoped parent material $Sr_3Ir_2O_7$ that may be related to the mechanism responsible for the insulating phase. Together, our neutron results uncover a complex picture of both magnetic and structural phase behavior within a doped J_{eff} = 1/2 insulator and suggest that electron-electron correlation effects play an essential role in governing the phase behavior in this class of 5d-electron materials.

References

[1] B. J. Kim, H. Ohsumi, T. Komesu, S. Sakai, T. Morita, H. Takagi, T. Arima, Science **323**, 1329 (2009).

[2] F. Wang, T. Senthil, Phys. Rev. Lett. **106**, 136402 (2011).

[3] D. Pesin, L. Balents, Nature Physics **6**, 376 (2010).

[4] B. J. Kim, H. Jin, S. J. Moon, J.-Y. Kim, B.-G. Park, C. S. Leem, Jaejun Yu, T.W. Noh, C. Kim, S.-J. Oh, J.-H. Park, V. Durairaj, G. Cao, E. Rotenberg, Phys. Rev. Lett. **101**, 076402 (2008).

[5] H. Matsuhata, I. Nagaia, Y. Yoshida, S. Hara, S. Ikeda, N. Shirakawa, J. Solid State Chem. **177**, 3776 (2004).

[6] C. Dhital, T. Hogan, X. Chen, Z. Ren, M. Pokharel, W. Tian, Z. Yamani, C. Opeil, J. S. Helton, J. W. Lynn, Z. Wang, S. D. Wilson, Phys. Rev. Lett. (in review).

Frozen spin ice correlations in the ground state of the pyrochlore magnet $Tb_2Ti_2O_7$

K. Fritsch[1], E. Kermarrec[1], K. A. Ross[1,2,3], Y. Qiu[3], J. R. D. Copley[3], H. A. Dabkowska[4], and B. D. Gaulin[1,4,5]

Geometrically-frustrated magnetism has been fertile ground for exotic magnetic ground states in new magnetic materials, leading to spin glass, spin liquid and spin ice states at low temperatures, in contrast to conventional long range order found in most magnetic materials. Such materials are often comprised of magnetic moments decorating a network of interconnected triangles and tetrahedra, and the pair-wise interactions between the magnetic moments are incompatible with a simple ordered state on this network. Cubic pyrochlore titanate magnets, with the chemical composition of $A_2Ti_2O_7$, where the A site is occupied by a magnetic rare earth ion, can be described in these terms. This family of materials has been widely explored by scientists interested in geometrical frustration, as many such magnets exist with varying properties, and they can be grown as large single crystals.

$Tb_2Ti_2O_7$ (TTO) is one such cubic pyrochlore antiferromagnet, with magnetic Tb^{3+} ions decorating a network of corner-sharing tetrahedra. Remarkably, even though its exotic ground state has been debated for almost 15 years, it has very recently been the topic of significant experimental research interest [1-3]. Our theoretical understanding of the interactions in TTO, based on classical Ising-like Tb^{3+} spins [4], originally suggested a magnetically ordered state below ≈ 1 K. However, early muon spin resonance and neutron scattering experiments on this material showed no evidence for long range order down to 50 mK [5]. Over time, this motivated two theoretical scenarios to account for the apparently disordered ground state in TTO: a quantum spin ice scenario [6] and a non-magnetic singlet ground state [7].

Our recent neutron scattering measurements [2] on a single crystal of TTO, using the DCS beam line with a dilution refrigerator and 10 T magnet, reveal short range, static spin correlations developing below $T \approx 275$ mK with a (½,½,½) ordering wave vector (Fig. 1a), and a concomitant opening of a spin gap across most of the Brillouin zone (Fig. 2). The diffuse elastic scattering observed at (½,½,½) positions in reciprocal space and its corresponding real space spin arrangement can be modeled as a short range antiferromagnetically ordered spin ice (Fig. 1b), in which spins obey a variant of the 2-in 2-out ice rules in each unit cell, and flip directions between adjacent cells (Fig. 1c, d). Spin ice itself is a six-fold degenerate arrangement of spins on a single tetrahedron. It leads to a macroscopically-degenerate disordered state which supports emergent electrodynamics, with diffusing magnetic monopoles as its elementary excitations [8].

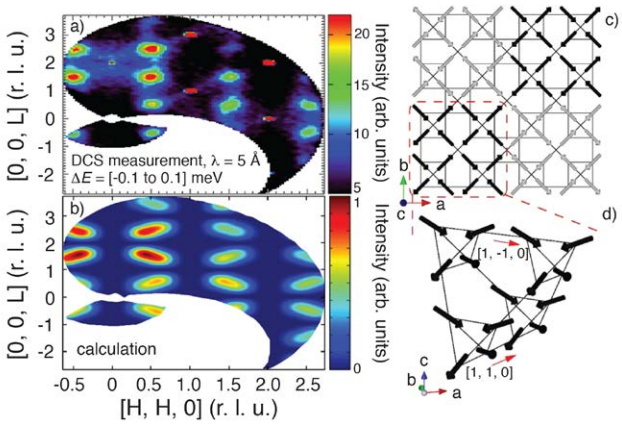

FIGURE 1: Comparison of the measured elastic diffuse scattering in the (H,H,L) plane of $Tb_2Ti_2O_7$ at 70 mK and $H = 0$ T (panel a) to the calculated $S(Q)$ (panel b). The spin arrangement between neighboring conventional unit cells is shown as a projection onto the xy-plane in panel c). The ordered 2-in 2-out spin configuration in a single unit cell is shown in panel d), and this pattern is reversed in the neighboring cells (black vs. grey arrows in panel c) to form "(½,½,½) ordered spin ice". The spins are tilted from their local [1,1,1] axes by 12 degrees.

Recently, ac susceptibility measurements at very low temperature and under a magnetic field applied along [1,1,1] were performed by Yin *et al.*[9]. They uncover a new *H-T* phase diagram, with the existence of a crossover at $T \approx 0$ and $\mu_0 H \approx 0.07$ T between two quantum phases. We used inelastic neutron scattering to follow the evolution of the spin dynamics under magnetic fields as a related phase boundary is crossed (one pertaining to the application of a [1,-1,0] magnetic field, Fig. 3). For low fields and temperatures,

[1] Department of Physics and Astronomy, McMaster University, Hamilton, ON, L8S 4M1, Canada
[2] Institute for Quantum Matter and Department of Physics and Astronomy, Johns Hopkins University, Baltimore, MD 21218
[3] NIST Center for Neutron Research, National Institute of Standards and Technology, Gaithersburg, MD 20899
[4] Brockhouse Institute for Materials Research, McMaster University, Hamilton, ON, L8S 4M1, Canada
[5] Canadian Institute for Advanced Research, Toronto, ON, M5G 1Z8 Canada

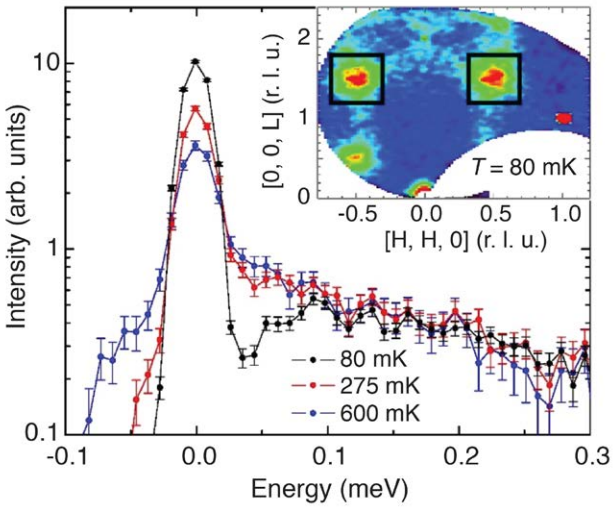

FIGURE 2: High-resolution neutron scattering data of $Tb_2Ti_2O_7$ in zero field. Intensity vs. energy transfer of the (½,½,½) positions averaged over two peaks as a function of temperature. Note the logarithmic intensity scale. The *Q*-integration range (H = [+/-0.3 to +/-0.7], L = [1.2 to 1.8] r.l.u.) is shown in the inset by the two black squares. Error bars represent one standard deviation.

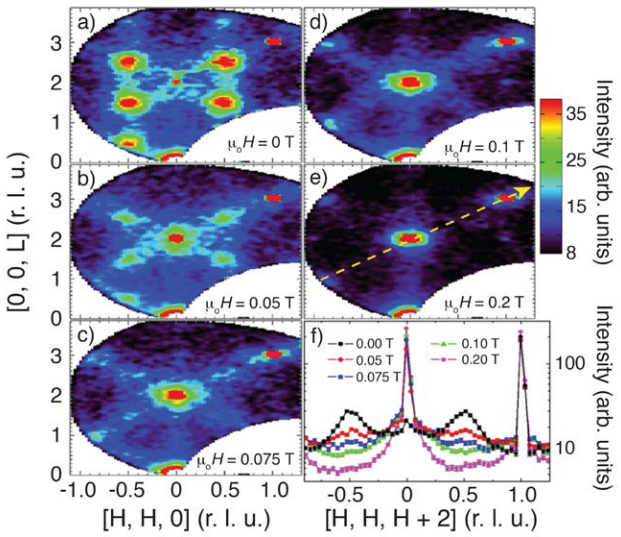

FIGURE 3: Elastic neutron scattering data within the (H,H,L) plane of $Tb_2Ti_2O_7$ at $T = 80$ mK for different values of applied magnetic field ($H \parallel [1,-1,0]$). The energy is integrated from $-0.1 < E$ (meV) < 0.1. Panels a) through e) show the evolution of the elastic scattering for an applied magnetic field of 0 T, 0.05 T, 0.075 T, 0.1 T and 0.2 T, respectively. Panel f) shows the *Q*-dependence of the elastic scattering along the [1,1,1] direction cutting through the (0,0,2) Bragg position as indicated by the yellow arrow in panel e). The (½,½,½) peaks vanish around $\mu_0 H \approx 0.075$ T (panel c)).

the susceptibility of TTO is isotropic, and little directional dependence of the field is expected. As the magnetic field is increased, the diffuse scattering at the (½,½,½) positions gets suppressed substantially, while there is a strong build-up in intensity at the structurally forbidden 002 peak. The application of a small magnetic field of 0.075 T along [1, -1, 0] is found to destroy the antiferromagnetic short range ordered spin ice state previously evidenced in zero field (Fig. 3c), in agreement with the susceptibility data of Yin *et al.* A further feature in the elastic scattering maps are weak rods of scattering along the [0,0,L] and [1,1,1] directions that have been identified as evidence for significant anisotropic exchange in TTO, consistent with observations in other pyrochlore titanates such as $Yb_2Ti_2O_7$ [10] or $Er_2Ti_2O_7$ [11].

This set of recent neutron scattering measurements focused on the identification of the ground-state of TTO in zero and moderate magnetic fields. It notably supports the quantum spin ice picture to explain its low temperature properties - a frozen variant of spin ice is clearly observed at low temperatures. Diffuse scattering near the quantum critical point will place an important constraint on any theory wishing to describe this transition. The origin of the short range frozen state itself remains mysterious. Whether the presence of weak disorder, perhaps in the form of extra magnetic Tb^{3+} ions as suggested by Taniguchi *et al.* [3], is responsible for the ordering, or on the contrary is preventing the correlation length from diverging, is one of the key questions to address in the future.

References

[1] for example: S. Petit *et al.*, Phys. Rev. B **86**, 174403 (2012), T. Fennell *et al.*, Phys. Rev. Lett. **109**, 017201 (2012).
[2] K. Fritsch *et al.*, Phys. Rev. B **87**, 094410 (2013).
[3] T. Taniguchi *et al.*, Phys. Rev. B **87**, 060408(R) (2013).
[4] M. J. P. Gingras *et al.*, Phys. Rev. B **62**, 6496 (2000).
[5] J. S. Gardner *et al.*, Phys. Rev. Lett. **82**, 1012 (1999); J. S. Gardner *et al.*, Phys. Rev. B **68**, 180401 (2003).
[6] H. R. Molavian *et al.*, Phys. Rev. Lett. **98**, 157204 (2007); H. R. Molavian *et al.*, arXiv:0912.2957v1 (2009).
[7] P. Bonville *et al.*, Phys. Rev. B **84**, 184409 (2011).
[8] C. Castelnovo *et al.*, Annu. Rev. Condens. Matter Phys. **3**, 35 (2012).
[9] L. Yin *et al.*, Phys. Rev. Lett. **110**, 137201 (2013).
[10] K. A. Ross *et al.*, Phys. Rev. X **1**, 021002 (2011).
[11] L. Savary *et al.*, Phys. Rev. Lett. **109**, 167201 (2012).

Stresses in a test artifact produced by additive manufacturing

T. Gnäupel-Herold[1], J. Slotwinski[2], and S. Moylan[2]

Additive Manufacturing (AM) is a term to describe processes for fabricating parts layer-by-layer directly from a digital 3D model. AM is a technology at the beginning of its arc, and many parameters affecting performance-relevant mechanical properties have yet to be explored. In this work, we analyze the residual stresses in a test artifact made of a high-strength stainless steel with respect to effects of size, dimensions and aspect ratios of the structures in the artifact. In order to allow further processing of the undisturbed AM-specimen, neutron diffraction was used to evaluate non-destructively the three-dimensional distribution of stress fields.

AM has excellent prospects for producing high-value parts that are individually customized and complex in shape due to the lack of topological constraints. For example, there is no principal obstacle for producing a seamless, hollow sphere, and in a time comparable to conventional milling methods that still require joining of separately made parts. The capabilities of AM are extraordinary but the technology faces a number of challenges on its way to broader dissemination, including a lack of data and standards for mechanical properties. One of the central questions surrounding the process is the fidelity between the digital model and part metrics. This is also where residual stresses play a decisive role in the sense that stresses can and do create substantial distortions and deviations from the intended shape that can render the AM-produced part useless (Fig. 1).

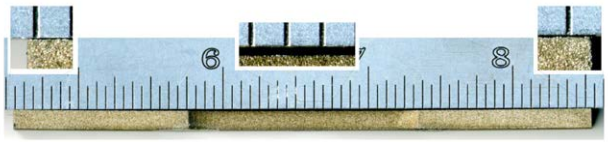

FIGURE 1: Self-bending of a cobalt-chromium AM-sample as demonstrated by a 0.2 mm gap between ruler (top) and sample.

This is of particular importance for metal-based AM-built parts for use in applications such as automotive engines, aircraft assemblies and medical implants where the desired functionality dictates complex shapes and high strength, with the latter almost invariably implying high residual stresses. The implication of high residual stresses is rooted in the powder bed fusion (PBF) process most commonly used in metal-based additive manufacturing. The process is shown schematically in Fig. 2.

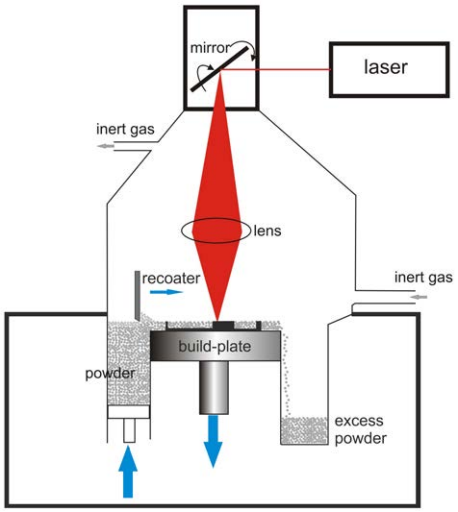

FIGURE 2: Schematic of the powder bed fusion process. A point heat source provided by a 400 W Yb-fiber laser sinters a region of a powder bed. A layer is built by moving the point (100 µm to 500 µm diameter) according to the digital model using an optical deflection (mirror) and focusing system (f-θ lens). After completion of the layer, a recoater spreads a new powder layer (≈ 0.02 mm) over the built structure that is then lowered by that thickness to keep the focal range constant. The process is repeated.

The layer-by-layer "build" occurs through moving ("scanning") the laser focus within the build-plane whereby neighboring scan lines fuse together by a slight overlap of the laser focus. By thermally quenching small, hot zones where sintering of particles occurs (≈ 1700 K) on top of a structure that is at a much lower temperature (< 400 K) quenching strains arise that are only partially permanent (plastic), with a small fraction of elastic strains that give rise to residual stresses. However, this represents only a qualitative understanding, with the actual three-dimensional distribution of residual stresses depending on structure geometry and on machine-dependent parameters such as scan speed, focal diameter and laser power.

The AM machine was operated in a preset that distinguished between the so called "skin" mode and "core" mode. The skin mode featured a smaller laser focus diameter and closer scan lines within a range of ≈ 0.7 mm from any one of the six surfaces of the parallelepiped structures including the bottom surface fused to the build-plate (Fig. 3). This "skin" zone receives a higher input of thermal energy with the goal of reducing

[1]NIST Center for Neutron Research, National Institute of Standards and Technology, Gaithersburg MD 20899
[2]Intelligent Systems Division, Engineering Laboratory, National Institute of Standards and Technology, Gaithersburg MD 20899

porosity and increasing strength. As a consequence, structures with different aspect ratios and dimensions several times that of the "skin" thickness will exhibit different stress fields, depending on the relative volumes of "core" and "skin". In order to assess the influence of geometry and size on residual stresses several structures fused to a build-plate were investigated, and two different types of fusing the structures to the build plate were considered. The inset in Fig. 3, top right, shows one bottom surface (after cutting) with a support structure (blue dot) consisting of 0.1 mm thick walls arranged in a 1 mm by 1 mm pattern with 1 mm height. All structures but one (blue dot) on the actual sample were built with such a support structure. The purpose of the support structure is to allow easier removal after the build, and to reduce residual stresses through thermally insulating the structure from the build-plate during the build.

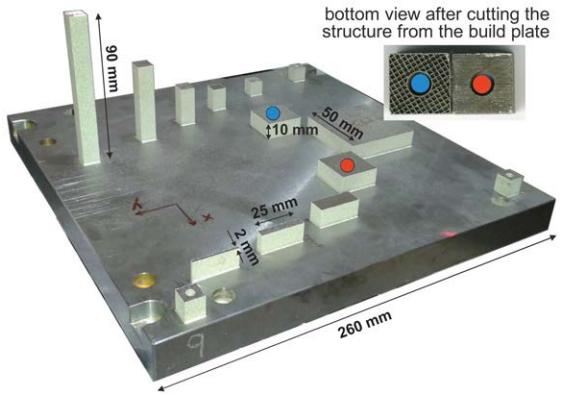

FIGURE 3: Test artifact used in the neutron diffraction stress measurements. Blue indicates a build that is fused directly to the build-plate (no support structure – red circle).

As shown in Fig. 4, this expectation of stress reduction is justified but the effect decreases as the distance to the build-plate increases (vertical scan). More notably, the stresses on the surface reach about 450 MPa – nearly 50 % of the bulk yield strength – which is high enough to raise concerns about fatigue performance.

A more detailed three dimensional analysis of the residual stresses is shown in Fig. 5. Three structures with very different aspect ratios of thickness to height ranging from 2:10 and 5:10 were investigated with respect to stresses normal to the build-plate. The "blade" (2:10) is dominated by the "skin" mode and it has the least variation in terms of stress. Similar near-surface stresses are found in the structure with higher thickness (5:10). However, this structure also has a distinct "core" mode region, and higher stress gradients are present as indicated by the high compressive stresses in the interior (2.5 mm from surface). In other words, within a distance of approximately 2 mm the stresses transition from ≈ +200 MPa near-surface tensile stresses ("skin") to ≈ -200 MPa compressive stress ("core") or more. Another notable feature of the residual stresses is that structural symmetry does not necessarily imply stress symmetry.

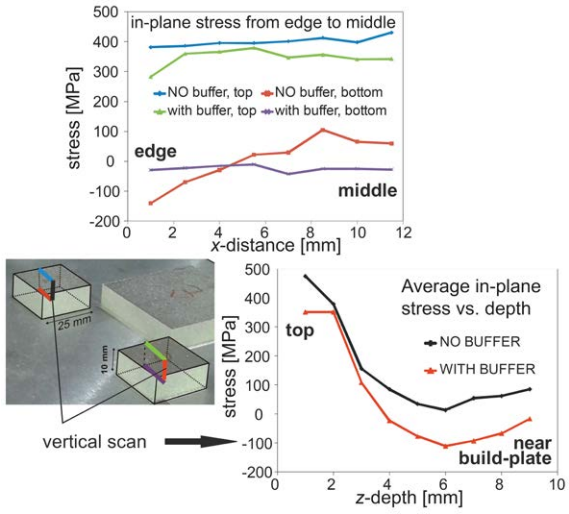

FIGURE 4: Residual stresses in "builds" with and without support structures (buffer). The color codes in the inset picture are the same as in the graphs.

In this ongoing project, many of the data generated are first-in-kind, and particularly the correlations between many process parameters (skin/core mode) and part properties such as stresses are not yet known. The stresses found here are unfavorable from a mechanical point of view because near surface tensile stresses promote cracking. A post-build treatment such as shot-peening is generally necessary to improve upon these properties, and it is intended to study the changes in stresses after shot-peening.

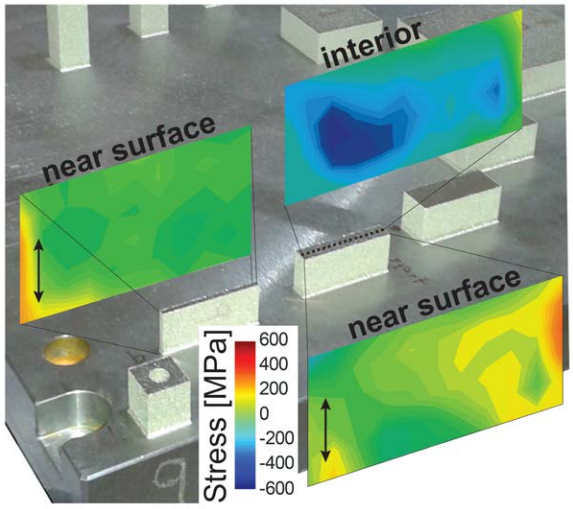

FIGURE 5: Stress maps (9x9 resolution) at various depths from the front surface. The arrows indicate the direction of the stress.

TOF measurements at neutron guide NG-Bu to characterize the source spectrum

J. C. Cook[1], J. Barker[1], C. Gagnon[1,2], R. Ibberson[1,2], R. Lindstrom[1], D. A. Neumann[1], J. M Rowe[1], and R. E. Williams[1]

The cold neutron source of the NBSR research reactor at the NCNR produces a spectrum of especially slow-moving neutrons. These low-energy neutrons have particularly desirable properties for probing matter at the atomic level. Just as atoms in a gas slow down when cooled, so do neutrons when they interact with a cold material, giving up some of their energy to the material. The slowing-down material, which must exhibit good neutron scattering properties with low neutron absorption, is referred to as a moderator. In general, the lower the temperature of the moderator, the lower is the average energy of the neutrons that emerge. In the case of the NBSR, the cold source moderator is liquefied hydrogen (LH_2) at atmospheric pressure at a temperature of about -253 °C, or 20 K. Knowing the cold neutron spectrum is a major asset to instrument development, and understanding or being able to confidently and reliably predict the spectrum is paramount for cold neutron source development. However, this seemingly fundamental quantity is surprisingly elusive. Unfortunately, direct measurement of the cold source spectrum by inserting a suitable probe in proximity of the functioning cold source is not feasible. An alternative is to measure the spectrum at the end of a cold neutron guide and correct for the transmission function of the guide. The neutron guide itself is a highly polished glass tube with special reflective interior coatings, used to concentrate the neutrons into beams and conduct them efficiently far from the source. As such, the neutron guide can alter the transmitted neutron spectrum in a complex way meaning that the guide transmission function must be simulated.

The temporary vacancy at the end of the newly-installed neutron guide NG-Bu, prior to installation of a SANS instrument, provided a rare opportunity to perform this measurement using the neutron time-of-flight (TOF) technique, Fig. 1. The particular properties of the NG-Bu guide, together with careful design of the measurement apparatus, allowed us to significantly improve upon a previous measurement from the mid-1990s. The aforementioned measurement was performed on an unfiltered straight guide (NG-1) with the first generation (Unit 1) liquid hydrogen cold source, but was subject to appreciable uncertainty. The situation was not improved by the fact that the second generation (Unit 2) cold source spectrum (previously unmeasured) had to be inferred from the Unit 1 measurement, via measured Unit 2/Unit 1 gain curves, introducing another layer of uncertainty.

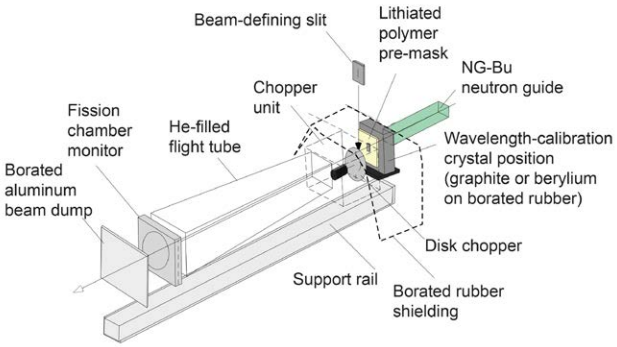

FIGURE 1: A schematic layout of the TOF apparatus.

In addition to providing an accurate basis for instrument simulations, this measurement was motivated by the desire to understand more fully the physics of the liquid hydrogen cold source when the reactor is operating at full power. Even though the cold source at the NBSR operates at atmospheric pressure, the liquid hydrogen at 20 K is not a straightforward cryogen by virtue of the spin of the protons in the hydrogen molecule. In a low-radiation environment, freshly liquefied hydrogen (such as we have prior to most beginning-of-cycle reactor startups) consists of a 75 % mole fraction of molecules in which both proton spins are parallel (ortho) and 25 % mole fraction of para (spins antiparallel). This ratio reflects the statistical occupancy of angular momentum states in "normal hydrogen" – an example of which is room-temperature hydrogen. Once liquefied, the hydrogen converts slowly towards the para ground state – a process that may be catalyzed – although 100 % mole fraction para is rarely achieved. However, in a high-radiation environment a different, but hard to quantify, ortho-para equilibrium is established. When trying to model the cold source spectrum this presents a problem because the scattering properties of ortho and para hydrogen are quite different in the energy

[1]NIST Center for Neutron Research, National Institute of Standards and Technology, Gaithersburg, MD 20899
[2]University of Maryland, College Park, MD 20742

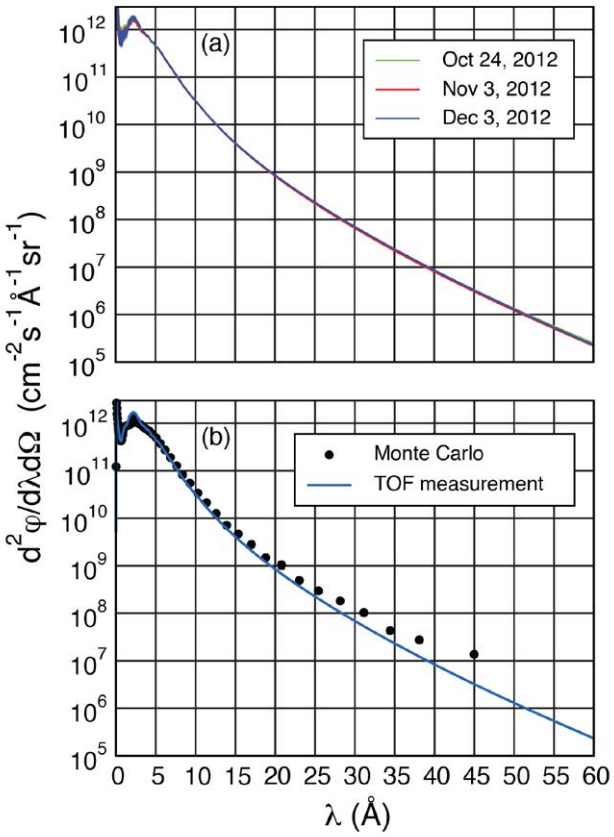

FIGURE 2: (a) Estimated Unit 2 LH_2 cold source brightness resulting from three independent TOF measurements. For each measurement, 20 superimposed curves are shown, corresponding to 20 independent simulations of the neutron guide transmission. For each simulation a unique guide configuration was generated by randomly selecting the reflectivity, substrate waviness, and element misalignments within their estimated distributions. The distribution of the curves is therefore characteristic of the spread in results due to the simulation step of the brightness evaluation. **(b)** An MCNP simulation assuming a 65:35 ortho:para ratio using LANL scattering kernels (black circles) is compared against the mean brightness function from the curves in (a).

region of interest. Specifically, the scattering cross-section of para hydrogen is much lower than that of ortho hydrogen for neutron energies below about 15 meV (wavelengths greater than about 2.3 Å). Thus, a simulation of the cold source assuming an incorrect ortho:para ratio results in an incorrect spectrum. Furthermore, there are some disagreements between sources of ortho and para hydrogen scattering data used in transport codes, which leads to further uncertainty.

The neutron wavelength calibration was performed by measuring Bragg edges from a polycrystalline beryllium crystal and a polycrystalline graphite crystal. The absolute intensity normalization was provided by a gold foil activation measurement of the thermal-equivalent fluence rate. The three TOF measurements, each at different stages of a reactor cycle, yielded evidence that the spectrum below about 3 Å might change slightly during the cycle, but the cold neutron spectra revealed few differences. Fig. 2(a) shows the results of the three independent measurements (at 20 MW). The "fuzziness" on the three sets of curves indicates a credible distribution of results, obtained by running multiple simulations of the NG-Bu guide with supermirror reflectivities, substrate waviness, and element misalignments adjusted randomly within their analyzed distributions. The blue curve in Fig. 2(b) represents the mean of these curves, which is henceforth adopted as the standard for future simulations. The shortest wavelength part of this model (which is relatively insensitive to variations in the ortho:para hydrogen ratio) is appended from an MCNP [1] simulation of the cold source cavity brightness, assuming a 65:35 ortho:para mole ratio, with (calculated) scattering kernels originating from Los Alamos National Laboratory. This MCNP simulation, extended into the cold neutron region, is indicated by the circular black symbols for comparison with the measurements.

In total, three independent measurements were performed, including an attempt to witness spectral changes due to the increase of ortho content during the initial reactor power ramp and hold at 20 MW. The latter required extraordinary coordination with various teams. The hydrogen was liquefied many days prior to startup (to maximize the initial para concentration) and measurements were taken quickly as power was increased. In the end, measurements yielded little evidence of a significant change in the neutron spectrum suggesting that either equilibrium is established within minutes of startup or that the initial para concentration is lower than expected.

In conclusion, we have performed the most accurate measurement-based estimate of the NBSR Unit 2 liquid hydrogen cold source brightness to date. The data quality was sufficient to yield reliable source brightness estimates extending to neutron wavelengths exceeding 60 Å (neutron speeds below 65 m/s). A comparison of the measurement with simulations using the particle transport code MCNP and hydrogen scattering data originating from ENDF/B-VII (endf70a and endf70sab libraries) is consistent with a steady-state hydrogen distribution of (50 to 75) % mole fraction in the ortho state. These measurements eliminate uncertainties from previous measurements of the cold source brightness and will allow for improved design choices in future cold source development. More details of these measurements will appear in a forthcoming publication.

References

[1] MCNP–A General Monte Carlo N-Particle Transport Code, Version 5, X-5 Monte Carlo Team, Diagnostics Applications Group, Los Alamos National Laboratory.

Nano-pore condensation of methane in shales

A. P. R. Eberle[1], H. E. King[1], G. Rother[2], D. J. Wesolowski[2], C. C. Walters[1], and C. E. Kliewer[1]

GEOLOGY

In the last decade, natural gas produced from shales has grown to become a major factor in the U.S. energy supply. This boom is largely the result of improved extraction methods and a better understanding of the porous nature of mature organic matter. The production rates of wells within the same geologic formation can vary significantly. Opportunities to optimize well number and placement and completion practices require a fuller understanding of the physics of gas encapsulation and flow in shale.

Shales are sedimentary rocks consisting of both organic and inorganic matter. While it is well established that the productivity of shale is a function of both gas storage and transport, the pore architecture in most high-maturity organic-rich shales is poorly understood. For instance, sorption measurements and microscopy suggest the majority of the porosity resides within organic matter [1,2]. This is in contrast to coarser grained sedimentary rocks where the pores form within a mostly inorganic framework and the pore-rock fabric interface is well described as a continuum of pore sizes spanning a range from mm to nm, following an approximately power-law size distribution [3].

Small-angle neutron scattering (SANS) offers unique advantages over other scattering techniques such as light and x-ray in the measurements reported herein as i) neutrons are highly penetrating, ii) neutrons interact with the atomic nucleus and lend to isotope labeling, and iii) the neutron scattering length density of the inorganic components of the matrix are similar, and as a result, the majority of the scattering comes from the pores. We use SANS to study the pore selectivity to light hydrocarbon condensation. We report on experimental measurements of shale samples under vacuum and pressurized with both deuterium and methane [4]. At pressures up to 34.5 MPa we find that methane condenses into nano-sized pores located within the organic phase of the matrix.

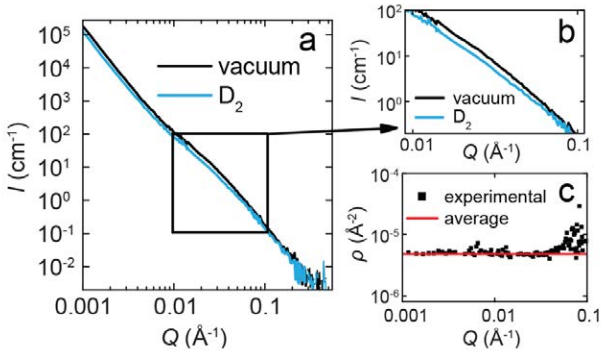

FIGURE 1: a) SANS scattering intensity from a shale sample in both vacuum and at 34.5 MPa of deuterium (D_2). b) Expanded SANS from the region outlined by the box in (a). c) Average scattering length density of the matrix calculated from Eq. (1).

Shale slabs were cut parallel to the bedding plane with thickness < 0.4 mm to minimize multiple scattering. SANS measurements were performed using the NIST high pressure de-mountable cells under vacuum and pressurized with various gases. Fig. 1 (a) displays the scattering intensity, representative of all samples measured, in vacuum and at 34.5 MPa with D_2. Deuterium, thermodynamically similar to hydrogen, has a relatively small kinetic diameter, d = 0.289 nm, and can be treated as an ideal gas over a wide range in temperature and pressure. We assume all the pores within the length scales measured with SANS (>≈ 1 nm) are accessible to the gas molecules. The scattering at the two conditions is similar but the total intensity decreases for the case of deuterium, see Fig. 1 (b) an expansion of the box in Fig. 1 (a). This is expected as the major component to the scattering intensity arises from the contrast between the matrix and the pores, $I(Q) \sim (\rho_{matrix} - \rho_{pore})^2$, where ρ is the scattering length density, and Q is the momentum transfer. The matrix $\rho_{matrix} \approx 4 \times 10^{-6}$ Å^{-2}, and for vacuum and with deuterium, respectively, $\rho_{pore} \approx 0$ Å^{-2} and $\rho_{pore} \approx 8.55 \times 10^{-6}$ Å^{-2} , assuming gas density in the pore is equal to the bulk density calculated from the NIST Reference Fluid Thermodynamic and Transport Properties Database (REFPROP). To a first order approximation the pores can be represented by particulate scattering methods from a two-

[1]ExxonMobil Research and Engineering Company, Annandale, NJ 08801
[2]Oak Ridge National Laboratory, Oak Ridge, TN 37831

phase system, in which case the average scattering length density of the matrix can be calculated from the following ratio, where ρ_{vac}, ρ_{D_2}, and ρ_m are the scattering length

$$ratio = \frac{I_1(Q)}{I_2(Q)} = \frac{(\rho_{vac} - \rho_m)^2 S_f}{(\rho_{D_2} - \rho_m)^2 S_f} \quad (1)$$

densities of the pore under vacuum, pore at pressure with D_2 and the matrix, respectively, and S_f is the scattering function for the system. Fig. 1 (c) is a plot of the ρ_m vs. Q calculated using Eq. (1), and we obtain an average $\rho_m = 4.8 \times 10^{-6}$ Å^{-2}. This value agrees well with the estimated scattering length density of the inorganic matrix (matrix composition determined from x-ray diffraction measurements, data not shown) and is roughly twice the estimated value of the scattering length density of the pure organic material, $\rho_{organic} \approx 2.0 \times 10^{-6}$ Å^{-2}.

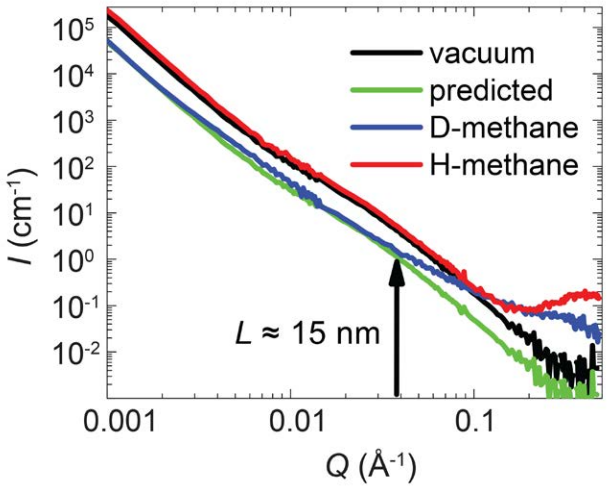

FIGURE 2: SANS scattering intensity from a shale sample in both vacuum and at 34.5 MPa of methane (CD_4 and CH_4). The predicted scattering curve of CD_4 determined using Eq. (1) with the bulk scattering length density of methane and the average scattering length density of the matrix.

Fig. 2 displays the predicted SANS scattering intensity using Eq. (1) and assuming bulk density of the deuterated methane within the pores, along with the experimental scattering from both CD_4 and CH_4 at 34.5 MPa. For length scales ($L \approx 2\pi/Q$) $L >\approx 15$ nm, the predicted scattering is nearly identical to the experimental data but diverges at higher Q. This suggests a significant change in the scattering contrast, $\Delta\rho$, as result of capillary condensation of the gas within the nano-pores, i.e. $\rho_{gas} \approx 2.93 \times 10^{-6}$ Å^{-2}, $\rho_{liquid} \approx 5.29 \times 10^{-6}$ Å^{-2} (in the case of CD_4). More detail can be extracted by considering the relative magnitude of the intensities at high Q, $I_{CH_4} > I_{CH_4} > I_{vacuum}$. Within the assumption that $I(Q) \sim (\rho_{matrix} - \rho_{pore})^2$, and recognizing that ρ_{CD_4} and ρ_{CH_4} are quite distinct allows us to conclude that the major scattering contribution must arise from the fact that methane is selectively condensed within the organic phase. These results confirm without question that there is porosity within both the inorganic and organic phases of shales and the methane condenses within the nano-pores of the organic phase. However, we cannot rule out that the methane also condenses in nano-pores found in the inorganic phase.

A summary of our findings is depicted in Fig. 3. Shales consist of both an inorganic and organic phase. On large length scales O(cm) the compositional distribution is homogeneous but locally the two phases are separate. Pores exist in both phases but there are a disproportionate number of small pores O(nm) in the organic phase. We have confirmed the existence of the small pores through direct imaging using Helium Ion microscopy, an example can be seen as an inset to Fig. 3. When pressurized with methane, capillary condensation occurs in the small pores located within the organic phase. These results shed light on the phase behavior and interaction of light hydrocarbons in shales and have implications in quantifying total hydrocarbon capacity in shales, as well as the development of improved extraction methods.

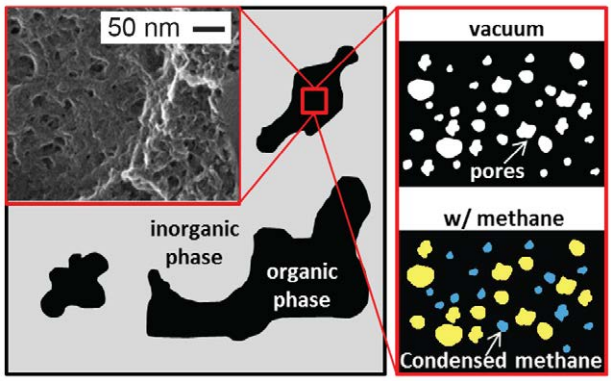

FIGURE 3: Schematic of inorganic and organic phases in shale. The box indicates a magnification of the organic phase: (left) helium-ion image of nano-pores in the organic phase, (right) schematic of nano-pores under two conditions as inferred from SANS measurements: (right, top) vacuum, and (right, bottom) pressurized with methane. Blue and yellow represent liquid and gas phases, respectively.

References

[1] P. H. Nelson, Amer. Assoc. Petr. Geologists Bulletin **93**, 329 (2009).
[2] R. G. Loucks *et al.*, J. Sed. Research **79**, 848 (2009).
[3] A. P. Radlinski *et al.*, Phys. Rev. Lett., **82** (15), 3078 (1999).
[4] A. P. R. Eberle *et al.*, *In preparation* 2013.

Probing the interlamellar amorphous phase in semicrystalline polyolefins using vapor flow

A. G. McDermott[1,2], C. R. Snyder[1], R. L. Jones[1,2]

The increasing popularity of shale-based sources of fuel, where byproducts of the extraction process are a cheap route to macromolecular synthesis, is driving a revolution in both commodity and high-performance polymer materials [1]. Key to this revolution is the development of new molecular architectures for polyolefin materials used to make polyethylene and hundreds of derivative plastics. To achieve new properties, materials chemists have pursued co-crystallized and blended structures by producing a wide array of molecular topologies including polyolefins with blocky main and side chains as well as compatibilizing side groups. While these strategies are thought to provide the range of properties necessary to meet emerging societal needs, there is a severe lack of direct measurements of the structure within a semicrystalline polymer. We report on developments of a new Small-Angle Neutron Scattering (SANS) method, using an infusion of labeled vapor into the amorphous polymer region to characterize structure and thermodynamics within semicrystalline polymers.

Semicrystalline polymers such as polyethylene often form sheet-like crystalline lamellae separated by amorphous material, termed here the "interlamellar" amorphous phase. "Extralamellar" amorphous regions can be found at grain boundaries and regions of uncrystallized material. These lamellar stacks may be randomly oriented (if crystallized without anisotropic stress), have a preferred orientation (if stretched or blown), or be nearly completely oriented (if crystallized under shear flow) (Fig. 1).

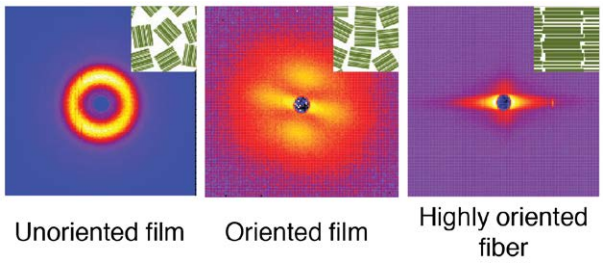

FIGURE 1: SANS patterns from polyethylene samples with contrast enhanced by absorption of cyclohexane-d_{12} or p-xylene-d_{10} vapor into the interlamellar amorphous material. Insets are statistical representations of the corresponding morphologies of the lamellar stack orientation, in (left to right) an unoriented film, an oriented film, and a highly oriented fiber.

Key to determining mechanical, barrier and other properties is the precise structure of chains within the interlamellar amorphous region. As shown in Fig. 2, these molecules can enter adjacent crystalline lamellae at both, one, or neither end. "Tie chains" spanning the interlamellar amorphous layer provide a direct mechanical function analogous to crosslinks in a network. While methods such as differential scanning calorimetry and mechanical stretching can be used to extract some indication of the conformation, composition, and density of molecules in this region, the measurements are indirect and often do not provide the required level of information.

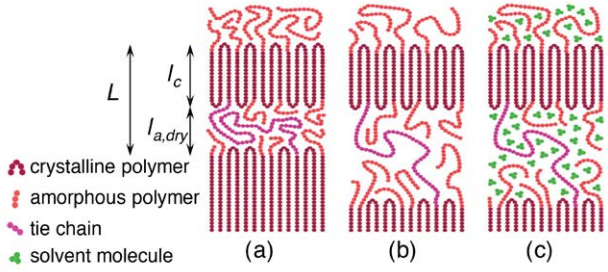

FIGURE 2: Semicrystalline polymer microstructure consisting of crystalline lamellae and interlamellar amorphous layers, (a) dry under no stress, (b) dry under external mechanical stress, and (c) swollen in solvent vapor.

Measuring equilibrium swelling as a function of solvent vapor activity is an established method of simultaneously determining the polymer-solvent interaction parameter and the effective tie-chain molecular weight [2-4]. Bulk measurements of swelling and solvent uptake, however, include contributions from both extralamellar and interlamellar amorphous material; they generally must also treat the permeant and amorphous phase as incompressible fluids. Because tie chains so strongly influence the properties of semicrystalline polymers, measurements of swelling and solvent uptake that are *independent* of one another as well as *specific* to interlamellar amorphous material are highly desirable.

Inspired to improve these equilibrium swelling experiments using scattering methods, we have utilized a vapor flow cell [5,6] at the NG-B 10m SANS instrument at the NIST Center for Neutron Research (NCNR) to measure structure within the interlamellar amorphous regions. Critically, the method relies on the permeability of amorphous polymer to a

[1]Materials Science and Engineering Division, National Institute of Standards and Technology, Gaithersburg, MD 20899
[2]nSoft, National Institute of Standards and Technology, Gaithersburg, MD 20899

chosen vapor and the impermeability of the crystalline phase to the same vapor. Polyolefins exhibit nearly zero scattering contrast between crystalline and amorphous phases. But when deuterated gas, such as cyclohexane-d_{12}, is allowed to permeate the amorphous region there is great neutron scattering contrast. When the swelling experiment described above is performed, the observed scattering peak is related to the long period of the lamellar structure, L. The degree of anisotropy of this peak is also indicative of the degree of orientation present, as described in Fig. 1.

In this *in situ* SANS swelling experiment, a melt-quenched sample of linear polyethylene SRM1475 [7] was equilibrated under cyclohexane-d_{12} vapor flow at several well-defined vapor activities. The dry long period, necessary to quantify the degree of swelling, was derived from an independent SAXS measurement. While a similar swelling experiment could also be carried out with SAXS, the larger contrast afforded using SANS independently quantified the amount of vapor absorbed; larger solvent vapor activities a_s caused the sample to absorb more vapor, producing larger scattering intensities as the peak shifted to lower wavevectors (Fig. 3).

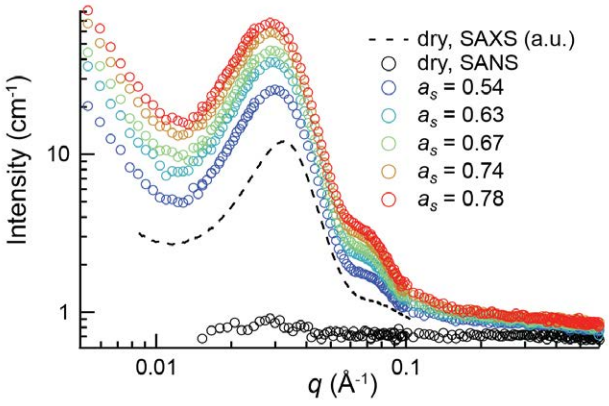

FIGURE 3: SANS patterns from an unoriented polyethylene film equilibrated under cyclohexane-d_{12} vapor flow at different solvent vapor activities a_s. A structure factor fit equating areas under peaks to the peak intensities of an ideal 1D lamellar structure yields the amorphous layer thickness.

The lamellae exhibit paracrystalline order; when distributions of crystal and amorphous layer thicknesses l_c and l_a are sufficiently narrow, higher-order peaks are observed. The areas under these peaks (Fig. 3) were taken as the peak intensities of a corresponding ideal one-dimensional lamellar structure, which are determined by a structure factor arising from the relative thicknesses of the amorphous and crystalline layers within the lamellar stacks. From differential scanning calorimetry measurements, $l_{a,dry}$ was known to be smaller than l_c. The thickness of the interlamellar amorphous layer as a function of vapor activity was thus extracted from SANS patterns.

From Flory-Rehner swelling theory [2] adapted for one-dimensional swelling [3], the interlamellar amorphous swelling ratio $l_a/l_{a,dry}$ can be related to the solvent activity a_s and an effective polymer-solvent interaction parameter χ_{eff} has a linear dependence as shown in Fig. 4.

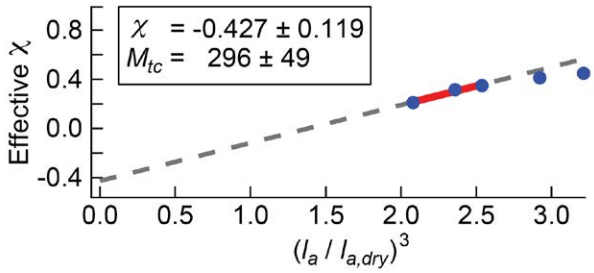

FIGURE 4: Fitting the data using the thermodynamic theory described in [3] yields an experimental measurement of the polymer-solvent interaction parameter χ and effective tie-chain molecular weight M_{tc}, both specific to the interlamellar amorphous fraction. Two points are omitted from the fit because samples did not reach equilibrium at the largest solvent activities.

The tie-chain molecular weight M_{tc} derived from the data in this study agrees well with literature values [3,4], considering that it likely depends sample history. The value of χ, while highly sensitive to choices in modeling and fitting the SANS patterns, differs from literature values derived from bulk measurements. Refinement of the modeling approach is required to reveal whether these differences are within measurement error or arise from variation in density and vapor solubility across the interlamellar amorphous region due to the presence of mesophases such as the rigid amorphous fraction.

Combining SANS and swelling experiments provides a uniquely specific measurement of effective tie-chain molecular weight in the interlamellar amorphous fraction. This property largely determines the mechanical performance of semicrystalline polymers and is strongly influenced by processing conditions. This technique also provides information about the thermodynamic property χ, describing polymer-solvent energetic interactions, specific to the interlamellar amorphous region. This is important in understanding the permeability of functional materials as well as the effect of processing techniques such as gel spinning and solvent casting. Both M_{tc} and χ may differ from values previously derived from bulk measurements of swelling. While these SANS swelling experiments were performed on unoriented films, the vapor contrast-enhancement technique is also applicable to oriented films and fibers.

References

[1] Plastics News, June 21, (2013).
[2] P. J. Flory, J. Rehner, J. Chem. Phys. **11** (11), 521 (1943).
[3] H. R. Brown, J. Polym. Sci.: Polym. Phys. **16** (10), 1887 (1978).
[4] C. E. Rogers, V. Stannett, M. Szwarc, J. Phys. Chem. **63** (9), 1406 (1959).
[5] M.-H. Kim and C. J. Glinka, J. Appl. Cryst. **38** (5), 734 (2005).
[6] M.-H. Kim and C. J. Glinka, Rev. Sci. Instr. **76** (11), 113904 (2005).
[7] C. A. Hoeve, *et al.*, Journal of Research of the NBS: A. Physics and Chemistry, **76A** (2) 137 (1972).

Fibrillar structure of methylcellulose hydrogels

J. W. McAllister[1], J. R. Lott[1], M. Wasbrough[2,3], F. S. Bates[4], and T. P. Lodge[1,4]

Methylcellulose (MC) is a commercially important polymer prepared by partial and heterogeneous replacement of cellulose hydroxyl moieties with methoxyl groups. When the degree of substitution per anhydroglucose unit is intermediate (*i.e.*, *ca.* 1.6 – 2.1), MC is a water-soluble polymer at low temperatures, and reversibly transitions to a turbid hydrogel at elevated temperature (Fig. 1) [1]. MC is categorized by the U.S. Food and Drug Administration as generally recognized as safe and has found use in a wide variety of products as thickeners or binders in pharmaceuticals, foods, and cosmetics as well as in building materials, ceramics, and cements. Despite widespread use of MC for nearly a century, the gel structure has been poorly understood. Fig. 1 shows the relationship between the thermogelation of MC by rheology and presence of fibrils by cryo-TEM. In this report, using a powerful combination of cryogenic transmission electron microscopy (cryo-TEM) and small-angle neutron scattering (SANS), we quantify fibril growth during MC thermogelation.

SANS for MC gels at 70 °C of 5 different concentrations is shown in Fig. 2a. Scattering of the gel is noted by a break in intensity scaling from $q^{-1.8}$ to $q^{-4.2}$ at $q \approx 0.015$ Å^{-1}, for a more than a decade of concentrations. This is notable [2], as it suggests that MC gels have a structure that is independent of concentration between (0.09 to 2.45) % mass fraction. A model for the form factor of a semiflexible cylinder, first proposed by Pedersen et al. [3,4] was used to model the fibril gels at temperatures above 70 °C:

$$I_{WC}(q,L,b,R_{CS}) = \phi_{cyl}(\Delta\rho)^2 S_{WC}(q,L,b)P_{CS}(q,R_{CS}) + bkg$$

Model fits for concentrations from (0.09 to 2.45) % mass fraction give a uniform fibril diameter of (14 ± 1) nm, in excellent agreement with cryo-TEM results. If the scattering length density (ρ_{cyl}) of the cylinder in the model was set to ρ_{MC} of MC, there was a systematic overshoot of the model fit to the experimental data shown in Fig. 2a. This

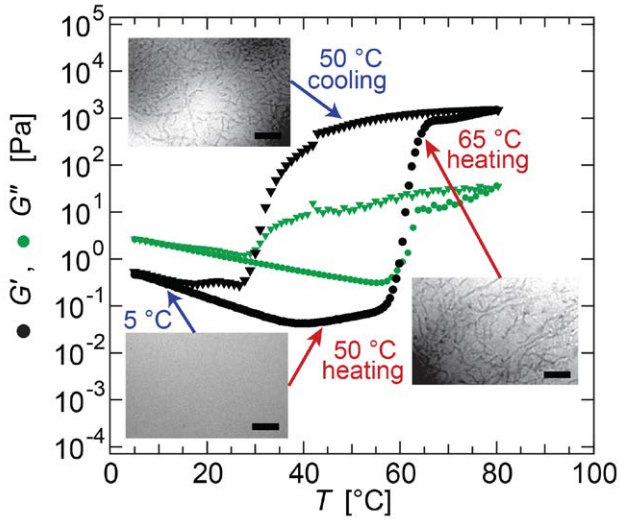

FIGURE 1: Storage (black) and loss (green) shear moduli, G' and G'' respectively, of an aqueous 1.4 % mass fraction MC solution with $M_w = 3.0 \times 10^5$ g/mol upon heating (circles) and cooling (triangles). Measurements were collected using a frequency of 1.0 rad/s, 5 % strain and a heating and cooling rate of 1 °C/min. When $G' < G''$ (2 °C to 60 °C on heating, 2 °C to 30 °C on cooling), no structure is visible by cryo-TEM. However, when $G' > G''$ (60 °C to 80 °C on heating, 30 °C to 80 °C on cooling), MC gels exhibit fibril structure of (15 ± 2) nm. All scale bars are 200 nm.

suggests that the fibrils of methylcellulose have a lower ρ than MC (expressed mathematically, $(\rho_{cyl} - \rho_{D_2O})^2 = x^2(\rho_{MC} - \rho_{D_2O})^2$, where x is the volume fraction of MC contained in the fibrils) and the volume fraction of cylinders can be related to the volume fraction of MC in the cylinders by the fraction x, $\phi_{cyl} = \phi_{MC}/x$. Therefore, SANS intensity is directly proportional to the volume fraction of MC in the fibrils, $I(q) \sim x$. Using this relation, the fibrils of MC were found to contain (40 ± 5) % volume fraction polymer, with the remainder of the fibril comprised of solvent.

Fig. 2b displays scattering intensity of a 1.09 % mass fraction solution of MC upon slow heating to the gel state at 70 °C. SANS and cryo-TEM suggest that MC exists primarily as semiflexible chains in solution at low temperatures, and the fibril structure develops upon heating, visible in the SANS by the growth of the slope break at $q = 0.015$ Å^{-1}.

[1]Department of Chemistry, University of Minnesota, Minneapolis, MN 55455
[2]NIST Center for Neutron Research, National Institute of Standards and Technology, Gaithersburg, MD 20899
[3]University of Delaware, Newark, DE 19716
[4]Department of Chemical Engineering & Materials Science, University of Minnesota, Minneapolis, MN 55455

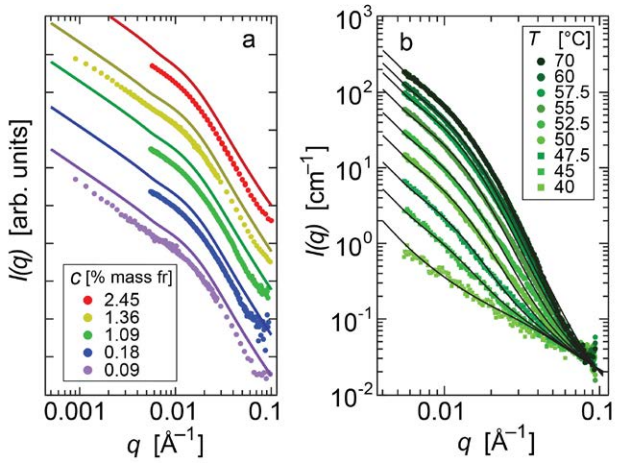

FIGURE 2: (a) SANS of MC gels at 70 °C, with corresponding model fits to a semiflexible cylinder model assuming the SLD of the cylinders is equal to MC. The systematic overshoot of the model compared to the data indicates that fibrils in MC gels contain (40 ± 5) % volume fraction polymer with the remainder solvent. Intensities have been shifted for clarity of viewing. (b) SANS of a 1.09 % mass fraction MC solution heated from 40 °C to 70 °C, and model fits to linear combinations of semiflexible chains (low *T*) to semiflexible cylinders (high *T*).

At temperatures less than 40 °C, SANS can be fit to a model for semiflexible chains in solution:

$$I(q) = aq^{-m} + \frac{I(0)}{1+q^2\xi^2} + bkg$$

modified from Chatterjee *et al.* [5] At temperatures above 70 °C, the semiflexible cylinder model is used with the appropriate ρ_{cyl} calculated from Fig. 2(a). For intermediate temperatures, linear combinations of the two models can be used to approximate the scattering intensities, and as seen in Fig. 2(b), the fit is very good. To achieve the model fits in Fig. 2, a number of assumptions were made. At 25 °C, the solution is assumed to have no fibrils, which is appropriate based upon our cryo-TEM results. At 70 °C, the gel is assumed to be comprised entirely of fibrils with no free chains. This is reasonable, based upon NMR results from Chatterjee *et al.* [5] showing a disappearance of the hydroxyl-water peak at 70 °C, indicating that MC molecules are associating very little with the surrounding solvent. Using this method, we are able to predict the scattering intensities during the entire heat-cool cycle of MC thermogelation.

Fig. 3 is calculated using the fraction of each model (semiflexible chains or semiflexible cylinders) applied to the fit at each temperature of the heat-cool cycle for MC. A "Fraction MC in fibrils" value of zero fibrils indicates that the semiflexible chain model was used exclusively, while a value of one indicates wholly the semiflexible cylinder model. Fig. 3 contains similar hysteresis upon heating and cooling to the storage modulus (G') of Fig. 1. This similarity strongly suggests that the growth of a fibril network is directly responsible for the elasticity of MC gels.

We report a correlation between SANS, rheology, and cryo-TEM for the thermoreversible gelation of aqueous MC solutions. Upon heating, MC develops fibrils with

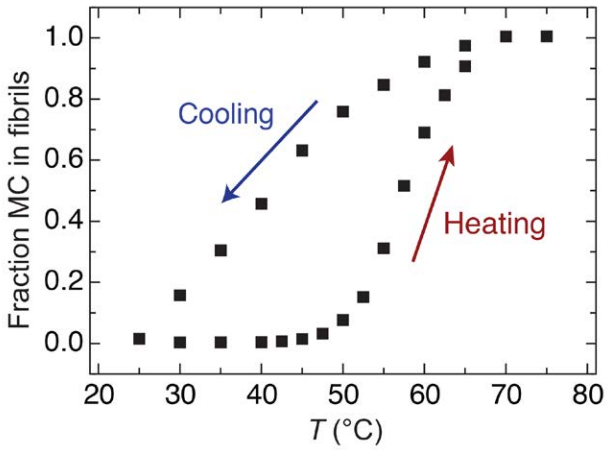

FIGURE 3: The distribution of MC between solution and fibrils upon heating and cooling, calculated from an analysis of linear combination of semiflexible chains (solution) and semiflexible cylinders (fibrils) illustrated in Fig. 2.

uniform diameters of (14 ± 1) nm, which is agrees very well with cryo-TEM images. Using differences between the scattering length density of fibrils and MC, it was found that MC fibrils contain (40 ± 5) % volume fraction polymer, and approximately 60 % mass fraction solvent for MC concentrations between (0.09 to 2.45) % mass fraction. Model fits during a heat-cool cycle of MC indicate that a solvent-swollen fibril network is responsible for the elastic behavior of MC gels at elevated temperature.

References

[1] S. A. Arvidson, J. R. Lott, J. W. McAllister, J. Zhang, F. S. Bates, T. P. Lodge, R. L. Sammler, Y. Li, M. Brackhagen. Macromol. **46** (1), 300 (2013).

[2] K. Kobayashi, C. Huang, T.P. Lodge, Macromol. **32** (21), 7070 (1999).

[3] J. S. Pedersen, P. Schurtenberger. Macromol. **29** (23), 7602 (1996).

[4] W. R. Chen, P. D. Butler, L. J. Magid, Langmuir **22** (15) 6539 (2006).

[5] T. Chatterjee, A. I. Nakatani, R. Adden, M. Brackhagen, D. Redwine, H Shen, Y. Li, T. Wilson, R. L. Sammler. Biomacromol. **13** (10), 3355 (2012).

Polymer chain mobility in confined polystyrene films

B. Akgun[1,2,3], M. D. Dimitriou[2], and S. K. Satija[2]

Thin polymer films are widely used in cutting-edge technologies including semiconductor processing, organic electronics, protective coatings, biological coatings, sensors, and filtration. The final structure and performance of a film is largely dictated by the processing conditions used in the production of a film. Furthermore, the processing methods used to create a film are greatly affected by the thermal properties of the polymers that make up the film. As such, the glass transition temperature (or *T*g, the temperature at which a polymer begins to flow) is a crucial property in determining a suitable processing method. However, as industry pushes to create polymers with greater functionality and smaller feature sizes, as well as thinner polymer films to cut cost, the soft matter community must reevaluate their conventional understanding of *T*g to include polymers that exist in a *confined* geometry within the thin film—an environment which differs drastically from the bulk conditions typically used to measure *T*g. Polymer mobility, which is inversely correlated with *T*g in bulk, is not only easier to quantify than *T*g, but better characterizes the behavior of the polymer within the thin film. Numerous studies have been dedicated to understand how *T*g and polymer mobility change in a confined geometry; however, little research has been performed to determine if and how the relationship between *T*g and mobility change when under confinement [1]. In this paper we investigate this relationship using samples where large *T*g reductions have been observed [2] suggesting an enhanced mobility in the vicinity of a film surface. We leverage the unique elemental contrast that neutron reflectometry (NR) offers to observe perpendicular mobility in stacked layers of miscible polymers where the sample film geometry confines the polymers [3].

To measure the mobility under confinement, we engineered two samples of equal total thickness (Fig. 1). First, a 40 nm thick layer of deuterated polystyrene (dPS) (M_n = 525,000 g/mol) was spin coated onto a silicon wafer. Next for the bilayer film, a 21 nm thick layer of hydrogenated polystyrene (hPS), of equal molecular weight to dPS, was floated on top to create a 61 nm bilayer film. The trilayer sample was created by floating first a 11 nm thick hPS and then a 9 nm thick dPS. The floating technique allowed us to generate stacks of polymer thin films with extremely sharp interfaces (less than 1.5 nm RMS roughness) between the hPS and dPS layers. The isotopic difference between hydrogen in hPS and deuterium in dPS creates an enhanced contrast when utilizing NR, allowing us to quantify both the layer thickness and interface width between layers with sub-nanometer accuracy. This distinct isotopic difference, however, did not alter the polymer mobility due to the fact that the two polymers are fully miscible at 525,000 g/mol. By using the bilayer and trilayer samples, we could monitor the dPS/hPS interface at three distinct depths from the air/film (free) surface: 9 nm (9TL), 20 nm (20TL), and 21 nm (21BL). Monitoring the interfaces as they broadened upon annealing enabled us to quantify perpendicular polymer mobility in a confined geometry and how it compares to polymer mobility in bulk.

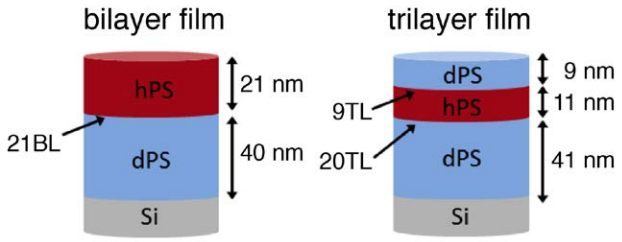

FIGURE 1: Schematic of the arrangement of bilayer and trilayer samples used in this work to characterize interfacial broadening of the three interfaces 21BL, 9TL, and 20TL.

The films were characterized using NR, generating a reflection profile as a function of momentum transfer vector perpendicular to the surface, *Q*. Next, both films underwent a set of equal annealing histories where the temperature was increased and reflectivity profiles were measured after each annealing step. Fig. 2a depicts the reflectivity profiles of the trilayer film after annealing. Each reflectivity profile was then fit to obtain a corresponding scattering length density depth profile (Fig. 2b) allowing us to determine the elemental composition and thickness of each layer, as well as the interfacial roughness between dPS and hPS layers. The rate at which the interface broadened was indicative of the polymer mobility due to interdiffusion between the miscible layers.

To negate differences in sample preparation the calculated interfacial roughness of each annealing step was normalized to the initial roughness prior to annealing. The normalized roughness values were then collapsed onto a universal curve using the time-temperature superposition principle (Fig. 3a). At ≈ 90 °C to ≈ 95 °C the chains become mobile and the broadening of all three interfaces progress at the same rate suggesting that polymer mobility, in the direction

[1]Bogazici University, Bebek 34342, Istanbul, Turkey
[2]NIST Center for Neutron Research, National Institute of Standards and Technology, Gaithersburg, MD 20899
[3]University of Maryland, College Park, MD 20742

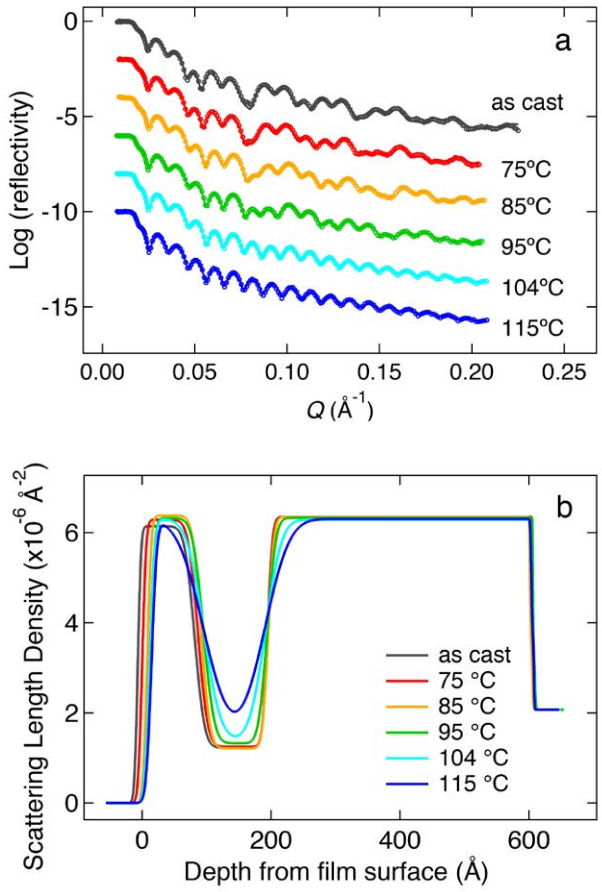

FIGURE 2: a) Evolution of trilayer reflectivity as a function of momentum transfer vector perpendicular to the surface, Q, taken intermittently during the anneal history. **b)** The scattering length density depth profile as determined by the best fit of the reflectivity.

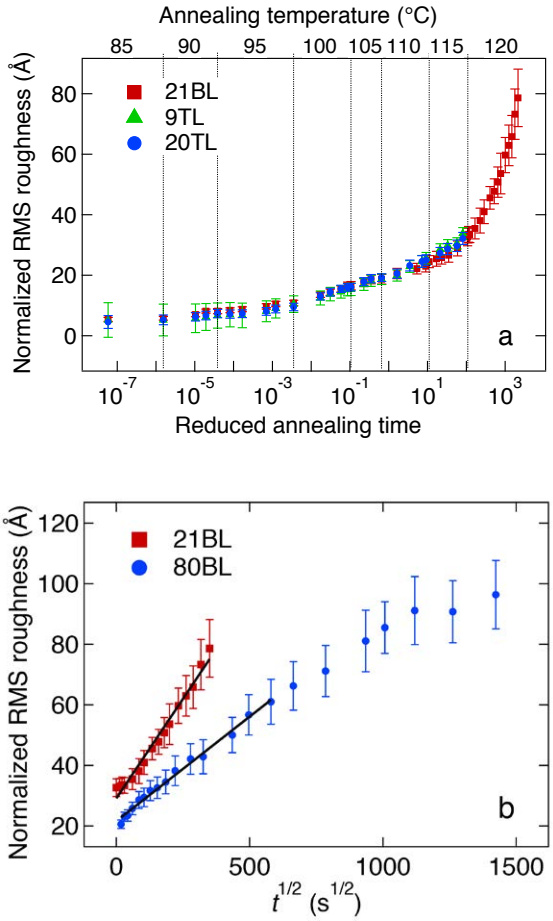

FIGURE 3: a) The normalized RMS roughness at each annealing step for each interface is collapsed onto a universal curve using time-temperature superposition showing the universality of the evolution of interfacial roughness. Error bars on data are statistical and are one standard deviation. **b)** The RMS broadening of 21BL compared to that of a bulk interface (80BL) at 120 °C shows the increased mobility in the confined films.

perpendicular to the film surface, is the same at both 9 nm and 20 nm depths for PS films. This result is notable and either contradicts earlier work stating that *T*g within these depths is not constant [2] or indicates that the relationship between *T*g and polymer mobility cannot be described as simply inversely correlated, as conventionally assumed.

To confirm that the system displays a correlation between the *T*g and polymer mobility, we compared the interfacial broadening rate of 21BL with that of a bulk system at 120 °C (Fig. 3b). To do this, we generated an additional bilayer sample using the same preparation methods as described earlier but significantly increased the film thickness to avoid polymer confinement effects. Both the dPS and hPS layers were 80 nm thick, resulting in a 160 nm thick bilayer film and an interface 80 nm from the film surface (80BL), so that the film displays bulk polymer properties. Fig. 3b shows the distinctly higher interfacial broadening rate for 21BL relative to 80BL indicating that we in fact observe increased polymer mobility in the confined thin film bilayer interface as compared to the bulk sample.

The unique scattering contrast that neutrons have to offer has allowed us to probe the interactions at an interface of two analogous polymer layers. This study addressed two major points. First, it showed that when compared to bulk conditions, confined polymer thin films show increased amounts of mobility, in agreement with previous research that found *T*g reduction under confinement. Second, the unique sample design allowed us to determine that there is no measureable difference in polymer mobility in confined, thin films at 9 nm and 20 nm depths. This finding suggests that either *T*g and polymer mobility are not correlated, or that there is no gradient in *T*g in polymer thin films between 9 nm and 20 nm from the air/polymer surface.

References

[1] J. A. Forrest, K. Dalnoki-Veress, Adv. Colloid Interface Sci., **94**, 167 (2001).
[2] C. J. Ellison, J. M. Torkelson, Nat. Mater., **2** (10), 695 (2003).
[3] B. Akgun, M. D. Dimitriou, S. K. Satija, *submitted.*

Small-angle neutron scattering reveals the size and shape of bottlebrush polymers in solution

S. L. Pesek[1], X. Li[1], B. Hammouda[2], K. Hong[3], and R. Verduzco[1]

Polymeric nanoparticles are a versatile class of materials currently being studied for a wide-range of applications including drug delivery, water purification, detection and sensing, and enhanced oil recovery. For each of these applications, the size and shape of the polymeric nanoparticles *in solution* underlies its target functionality. For example, in the case of targeted drug delivery, both nanoparticle size and shape impact circulation times, cellular uptake, and potential toxicity. However, measuring the size and shape of polymeric nanoparticles in solution can be significantly more challenging than analyzing dry nanoparticles adsorbed to a surface, which may not reflect the true nanoparticle characteristics in solution. Here [1], we report small-angle neutron scattering (SANS) measurements to quantify the size, shape, and flexibility of bottlebrush polymers in solution.

Bottlebrush polymers are nanoparticles with polymeric side-chains extending radially from a main-chain polymeric backbone and are promising for applications that rely on large, highly extended macromolecules and/or densely packed polymeric chains. These materials are of interest for drug delivery systems since the overall size and extension can in principle be controlled by the length and grafting density of the polymeric side-chains. However, a systematic study of bottlebrush polymer size and shape with varying molecular characteristics (backbone and side-chain length) has not been reported.

Bottlebrush polymers have two main components; (1) a main-chain backbone polymer with M repeat units and (2) side-chain polymers of N repeat units that are chemically attached to the backbone (Fig. 1, top). Through optimized polymerization reactions [2] we can tailor both M and N independently. We utilized a "grafting-through" method in which the side-chains are first synthesized, followed by a polymerization reaction to generate the bottlebrush polymer. Side-chain polystyrene polymers were synthesized *via* reversible addition-fragmentation chain-transfer (RAFT) polymerization followed by ring opening metathesis polymerization (ROMP) to form the norbornene-functionalized backbone polymer. The PS bottlebrush polymers have side-chain molecular weights M_W from (3.1 to 6.9) kg mol^{-1}, corresponding to side-chain degree of polymerization (DP) from N = 14 to N = 54, and overall molecular weights from (36 to 3,140) kg mol^{-1}, corresponding to backbone DP from M = 10 to M = 250. Bottlebrush polymer polydispersities (PDIs) range from 1.2 to 2.3.

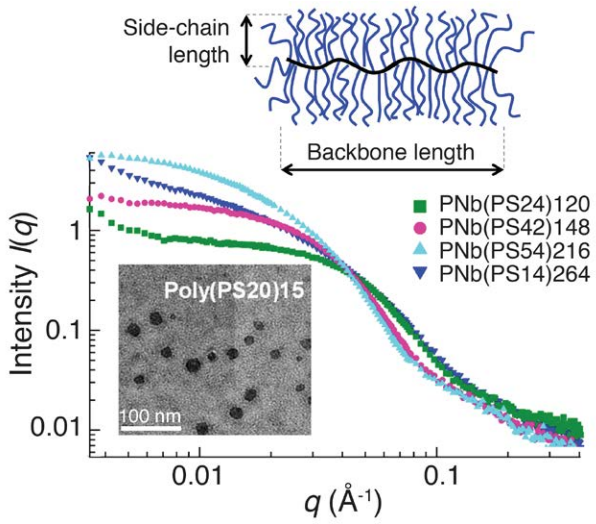

FIGURE 1: Schematic of a bottlebrush polymer (top) illustrating how the backbone length governs macromolecular length and side-chain polymers dictate radius or cross-sectional area. SANS data (bottom) and TEM micrograph (bottom, inset) for polystyrene bottlebrush polymers. Final PS bottlebrush polymers PNb(PS*N*)*M* have PS side chains with a degree of polymerization *N* and a backbone with a degree of polymerization *M*.

SANS analysis was performed over a q-range of 0.008 Å^{-1} to 0.4 Å^{-1}. This broad q-range provides information on the structure of bottlebrush polymers at multiple length scales. Roughly, the low-q region ($0.008 < q$ (Å^{-1}) < 0.02) gives information on the overall size of the bottlebrush polymer, the mid-q region ($0.02 < q$ (Å^{-1}) < 0.1) provides information about the cross sectional size and stiffness, and the high-q region ($q > 0.1$ Å^{-1}) is indicative of thermal fluctuations at the molecular level. SANS scattering curves are shown in Fig. 1. The plateau at low-q indicates fully dissolved bottlebrush polymers with little or no aggregates.

SANS data were analyzed using three different models. First, the Guinier-Porod model is a generic model that provides an estimate of overall size and shape for polymeric nanoparticles. Additionally, based on prior work with bottlebrush polymers [3,4], SANS data were analyzed using both rigid and semi-flexible cylinder models, the latter of which can provide an estimate of backbone flexibility. All three models predict similar trends in the radius or cross-section of bottlebrush polymers. The bottlebrush polymer radius is found to depend on side-chain length, as expected based on the known structure. From

[1]Rice University, Houston, TX 77251
[2]NIST Center for Neutron Research, National Institute of Standards and Technology, Gaithersburg, MD 20899
[3]Oak Ridge National Laboratory, Oak Ridge TN 37831

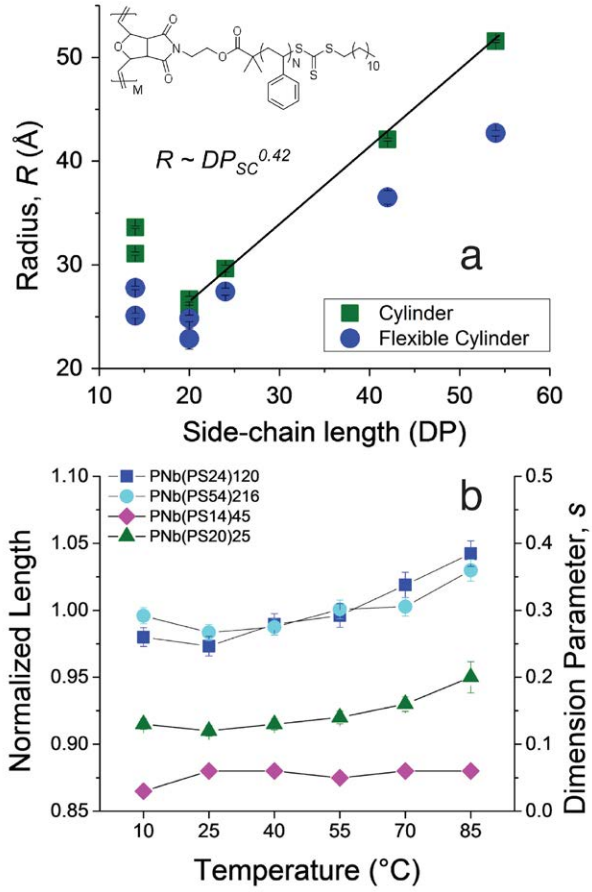

FIGURE 2: (a) Radius increase with side-chain length. (b) SANS data indicates that the backbone increases in length with increasing temperature. Error bars are one standard deviation.

the Guinier-Porod model, we observe a power-law dependence of the dimensions of the side-chains with side-chain DP, $R \sim DP^{0.39}$. Using the radius R from the cylindrical form factor models provides a slightly larger exponent of 0.42 (Fig. 2a). These numbers suggest a 2-D or 3-D self-avoiding walk conformation of the polymeric side-chains. Side-chains show an average length per repeat unit greater than 1 nm in all cases, indicating they are strongly stretched.

Analysis of SANS data by both Guinier-Porod and cylindrical form factor models predict a sphere-to-cylinder transition with increasing backbone DP, shown schematically in Fig. 3. The results for PS bottlebrush polymers show a more elongated solution conformation for PS bottlebrush polymers with DPs greater than 120, while bottlebrush polymers with smaller backbone DPs are roughly spherical globules in solution.

We can estimate the maximum dimension for bottlebrush polymers in solution using the Guinier-Porod model (diameter $D = 2\sqrt{2}\,R_g$) for bottlebrush polymers with backbone DPs less than 120 and the length predictions for bottlebrush polymers with backbone DPs greater than 120. As shown in Fig. 3, this analysis predicts the maximum dimension is independent of backbone length below backbone DPs of 120, where side-chain stretching determines the size of the bottlebrush polymer. Above

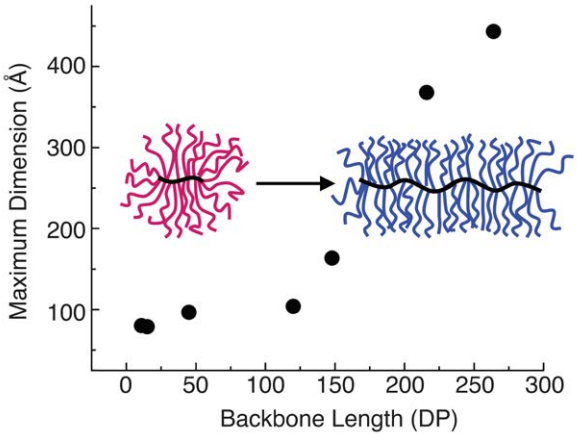

FIGURE 3: Bottlebrush polymers undergo a conformational change from spherical to cylindrical after the backbone length extends beyond the diameter of the polymer. For polymers studied here, this transition occurs around backbone DP of 120.

a backbone DP of roughly 120, the maximum dimension increases with backbone DP. While we observe this conformational transition at a backbone DP of roughly 120, this transition will generally depend both on side-chain length, flexibility, and grafting density.

Our results from the flexible cylinder model further indicate that the backbone is not fully stretched, with lengths of backbone per monomer repeat unit, l_b, roughly 0.18 nm ± 0.05 nm compared to the theoretical length for a fully extended backbone of roughly 0.5 nm. For bottlebrush polymers with backbone DPs greater than 120, temperature changes are found to only affect the backbone length and not bottlebrush polymer radius (Fig. 2b). This suggests that side-chains are highly stretched at all temperatures, while the backbone has more flexibility and reflects modest elongation with increasing temperature.

Polymer nanoparticles have significant promise for a number of applications, but quantitative knowledge of their conformation and size in solution is needed. Here, we demonstrated that SANS analysis provides detailed information of the size and shape of bottlebrush polymers in solution. SANS measurement reveal a change in shape from spherical to cylindrical, for bottlebrush polymers with increasing backbone length. This has not been previously reported experimentally but is consistent with predictions of recent multi-scale molecular simulations of bottlebrush polymers. This finding has direct implications for the design and development of bottlebrush polymers for a wide variety of applications.

References

[1] S. L. Pesek, X. Li, B. Hammouda, R. Verduzco, Macromolecules **46** (17) 6998 (2013).
[2] Z. Li, J. Ma, N. S. Lee, K. L. Wooley, J. Am. Chem. Soc. **133** (5), 1228 (2011).
[3] S. Rathgeber, T. Pakula, W. Agnieszka, K. Matyjaszewski, K. L. Beers, J. Chem. Phys. **122** (12), 124904 (2005).
[4] B. Zhang, F. Grohn, J. S. Pederson, K. Fischer, M. Schmidt, Macromolecules **39** (24), 8440 (2006).

A shear cell designed to probe the velocity-velocity gradient (1-2) plane of shear in complex fluids

A. K. Gurnon[1], P. D. Godfrin[1], N. J. Wagner[1], C. Lopez-Barron[1, 2], A. P. R. Eberle[1, 2], P. Butler[2], C. Gagnon[2,3], and L. Porcar[1, 4]

A new shear cell sample geometry for complex fluids is optimized for SANS and USANS structure measurements at the NCNR that probes the most useful projection of the microstructure under flow; the velocity-velocity gradient (1-2) plane of shear (Fig. 1). The new NCNR sample environment is available for use on the three SANS (NG-3, NG-7, and 10m SANS) and USANS (BT-5) instruments at the NCNR and on D22 at the Institut Laue-Langevin (ILL), as a collaborative development with the Center for Neutron Science at the University of Delaware and the ILL, Grenoble, France. Complex fluids encompass, but are not limited to, colloidal dispersions, surfactant solutions, emulsions, gels, glasses, proteins, biomaterials, foams, polymers and block copolymer solutions. Common to all is that oftentimes their processing and use involves flow. Hence, the study of soft matter forced out of equilibrium by shear flow is an important research area to improve formulation, processing, and manufacturing of complex fluids. The unique shear cell sample environment highlighted here represents a significant advance in our ability to understand the relationship between the microstructure of complex fluids and the macroscopic stress exhibited by these materials.

Recent manuscripts [1-3] discuss in varying detail the rheo- and flow-SANS methods. The sealed Couette shear cell sample environment is designed to generate a laminar shear field while simultaneous microstructure measurements are made using SANS or USANS (Fig. 1) [3]. Investigating the evolution of velocity gradient dependent phenomenon, such as shear banding [7], is now possible by performing spatially-resolved experiments using a narrow slit aperture (Fig. 1) [4,5] during start-up flow [6] using time-resolution capabilities available at the NCNR. Example results of a time-resolved flow-SANS experiment (Fig. 2) are shown for a shear thickening colloidal suspension during large amplitude oscillatory shear (LAOS) using time-resolved SANS. The example 2D SANS patterns demonstrate the formation of hydroclusters corresponding to the highest shear rate and can be quantitatively used to determine the mechanism underlying the associated stress response [7,8]. This example illustrates just one of many uses for studying complex fluids under shear flow using the newly commissioned 1-2 shear cell sample environment geometry in conjunction with spatial- and time-resolved neutron scattering methods at NIST. More information about this sample environment, including a video documenting its operation, is available from the Journal of Visual Experiments [3].

[1]University of Delaware, Newark, DE 19716
[2]NIST Center for Neutron Research, National Institute of Standards and Technology, Gaithersburg, MD 20899
[3]University of Maryland, College Park, MD 20742
[4]Institut Laue-Langevin, Grenoble Cedex 9, France

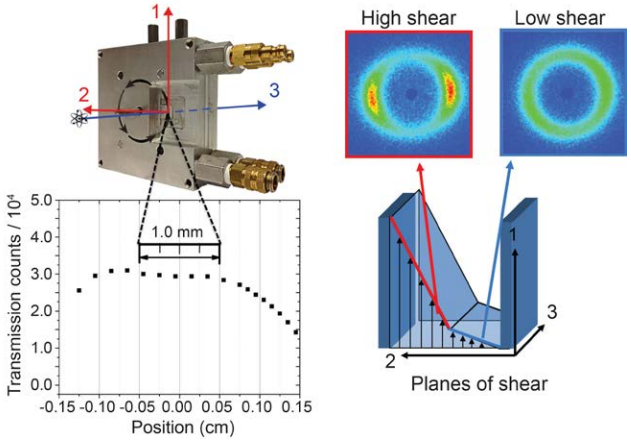

FIGURE 1: Left top: 1-2 shear cell geometry with velocity (1), velocity-gradient (2) and vorticity (3) shear directions indicated; bottom: counts as a function of position across the shear cell gap [3]. Right: Example of spatially resolved shear-banding.

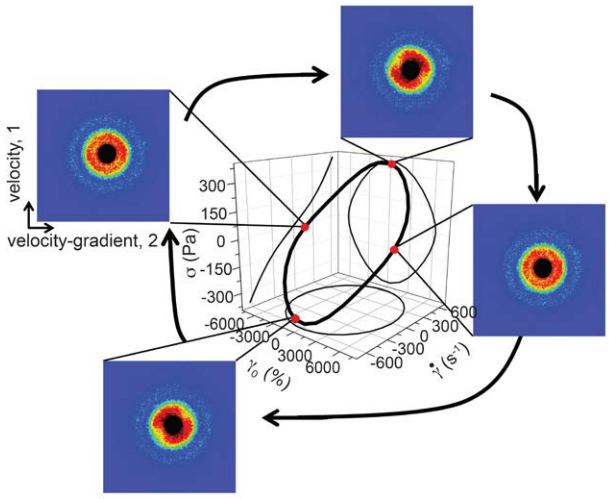

FIGURE 2: Shear thickening fluid (SiO_2 particles in d-ethylene glycol PEG-600 (70/30), $\phi_{effective} = 0.48$) during LAOS (oscillation frequency $\omega = 10$ rad/s and shear amplitude $\gamma_0 = 6278$ %). The black line is the viscoelastic rheometry stress response reported as a Lissajous curve accompanied by 2D SANS results from experiments made in the 1-2 plane of shear.

References

[1] A. P. R. Eberle, L. Porcar, Curr. Opin. Colloid Interface Sci. **17**, 33 (2012).
[2] L. Porcar, *et al.*, Rev. of Sci. Instrum. **82**, 083902 (2011).
[3] A. K. Gurnon, *et al.*, J. of Visual Exp. (In Press, 2013).
[4] M. W. Liberatore, *et al.*, Phys. Rev. E **73**, 020504 (2006).
[5] M. E. Helgeson, *et al.*, Phys. Rev. Lett. **105**, 084501 (2010).
[6] C. Lopez-Barron *et al.*, Phys. Rev. Lett. (submitted 2013).
[7] N. J. Wagner, J. F. Brady, Phys. Today **62**, 27 (2009).
[8] B. J. Maranzano, N. J. Wagner, J. Chem. Phys. **117**, 10291 (2002).

Rapid and accurate calculation of small-angle scattering profiles using the golden ratio

M. C. Watson[1] and J. E. Curtis[1]

Small-angle neutron and x-ray scattering have become invaluable tools for studying the nanoscale structure of biological molecules under near physiological conditions. While methods for measuring the overall size of molecules and the extent to which they are folded have long been established, determining three-dimensional molecular shape based on one dimensional small-angle scattering data remains one of the field's greatest challenges. Achieving this ambitious goal has been made possible with the advent of modern computing, where the theoretical scattering profiles of millions of candidate structures are calculated until a configuration that agrees with the experimental data is found [1]. However, calculating the scattering intensity based on atomic positions is extremely time-consuming, and imposes a serious bottleneck on the interpretation of experimental measurements. Similar limitations are also encountered when calculating the average scattering profile in molecular simulations.

We have devised a simple numerical method that significantly reduces this computational overhead [2]. While calculating the true scattering profile involves integrating over all scattering directions, we approximate it as a finite sum. The specific scattering directions used to evaluate the sum are chosen using the golden ratio, an irrational number known since the time of the ancient Greeks. Owing to a geometric property of the golden ratio, the scattering directions are uniformly distributed in all directions. This 'golden vector' approximation only consists of a few equations, allowing for easy customization [3].

The time required to calculate a scattering profile using the golden vector method scales as nN, where n is the number of scattering directions and N is the number of atoms in the molecule. The exact method scales as N^2. For biological molecules, N ranges from $N = 10^3$ to $N = 10^6$. Taking four biomolecules as examples, we found that using $n < 150$ orientations gives extremely accurate results (Fig. 1), offering tremendous time savings over the exact method. A previous approximation technique based on a multipole expansion [4] scales as NL^2 where L is the number of spherical harmonics. For a given level accuracy, we found that the golden vector method is much faster than the multipole technique for irregularly shaped molecules, while comparable in speed for quasi-spherical shapes (Fig. 2).

Though we have examined cases involving a single type of biomolecule in a dilute solution, the golden vector method can be applied to a host of other systems. The scattering pattern of a flexible molecule can be obtained by calculating the scattering profile of each molecular conformation, and taking the ensemble average. Our method can be readily applied to simulations of interacting molecules by extending the sum to include all solute atoms. The analysis of x-ray and neutron powder diffraction data for many nanocrystalline materials relies on the same "candidate structure" approach as described above, and suffers from a similar computational bottleneck. The golden vector method may potentially expedite this analysis as well.

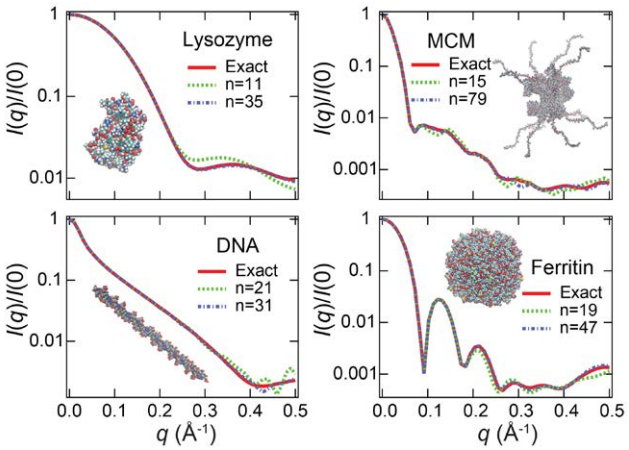

FIGURE 1: The calculated scattering profiles of lysozyme, MCM (mini chromosome maintenance complex), ferritin and a strand of DNA (images are not on the same scale). The red curves correspond to Debye's exact, but computationally expensive formula [2]. The blue and green curves were obtained using the golden vector approximation for different numbers of scattering directions.

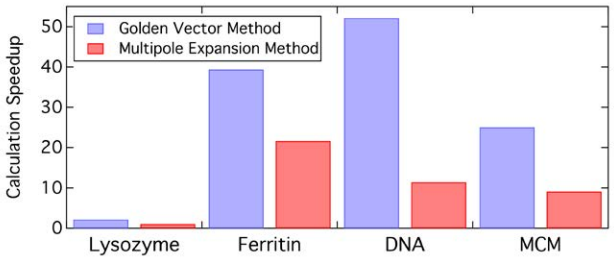

FIGURE 2: The speed improvement is shown as the calculation times required for the golden vector [3] and multipole expansion [4] techniques divided by the time needed to evaluate the exact formula. The timings shown correspond to 95 % agreement with the exact method.

References

[1] P. Chacón *et al.*, J. Mol. Biol. **299**, 1289 (1998).
[2] B. Warren, X-ray Diffraction. (1990).
[3] M. C. Watson, J. E. Curtis, J. Appl. Cryst. **46**, 1171 (2013).
[4] D. I. Svergun, C. Barberato, M. H. J. Koch. J. Appl. Cryst. **28,** 768 (1995).

[1]NIST Center for Neutron Research, National Institute of Standards and Technology, Gaithersburg, MD 20899

Advances in neutron flux measurement with the Alpha-Gamma device

A. T. Yue[1,2,3], M. S. Dewey[2], D. M. Gilliam[2], G. L. Greene[3,4], A. B. Laptev[5,6], and J. S. Nico[2]

Determining the flux (number of neutrons per second) of a neutron beam at the level of 0.1 % relative uncertainty has been an ongoing challenge for more than two decades, and it has applications in nuclear physics and neutron metrology. The ability to determine the flux at this precision is critical for beam-type neutron lifetime measurements [1], where the limiting systematic uncertainty has been the determination of the absolute neutron flux. A precise neutron flux technique will allow improved measurement of important neutron cross sections standards at near thermal energies, such as ^{6}Li, ^{10}B, and ^{235}U, where there is little data [2]. It can also be used to calibrate the emission rate of NBS-1, the national standard Ra-Be photo-neutron source whose current emission rate uncertainty is 0.85 % [3]. We present the results from the Alpha-Gamma (AG) device, a totally absorbing neutron detector that was recently used to measure the neutron flux of beam line NG-6M to better than 0.1 % and to improve the uncertainty in the detection efficiency of an important neutron monitor by a factor of five.

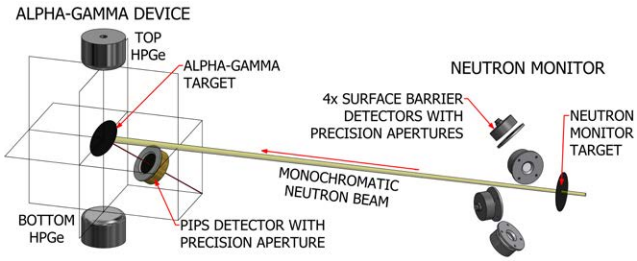

FIGURE 1: Schematic of the instrument setup on NG-6M.

The AG device determines the flux of neutrons impinging on a totally-absorbing ^{10}B-enriched boron carbide target by counting the 478 keV ^{10}B(n,γ)^{7}Li reaction gamma rays with high-purity germanium (HPGe) detectors [4]. The flux is determined from the measured gamma rate and the absolute detection efficiency of the HPGe detectors for the capture gamma. The gamma detection efficiency is determined in a separate calibration procedure in which the precisely known activity of an alpha source is successively transferred through a series of intermediate steps.

The AG device and a thin ^{6}LiF target-based neutron monitor were operated simultaneously on NG-6M, a monochromatic cold neutron beam (as shown in Fig. 1). A typical three-day measurement with the AG device determines the neutron flux to 0.07 % statistical uncertainty. The measured flux from the AG device and the measured rate of ^{6}Li(n,t)^{4}He reaction products in the neutron monitor are then used to determine the detection efficiency of the neutron monitor without reference to the ^{6}Li(n,t)^{4}He cross section or the target density. As shown in Fig. 2, data taken with three different beam collimations show good statistical consistency after correction for several systematic effects that may alter the efficiency. Including the uncertainties from systematic effects, the neutron monitor efficiency has been determined to 0.06 % with the AG device [5].

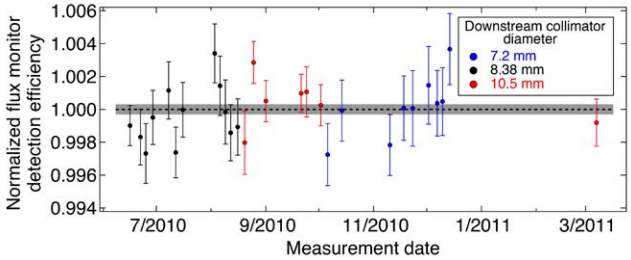

FIGURE 2: Normalized flux monitor detection efficiency measurements with the AG device for three beam collimations. Corrections for systematic effects depending on beam collimation are included. The error bars (± σ) are statistical only. The dashed black line is a weighted fit to the data, and the grey bar represents the 1σ uncertainty on the fit.

The AG device has allowed us to perform high-precision neutron flux measurements on beam line NG-6M, directly measuring the detection efficiency of an important neutron monitor to levels of uncertainty previously unattainable. This reduced uncertainty provides improved calibration of neutron sources and has spurred a new effort to measure the neutron lifetime [6] with significantly reduced uncertainty. In addition, we are pursuing a program that for the first time would allow direct measurement of neutron capture cross sections.

References

[1] J. S. Nico, *et al.*, Phys. Rev. C, **71**, 055502 (2005).
[2] M. S. Dewey, *et al.*, Proceedings of the 13th International Symposium on Reactor Dosimetry, 483 (2008).
[3] J. M. Adams, Nucl. Instrum. Methods B, **213**, 218 (2004).
[4] D. M. Gilliam, *et al.*, Nucl. Instrum. Methods A, **284**, 220 (1989).
[5] A. T. Yue, Ph.D. Thesis, University of Tennessee (2011).
[6] M. S. Dewey, *et al.*, Nucl. Instrum. Methods A, **611**, 189 (2009).

[1]University of Maryland, College Park, MD 20742
[2]Physical Measurement Laboratory, National Institute of Standards and Technology, Gaithersburg, MD 20899
[3]University of Tennessee, Knoxville, TN 37996
[4]Oak Ridge National Laboratory, Oak Ridge, TN 37831
[5]Los Alamos National Laboratory, Los Alamos, NM 87545
[6]Tulane University, New Orleans, LA 70118

Neutron Source Operations

December 7, 2012 was the 45-year anniversary of the initial startup of the NBSR. Many things have changed at the facility since that afternoon in 1967 when the Reactor Operations staff posed for a group photo (Fig. 1) with their Chief of Reactor Operations, Tawfik Raby. To celebrate the years of continuous and successful reactor operation, Tawfik visited the NCNR control room at the exact moment (3:55 PM) that he supervised the first criticality of the NBSR.

FIGURE 1: Tawfik Raby (front, center) and NBSR Reactor Operations and Engineering in 1967.

FIGURE 2: Tawfik Raby visiting the NBSR Control Room 45 years after initial reactor startup.

This past fiscal year, the NBSR operated for 238 days with 98.5% reliability. Only four scheduled operational days were lost but two of these were made up by extending the impacted cycles. This year, lost days were due to the reactor and the NCNR being preemptively shutdown for over a day due to hurricane Sandy. Unplanned shutdowns in past years caused by equipment failures or power outages have been minimized. Even with unplanned shutdowns and an extended maintenance period in the summer, the NBSR provided slightly less than the average number of experimental days per year in FY13.

A major activity for ROE this year was the replacement of the four reactor control shim arms. These four, motor-driven and aluminum-clad cadmium blades (arms) are used to control the NBSR power level and to shutdown the facility at the end of an experiment cycle. The arms must be replaced approximately every four years and this requires an extended shutdown (4 to 6 weeks). The longer shutdown and the removal of the shim arms this year provided an excellent opportunity to refurbish the four drive systems used by the reactor operators to remotely manipulate the arms and to upgrade a number of other reactor systems. All these activities were coordinated with Reactor Facility Operations (RFO) projects to minimize scheduling conflicts and the reactor restarted as scheduled at the end of the extended shutdown.

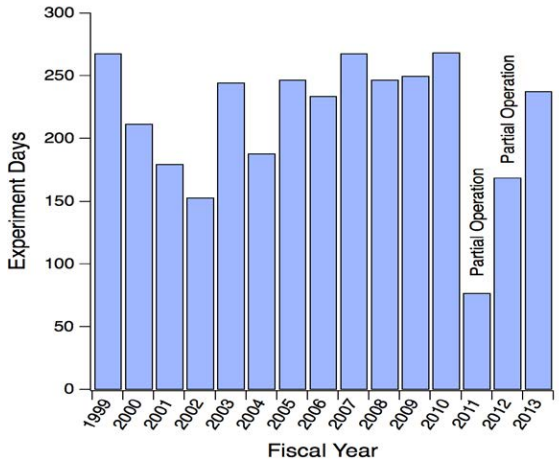

FIGURE 3: Number of NCNR Experimental Days per Fiscal Year 1999-2013.

FIGURE 4: Attila Halacsy and Greg Heller examine a new shim arm prior to installation.

Progress towards the installation of a liquid deuterium source continued this year with the purchase of a new 7 kW helium refrigerator (expected delivery in early FY14) and the fabrication or ordering of several large components for the system. The operating large liquid hydrogen cold neutron source serving the guide hall has not been ignored and an upgraded control system for the source was purchased this year to assure that aging and obsolete components of the original system are replaced before failure. This instrumentation and control upgrade will not only provide enhanced reliability of the two operating liquid hydrogen cold sources but will be compatible with the new liquid deuterium cold source control system saving time and money when the new system is installed in a few years.

Reactor Operations and Engineering continues to work with the National Nuclear Security Agency (NNSA) and several national laboratories to develop a replacement reactor fuel that will allow the NCNR to use low enriched uranium (LEU) in the future. The fuel manufacturer and the NNSA must demonstrate the safety of the proposed fuel and its cost-effective manufacturability prior to the NBSR conversion to LEU. Safety analysis, fuel testing, and the development of a manufacturing process is on-going with an expected NBSR conversion sometime in the next decade prior to the NCNR receiving a planned additional 20-year operation license in 2029.

Facility Development

Facility support staff effort has focused on instrument installation and redeployment to capitalize on the new guide network and cold source infrastructure completed during the recent NCNR Expansion Initiative.

Instrument Development

The Polarized Beam Reflectometer (PBR) and MAGIk, the new reflectometer dedicated to off-specular scattering, completed commissioning on guide NG-D and were the first instruments to enter the user program operating on the newly-installed supermirror guide network. Both instruments benefit from a larger beam area afforded by the new guide, with flux gains on PBR of nearly a factor ×3 compared to the previous installation on NG-1. MAGIk is now operating routinely with the high-resolution 2-D Denex detector and will be the first instrument to migrate to the Facility's new data acquisition and instrument control software – NICE (see below).

The NCNR's small-angle neutron scattering capacity has also been enhanced following the installation and commissioning of a new 10 m SANS machine. The 10 m instrument is situated on NG-B_{lower}, one of two low-divergence 50 mm × 50 mm cross-section guides on the new network that will be dedicated to the SANS program. The 10 m SANS is the flagship instrument supporting the neutron scattering program of nSoft, the new NIST-led consortium of industrial, government, and academic members promoting research and development programs focused on high impact issues in soft materials manufacturing.

The final sections of the NG-A guide have now been installed ready to service the Neutron Spin Echo spectrometer, which is being relocated from its historical location on NG-5. The NG-A guide is strongly curved (on a radius of 151 m) and direct line of sight is eliminated about 10 m from the cold source. The curvature has other operational advantages for the spectrometer, increasing its isolation from "contamination" from stray magnetic fields elsewhere in the Facility by gaining more distance from all neighboring beamlines. The final guide sections include a new polarizing cavity comprising supermirror coated "V"s of silicon wafers surrounded by 84 pieces of permanent magnet (NdFeB) to maintain a 500 G polarizing horizontal field for the supermirrors. The new polarizer promises improvements in beam polarization from the 80 % polarization at NG-5 to ≈ 99 % at NG-A. The relocated instrument will also benefit from all new power supplies to replace the obsolete and increasingly unreliable units used at NG-5. The new units are now in place at NG-A and have been connected to a dedicated 480 V/600 A supply—this is at least an order of magnitude more power than required for typical instrument installations at the Facility. Commissioning activities for the Spin Echo instrument will start towards the end of the year.

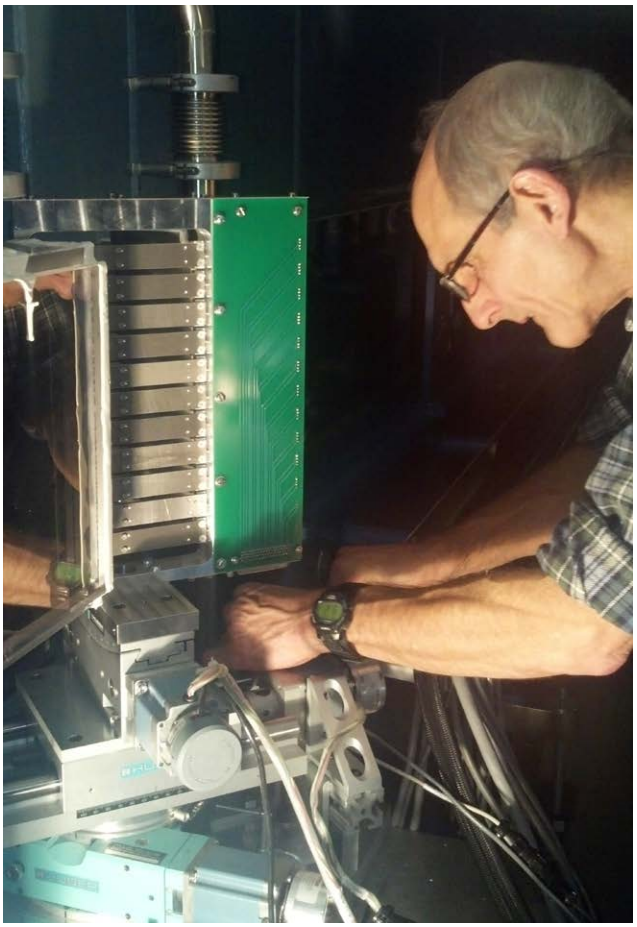

FIGURE 1: Chuck Majkrzak aligns the new pyrolitic graphite monochromator for PBR inside the NG-D guide bunker.

In the confinement building, the cold-neutron Multi-Axis Crystal Spectrometer returned to user operations as MACS-II following its relocation from NG-0 to BT-9. The move was necessary in order to open up a viewport on the liquid hydrogen cold source for the new guide network, and a new dedicated cold source, "*Peewee*", has been installed at BT-9 for MACS-II. The *Peewee* cold source has realized its design specification to provide a smaller (half the size) but brighter (factor ×2) source of cold neutrons optimized for the spectrometer and offering considerable gains in signal-to-background for the typical sample sizes used in experiments

on the spectrometer. As part of the move, MACS was also upgraded to operate with a selection of cold filters on both the incident and scattered beams and, once again, these have already been shown to improve significantly signal-to-background on the spectrometer.

FIGURE 2: (left) Jim Moyer and Bill Clow install the monochromatic cold filter exchanger (MCFX) on the MACS analyzer system. (right) Danny Ogg and Eli Baltic lower into place the new incident beam cold filter exchanger (CFX) on MACS' front end at BT-9.

Neutron Spin Filters

The NCNR promotes an active program, operated in collaboration with the Physical Measurement Laboratory at NIST, to provide and develop ^{3}He neutron spin filters (NSFs) to support high quality research using polarized neutrons. During the past year, the NCNR's spin filter program serviced 15 user experiments, for a total of 58 days of beam time and 83 bar-liters of polarized ^{3}He gas.

Polarized beam experiments are routinely carried out on the thermal neutron triple-axis spectrometer BT-7 and on the small-angle neutron scattering instruments. ^{3}He gas is polarized by spin-exchange optical pumping (SEOP), in which alkali-metal atoms are polarized by optical pumping and the resulting electronic polarization is transferred to ^{3}He nuclei in spin-exchange collisions. The goal is always to improve polarized neutronic performance and several large high-pressure cells have been successfully fabricated to meet demands of polarized inelastic experiments on BT-7. Improvements in polarization values have also been made, with a record value of 85 % in a large spin filter cell having now been achieved. The improvements were observed following conversion of the feedback element in the spectral narrowing scheme from a conventional diffraction grating to a chirped volume Bragg grating. The result, although welcome, was somewhat unexpected since prior studies had indicated that the alkali-metal polarization was unity and the ^{3}He polarization was limited to 80 % by the temperature dependence of ^{3}He relaxation under SEOP conditions. The origin of this gain is currently under investigation as the underlying physics likely has important implications for the limits of the SEOP technique.

Efforts continue to develop standard protocols for the routine use of NSFs in polarized neutron scattering measurements at the NCNR. These protocols include NMR and ^{3}He spin flipping devices and their associated software and an interface enabling communications between an instrument computer and IGOR-based ^{3}He NMR software. These user-friendly protocols have been implemented on dedicated spin filter apparatus for use on both BT-7 and the NG-3 and NG-7 SANS instruments. Similar systems are currently under development on the recently-commissioned MACS-II and MAGIk.

There have been a number of advances made on polarized neutron instrumentation for the individual instrument classes. For triple-axis experiments on BT-7 a polarized beam configuration has been implemented that capitalizes on earlier breakthroughs to reduce ^{3}He spin flip losses by two orders of magnitude and realize compact adiabatic spin rotation devices. Key features of the configuration include single or multiple adiabatic spin rotators, depending on whether the instrument is configured for polarization, P, perpendicular to Q, or P parallel to Q. The energy dependence and spatial uniformity of the spin transport has been characterized at better than 99 % for neutron energies up to 50 meV. Moreover, the spin transport efficiency is uniform over a wide range of scattering angles, a feature required in particular for the configuration of P parallel to Q. The nearly perfect spin transport is complemented by an observed flipping ratio of 85 % with an intensity reduction factor of only 9.5 % as compared to an unpolarized beam configuration. This level of performance using a combination of a pyrolitic graphite monochromator and ^{3}He NSF is better than that achieved using Heusler crystal polarizers.

On the SANS instruments, polarization analysis development has focused on soft matter investigations. For a number of soft matter systems, extracting the weak coherent scattering from the sample at high Q is extremely challenging without accurate knowledge of the Q-independent nuclear spin-incoherent background. Polarization analysis in combination with the time-of-flight (TOF) technique has been used to eliminate background from the inelastic scattering, and thus allow an accurate separation of coherent and spin-incoherent scattering. Refinement of the experimental procedures and data analysis methods for this technique is on-going and further tests of this challenging soft-matter application will be done in the future.

In addition, a compact in-situ SEOP system has been designed applicable for low-field SANS polarization analysis in both hard and soft matter research. The system

enables a constant ^{3}He polarization to be maintained and decreases sensitivity to stray fields. The system incorporates a compact oven with silicon windows for neutron passage, a ^{3}He flipping device, and a laser with associated optics and controllers. A dedicated system for NMR and ^{3}He spin flipping has been implemented and offline tests of the system are in progress.

Finally, following the commissioning of MACS-II, the development program for wide-angle neutron polarization analysis apparatus has restarted. The cells cover angles up to 110° on either side of the neutron beam and the latest layout consists of a vertical, neutron-compatible, solenoid that contains a spin filter polarizer and analyzer cell situated close to the tail of a sample cryostat. The polarizer cell is contained in a shielded radio-frequency solenoid to permit inversion of the ^{3}He polarization via adiabatic fast passage NMR without loss of polarization in the analyzer cell. Free induction decay NMR is used to monitor the ^{3}He polarization in the spin filter cells. During preliminary testing a magnetic field gradient was discovered that led to reduced storage times for the polarized gas. A simple magnetic shield has since been used to block the stray fields originating from the MACS pre-sample optics without undue distortion of the highly homogeneous solenoid field. Further tests are required to validate this configuration but the research experiments using neutron polarization on MACS-II are expected to begin later his year.

Data Acquisition Software

Progress has continued in developing the New Instrument Control Environment software package (NICE) and the first deployment is now rolled out on MAGIk. The NICE project seeks ultimately to replace all the legacy software systems currently deployed at the NCNR with a modern and readily-extensible system common to all instrument classes. NICE is a Java-based package that incorporates a highly versatile scripting capability to enable end user adaptations to be coded under all the major scientific programing languages. Test releases of the new code are also available for the SANS instruments, the neutron spin echo spectrometer, and a basic triple-axis spectrometer.

Data Analysis Software

Development activity continues on the reflectometry analysis package, Refl1d, spawned from the DANSE (Distributed Data Analysis for Neutron Scattering Experiments) project. This package is used by many of our external users to fit their more complicated reflectometry models and a number of new features were added to make it easier to define and manipulate these models.

Recently, *bumps*, the fitting engine at the core of Refl1d, has been separated from the fitting package and made available as a separate python application, which can be used to fit arbitrary models to data and report uncertainty in the fitting parameters. This program has been undergoing continual improvements to make it easier to construct models and share parameters between models for simultaneous fitting. Support for Message Passing Interface (MPI) parallelism has also been added to *bumps*, to facilitate runs on large computer clusters such as Kraken at Oak Ridge National Laboratory.

The NCNR is also a contributor to the international SANS team working to develop the DANSE/SASview software package. The plug-in architecture has been redesigned to make it easier for developers and end users to add their own models in a compiled language and the first steps have been taken to incorporate the *bumps* fitting engine into SASView.

The Data Analysis and Visualization Environment (DAVE) project provides software solutions for a range of inelastic neutron scattering instruments at the NCNR and elsewhere. It is widely used by scientists to reduce, view and interpret their data and also for experiment planning. The software suite is fully supported on the three widely used computer platforms – Microsoft Windows, MacOS X and Linux and is freely available for download from the Internet. Currently, DAVE is a mature product with regards to its functionality, although it continues to evolve and expand to accommodate the needs of the Facility and its users.

The data reduction module for the MACS instrument has been completely overhauled and is now fully supported through the Mslice reduction and analysis module. Thus visualizing and manipulating multiple datasets from MACS is more straightforward with the inclusion of slicing and cutting capabilities for volumetric data. In addition, experiment planning and scan setup tools are now available. For SPINS, a new reduction module is now in place for handling data from the position-sensitive detector. However, it is not yet feature complete as only data from powder samples is currently supported – support for a single crystal is planned. Numerous upgrades were applied to the BT-7 reduction software to support new features such as background subtraction, monitor correction and a raw view mode that adds to the existing powder and single crystal modes.

A new genetic algorithm known as differential evolution (DE) is now an integral part of the peak analysis module (PAN) in DAVE. DE employs a population-based stochastic search approach to optimize the function parameters to

be fitted. In conventional DE, a mutation strategy and associated control parameters are selected to produce an evolution of the initial population of parameter vectors in future generations until a satisfactory solution is reached. Unfortunately, the performance of the algorithm is very sensitive to the choice of mutation strategy and the value of the control parameters. It is essentially problem-dependent. In our implementation we have employed a recent technique in which a pool of mutation strategies and control parameter values are used simultaneously and compete to produce a successful offspring generation. One significant advantage of this approach, which also happens to align perfectly with the goals of DAVE, is that the process is transparent to the end user since it is not necessary to make a choice about what mutation strategy to select. The end result is a DE algorithm that is as straightforward to use as the existing Levenberg-Marquardt (LM) gradient search algorithm already in PAN. The LM algorithm remains the default but users can switch to and from the DE algorithm as required. However, for the DE, the user must specify the upper and lower bounds of the parameters to be fitted. In the figure, a fit of the "mean field order parameter" function to BT-7 data generally produces mixed results using the LM algorithm while switching to DE always produces an excellent fit as shown.

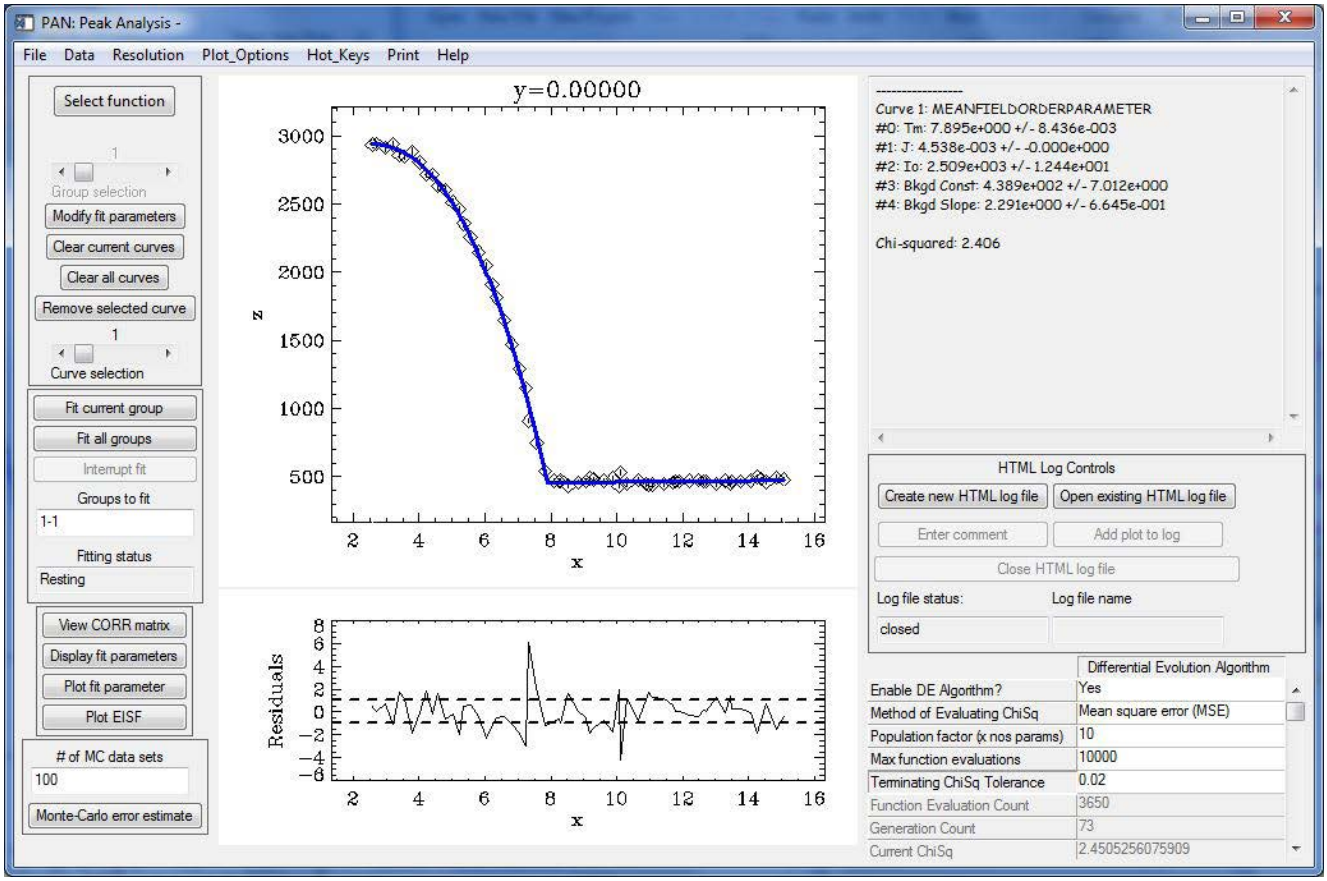

FIGURE 3: Using the new Differential Evolution (DE) fitting algorithm in PAN to fit a mean field order parameter function to BT7 data. The user controls for the DE are shown in the bottom right section of the PAN interface. Using the Levenberg-Marquardt algorithm generally produces mixed results for this function. PAN uses the LM algorithm by default but switches to the DE algorithm if 'Enable DE Algorithm' is selected.

Serving the Science and Technology Community

The mission of the NIST Center for Neutron Research is to ensure the availability of neutron measurement capabilities to meet the needs of U.S. researchers from industry, academia and from other U.S. government agencies. To carry out this mission, the NCNR uses several different mechanisms to work with participants from outside NIST, including a competitive proposal process, instrument partnerships, and collaborative research with NIST.

Proposal System

Most of the time on NCNR instruments is made available through a competitive, peer-review proposal process. The NCNR issues calls for proposals approximately twice a year. Proposals are reviewed at several different levels. First, expert external referees evaluate each proposal on merit and provide us with written comments and ratings. This is a very thorough process where several different referees review each proposal. Second, the proposals are evaluated on technical feasibility and safety by NCNR staff. Third, we convene our Beam Time Allocation Committee (BTAC) to assess the reviews and to allocate the available instrument time. Using the results of the external peer review and their own judgment, the BTAC makes recommendations to the NCNR Director on the amount of beam time to allocate to each approved experiment. Approved experiments are scheduled by NCNR staff members in consultation with the experimenters.

The current BTAC members are:

- Andrew Allen (NIST Ceramics Division)
- Jeffrey Allen (Michigan Technological University)
- Collin Broholm (Johns Hopkins University)
- Leslie Butler (Louisiana State University)
- Kushol Gupta (University of Pennsylvania)
- Hye-Jung Kang (Clemson University)
- Ramanan Krishnamoorti (University of Houston)
- Valery Kiryukhin (Rutgers University)
- Jennifer Lee (National Institutes of Health)
- Janna Maranas (The Pennsylvania State University)
- Steven May (Drexel University)
- Alan Nakatani (Dow Chemical Company)
- Danilo Pozzo (University of Washington)
- Stephan Rosenkranz (Argonne National Laboratory)
- Gila Stein (University of Houston)
- Lynn Walker (Carnegie-Mellon University)

Partnerships

The NCNR may form partnerships with other institutions to fund the development and operation of selected instruments. These partnerships, or "Participating Research Teams", may have access to as much as 75 % of the available beam time on the instrument depending on the share of total costs borne by the team. A minimum of 25 % of the available beam time is always made available through the NCNR proposal program to all users. Partnerships are negotiated for a fixed period (usually three years) and may be renewed if there is mutual interest and a continued need. These partnerships have proven to be an important and effective way to expand the research community's access to NCNR capabilities and have been very successful in developing new instruments.

Collaboration With NIST

Some time on all instruments is available to NIST staff in support of our mission. This time is used to work on NIST research needs, instrument development, and promoting the widespread use of neutron measurements in important research areas, particularly by new users. As a result of these objectives, a significant fraction of the time available to NIST staff is used collaboratively by external users, who often take the lead in the research. Access through such collaborations is managed through written beam time requests. In contrast to proposals, beam time requests are reviewed and approved internally by NCNR staff. We encourage users interested in exploring collaborative research opportunities to contact an appropriate NCNR staff member.

Research Participation and Productivity

The NCNR continued its strong record of serving the U.S. research community this year. Over the 2013 reporting year, 2,148 research participants benefited from use of the NCNR. (Research participants comprise users who come to the NCNR to use the facility as well as active collaborators, including co-proposers of approved experiments, and co-authors of publications resulting from work performed at the NCNR.) As the number of participants has grown, the number of publications per year has increased proportionately. The quality of the publications has been maintained at a very high level. The trend of the past few years, however, suggests that the number of participants and publications is beginning to saturate, as one might expect as the capacity of the facility is reached. Completion of instruments associated with the Expansion Initiative that has taken place over the past few years promises increasing activity and productivity.

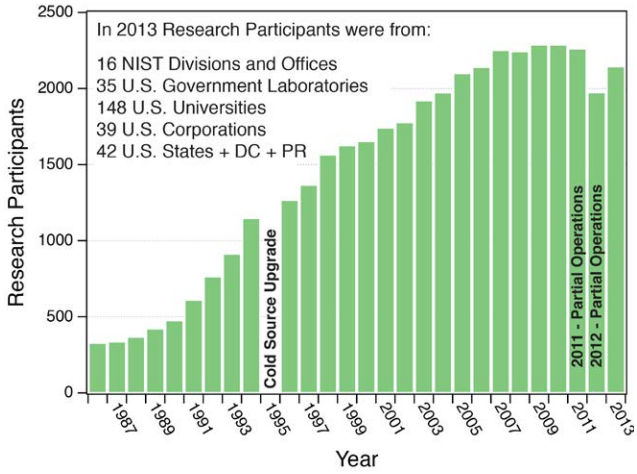

FIGURE 1: Research participants at the NCNR 1986- 2013.

2013 NCNR Proposal Program

Two calls for proposals for instrument time were issued in the past year. We received 659 proposals, of which 393 were approved and received beam time. The oversubscription, *i.e.*, the ratio of days requested on all proposals to the days available, was 2.1 on the average, but as high as 3.0 for specific instruments. Proposal demand has grown constantly since the NCNR first began accepting proposals in 1991, and has doubled in the past eight years. The following table shows the data for several instrument classes.

Instrument class	Proposals	Days requested	Days allocated
SANS and USANS	262	994	460
Reflectometers	113	728	348
Spectrometers	235	1581	714
Diffraction	21	65	46
Imaging	28	129	104
Total	659	3497	1672

Users Group Holds Election

The NCNR Users Group (NUG) provides an independent forum for all facility users to raise issues to NCNR management, working through its executive officers to carry out this function. The group held its fourth election in early 2013, choosing four new members for the NUG Executive Committee. The newly elected members are Kate Gurnon (University of Delaware, student/postdoc member), (Alan Nakatani (Dow Chemical), Megan Robertson (University of Houston), and Michael Mackay (University of Delaware). Remaining on the committee are Despina Louca (University of Virginia, chair), John Katsaras (Oak Ridge National Laboratory), and Dale Schaefer (University of Cincinnati).

Panel Of Assessment

The major organizational components of NIST are evaluated annually for quality and effectiveness by the National Research Council (NRC), the principal operating agency of both the National Academy of Sciences and the National Academy of Engineering. A panel appointed by the NRC last reported on the NIST Center of Neutron Research in July 2013. The report from that meeting is not yet publicly available, but the findings of a prior meeting are summarized in a document that may be viewed online at http://www.nist.gov/director/nrc/upload/nr-panel-2011-final-report.pdf. The panel members included Paul Fleury, Yale University, Laura Greene, University of Michigan, Andrew Harrison, Institut Laue-Langevin, Grenoble, Alan Hurd, Los Alamos National Laboratory, Dale Klein, University of Texas, Wade Konze, Dow Chemical, Roger Leach, DuPont Central Research and Development, Brian Maple, University of California, San Diego, and David Weitz, Harvard University.

The Center For High Resolution Neutron Scattering (CHRNS)

CHRNS is a national user facility that is jointly funded by the National Science Foundation and the NCNR. Its primary goal is to maximize access to state-of-the-art neutron scattering instrumentation for the research community. It operates six neutron scattering instruments at the NCNR, enabling users from around the nation to observe dynamical phenomena involving energies from ≈ 30 neV to ≈ 100 meV, and to obtain structural information on length scales from ≈ 1 nm to ≈ 10 μm. A more detailed account of CHRNS activities may be found on p. 57 of this report.

Partnerships For Specific Instruments

NG-7 SANS Consortium

A consortium that includes NIST, the ExxonMobil Research and Engineering Company, and the Industrial Partnership for Research in Interfacial and Materials Engineering (IPRIME) led by the University of Minnesota, operates, maintains, and conducts research at the NG-7 30 m SANS instrument. The consortium uses 57 % of the beam time on this instrument, with the remaining 43 % allocated to the general scientific community through the NCNR's proposal system. Consortium members conduct independent research programs primarily in the area of large-scale structure in soft matter. For example, ExxonMobil has used this instrument to deepen their understanding of the underlying nature of ExxonMobil's products and processes, especially in the fields of polymers, complex fluids, and petroleum mixtures.

The nSoft Consortium

Formed in August 2012, the nSoft Consortium allows member companies to participate with NIST in the development of advanced measurements of materials and manufacturing processes, and develop their own expertise in state-of-the-art measurement technologies to include in their analytical research programs. nSoft develops new neutron-based measurement science for manufacturers of soft materials including plastics, composites, protein solutions, surfactants, and colloidal fluids. Members receive access to leading expertise and training support in neutron technology and soft materials science at the NIST Center for Neutron Research, the NIST Materials Science and Engineering Division, and the University of Delaware. Contact: Ron Jones, nSoft Director, rljones@nist.gov, 301-975-4624.

NIST / General Motors – Neutron Imaging

An ongoing partnership and collaboration between General Motors and NIST continues to yield exciting results using neutron imaging. Neutron imaging has been employed to visualize the operation of fuel cells and lithium-ion batteries for automotive vehicle applications. Neutron imaging is an ideal method for visualizing hydrogen and lithium, the fuel of electric vehicle engines. These unique, fundamental measurements, provide valuable material characterizations that will help improve the performance, increase the reliability, and reduce the time to market introduction of the next generation electric car engines. 25 % of the time on the BT-2 Neutron Imaging Facility is made available to the general scientific community through peer-reviewed proposals.

Interagency Collaborations

The Smithsonian Institution's Nuclear Laboratory for Archeological Research is part of the Anthropology Department at the National Museum of Natural History. It has had a productive 34 year partnership with the NCNR, during which time it has chemically analyzed over 43,100 archaeological artifacts by Instrumental Neutron Activation Analysis (INAA), drawing extensively on the collections of the Smithsonian, as well as on those of many other institutions in this country and abroad. Such chemical analyses provide a means of linking these diverse collections together in order to study continuity and change involved in the production of ceramic and other artifacts.

The Center for Food Safety and Applied Nutrition, U.S. Food and Drug Administration (FDA), maintains laboratory facilities at the NCNR providing agency-wide analytical support for food safety and food defense programs. Neutron activation (instrumental, neutron-capture prompt-gamma, and radiochemical), x-ray fluorescence spectrometry, and low-level gamma-ray detection techniques yield multi-element and radiological information about foods and related materials and provide a metrological foundation for FDA's field investigations and for radiological emergency response planning. Current studies include development and validation of swordfish and cocoa powder in-house reference materials, measuring cesium levels in soil to study cesium uptake behavior into food products, rapid screening of food for dangerous levels of toxic elements, analysis of rice products for arsenic, and quantification of iodine in dietary supplements.

The Center for High Resolution Neutron Scattering (CHRNS)

The Center for High Resolution Neutron Scattering is a national user facility that is jointly funded by the National Science Foundation through its Division of Materials Research (grant number DMR-0944772) and by the NCNR. The primary purpose of this partnership is to maximize access to state-of-the-art neutron scattering instrumentation for the research community using the NCNR's proposal system. Proposals to use the CHRNS instruments are critically reviewed on the basis of scientific merit and/or technological importance. The core mission of CHRNS is fourfold: (i) to develop and operate neutron scattering instrumentation, with broad application in materials research, for use by the general scientific community; (ii) to promote the effective use of the CHRNS instruments by having an identifiable staff whose primary function is to assist users; (iii) to conduct research that advances the capabilities and utilization of CHRNS facilities; and (iv) to contribute to the development of human resources through educational and outreach efforts.

Scattering Instruments and Research

During FY 2013, CHRNS supported operation of the following instruments: the NG-3 30 m Small Angle Neutron Scattering (SANS) instrument, the Ultra-Small Angle Neutron Scattering (USANS) instrument, the Multi-Angle Crystal Spectrometer (MACS), the Disk Chopper Spectrometer (DCS), the High Flux Backscattering Spectrometer (HFBS), and the Neutron Spin-Echo (NSE) spectrometer. The small angle scattering instruments together provide structural information over length scales from ≈ 1 nm to ≈ 10 μm. The spectrometers collectively yield dynamical information over time scales from ≈ 3 x 10^{-14} s to ≈ 10^{-7} s (energy scales from ≈ 100 meV to ≈ 30 neV). These wide ranges of accessible distances and times support a very diverse scientific program, allowing researchers in materials science, chemistry, biology, and condensed matter physics to investigate materials such as polymers, metals, ceramics, magnetic materials, porous media, fluids and gels, and biological molecules.

In the most recent Call for Proposals (call 30), 236 proposals requested CHRNS instruments, and 124 of these proposals received beam time. Of the 1175 days requested for the CHRNS instruments, 497 were awarded. Corresponding numbers for all instruments were 340 proposals received, 193 proposals approved, 1776 days requested, and 834 days awarded. Roughly half of the users of neutron scattering techniques at the NCNR use CHRNS-funded instruments, and more than one third of NCNR publications (see the "Publications" section on p. 62), over the current one-year period, are based on research performed using these instruments. This reports contains several highlights of CHRNS publications. See the labeled highlights in the table of contents.

Scientific Support Services

CHRNS offers scientific support to our users in two critical areas: sample environment and chemical laboratories. The CHRNS Sample Environment team provides users with the equipment and training required to make measurements under special conditions of temperature, pressure, magnetic field, and fluid flow. This year the team commissioned a new ^{3}He system that will be use with our 10 T magnet and our 70 mm ILL cryostats, thus increasing our low temperature

FIGURE 1: Participants in the NCNR 2013 Summer School "Methods and Applications of Neutron Spectroscopy and SANS."

capabilities. In order to improve our high temperature capabilities, the team commissioned two new high temperature CCR's. In addition, other old and less reliable pieces of equipment have been replaced throughout the year.

The laboratory staff continues work on developing training materials, helping users with their sample preparations, and keeping all our users laboratories in top shape. With nine laboratories dedicated to our users, the staff ensures that users have the tools and supplies they need for a successful experiment.

Education and Outreach

This year the Center for High Resolution Neutron Scattering sponsored a variety of educational programs and activities tailored to specific age groups and professions. The annual summer school, held on June 17-20, 2013 was entitled "Methods and Applications of Neutron Spectroscopy and SANS". Forty graduate and postdoctoral students from 23 universities participated in the school. Lectures, research seminars and were highlighted for a wide variety of neutron measurement techniques. The guest lecturer was Prof. Stephen Wilson from Boston College. The evaluations were excellent and student feedback was very positive.

As part of its expanding education and outreach effort, CHRNS offers to university-based research groups with BTAC-approved experimental proposals the opportunity to request travel support for an additional graduate student to participate in the experiment. This support is intended to enable prospective thesis students, for example, to acquire first-hand experience with a technique that they may later use in their own research. Announcements of this program are sent to all of the university groups whose experimental proposals receive beam time from the BTAC. Recipients of the announcement are encouraged to consider graduate students from under-represented groups for this opportunity. The program is also advertised on the NCNR's website at http://www.ncnr.nist.gov/outreach.html.

As in previous years, CHRNS participated in NIST's Summer Undergraduate Research Fellowship (SURF) program. In 2013 CHRNS hosted 13 SURF students. The students worked on a variety of projects including etch damage in magnetic thin-film sensors, dynamics of methanol/water mixtures, gas adsorption in metal-organic frameworks, pressure dependence of coordinated polymers, enhanced fitting engines for diffraction data refinement, and conceptual design of a new high-power research reactor. They presented their work at the NIST SURF colloquium in early August 2013.

The Summer High school Intern Program (SHIP) has been a very successful program with seven students participating this year. The students participated on research projects such as web-based data fitting, modeling off-specular x-ray scattering, minimizing roughness in permalloy thin films, and determining the glass transition temperature in confined polymer films. The results of the students' summer investigations were highlighted in a NIST-wide poster session in early August, as well as in an oral symposium at the NCNR.

FIGURE 2: The 2013 SURF students, NCNR director Rob Dimeo (left), CHRNS director Dan Neumann (second from left), and chief of reactor operations Sean O'Kelly (right).

The NCNR initiated a Research Experiences for Teachers (RET) program in the summer of 2010. Wootton High School teacher Michael Thompson (Montgomery County, MD) was selected for the program for the summer of 2012 and 2013. He collaborated with NCNR's Joe Dura and SURF student Benjamin Jones from the University of Maryland on a project involving thin carbon films for battery and fuel cell applications.

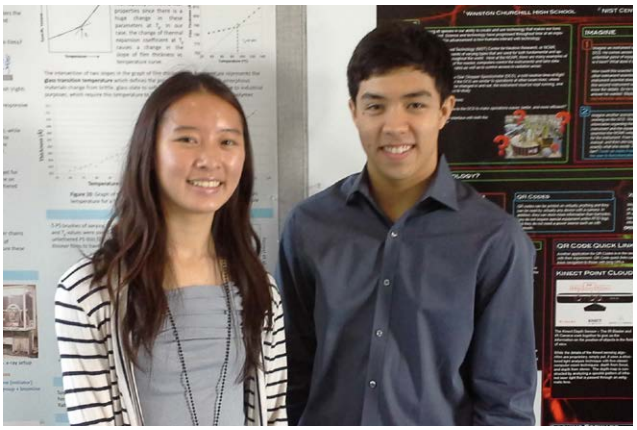

FIGURE 3: Two of the NCNR's SHIP students, Amy Lin and Mark Richardson from Winston Churchill High School (Potomac, MD) present their results at a NIST-wide symposium.

The annual Summer Institute for Middle School Science Teachers brings middle school science teachers to NIST for two weeks in order to give them a better understanding of the scientific process. Each year, CHRNS hosts the teachers for a one-day introduction to neutron scattering with a presentation that describes how neutrons are produced and how they are used to improve our understanding of materials at the atomic scale. Having toured the neutron guide hall, and having seen several neutron instruments, the teachers learn about the types of experiments performed at the NCNR. To bring home projects suitable for middle school students, they then learn how to grow crystals of "alum" (hydrated aluminum potassium sulfate). Throughout the day and at lunchtime, the teachers have the opportunity to interact with staff members.

Elementary, Middle, and High School Activities

As part of NIST's activities for the annual "Take Your Daughters and Sons to Work Day", CHRNS staff gave a presentation on what neutrons can do and offered a tour of the facility. The children, whose ages ranged from 12 years old to 15 years old, enjoyed watching the "Neutron Mouse Trap" (which demonstrates a "chain reaction" with mouse traps and ping pong balls).

22 tours for Middle School, High School, and University students were offered throughout the year.

"Adventures in Science" is a hands-on science program for middle school students with classes in physics, chemistry, computers, biology, astronomy, etc., taught by scientists, engineers, and technical professionals. Classes meet for about two hours on Saturday mornings from October through March.

The NCNR and CHRNS staff developed a program to help Boy Scout troops from around the NIST area earn a Nuclear Science Merit Badge.

2013 Awards

Shannon Watson and **Wangchun Chen** of the NCNR have been named the recipients of the 2013 **Sigma Xi Award for Outstanding Scientific Support** of NIST research scientists. This award recognizes their dedication in developing, producing, and delivering nuclear spin-polarized ^{3}He gas cells used for neutron beam measurements.

NCNR's **Kathryn Krycka** was presented with the **Young SANS Investigator Award** for her work on the magnetic morphology of nanoparticles during the 15th International Small-Angle Scattering Conference in Sydney, Australia.

David Mildner of the NCNR and an international group of co-workers received the **Dal Swaine Award** for the best paper in Coal and Hydrocarbon Source Rock Geochemistry, given by the Society for Organic Petrology. Their paper was titled "Pore size distribution and accessible pore size distribution in bituminous coals."

Kim Tomasi has been selected to receive the **NIST Colleague's Choice Award**. Kim is being recognized "For oversight in development, organization, and upkeep of 12 laboratories and the design and maintenance of the laboratory safety program." Kim Tomasi has also been selected to receive the organizational **Safety Award** as part of the NIST Biosafety Working Group. In particular they are being recognized "for their efforts in developing and promoting biosafety training and awareness for NIST staff." The Safety Award is given to recognize NIST employees and organizations for substantial contributions to improving safety at NIST.

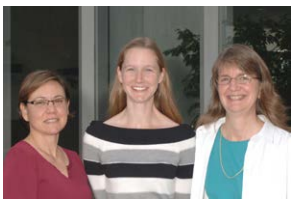

NCNR's **Yamali Hernandez**, Cindi Dennis (NIST MML), and NCNR's **Julie Borchers** received the **NIST Equal Employment Opportunity/ Diversity Award** "For extraordinary and voluntary effort into initiating and establishing the NIST Summer High School Internship Program (SHIP)."

NCNR's **Mike Dmitriou** received **first place** at the **Sigma Xi Post-doc Poster** Presentation for his poster entitled "The Effect of T_g Reduction on Chain Mobility in Confined Polystyrene Films."

NCNR's **Brian Kirby** received the **NIST Bronze Medal**. Brian is being recognized for "The elucidation of complex magnetic coupling in ferromagnetic, semiconducting multilayers using innovative polarized neutron reflectivity methods."

NCNR's **William Ratcliff, Jr.** received the **NIST Bronze Medal** for "His achievements in elucidating the magnetic and ferroelectric properties of $BiFeO_3$, the leading contender for new spintronics technologies."

NCNR's **Dan Dender**, with Bruce Benner and Mike Kelley (NIST MML), and Adrian Mitchell and Carol Wood (NIST OFRM) were awarded the **NIST Bronze Medal** "For improving the safety, efficiency, and effectiveness of the compressed gas program."

Aaron Eberle from ExxonMobil was recognized for "**Best Use of Small-Angle Neutron Scattering To an Industrial Application**" presented at the 15th International Small-Angle Scattering Conference in Sydney, Australia. Aaron was a post-doc at the NCNR and now leads the ExxonMobil program at the NCNR.

Norman Wagner, the Alvin B. and Julia O. Stiles Professor of Chemical Engineering at the University of Delaware, is the recipient of the 2013 **Shell Global Solutions Thomas Baron Award**. Prof. Wagner is being recognized for his excellence in colloidal suspension rheology fundamentals, developing new instrumentation, and translating these into breakthrough applications. This award recognizes an individual's recent outstanding scientific/technical accomplishment that has made a significant impact in the field of fluid-particle systems or in a related field with potential for cross-fertilization. Norm is a frequent NCNR user.

Tyrel McQueen, assistant professor of chemistry at Johns Hopkins University received the 2013 **ExxonMobil Solid-State Chemistry Faculty Fellowship**. The award is administered by the ACS Division of Inorganic Chemistry, recognizing significant contributions to solid-state chemistry by an untenured faculty member at a U.S. institution. McQueen is a faculty member in Chemistry, as well as the Institute for Quantum Matter in Physics at Johns Hopkins University. His interdisciplinary research focuses on the discovery of new materials with unique physical properties, particularly those with strong electron correlation effects. Tyrel often uses the NCNR facilities for his work.

Kate Gurnon, a graduate student at the University of Delaware working with Prof. Norm Wagner won the **Reg Davies Best Poster Award** at the 2013 International Fine Particles Research Institute Annual Meeting held in Newark, DE. Her poster title was: "Microstructure-property Relationships for Novel Field-responsive Nanomaterials". Kate also won 1st prize in the graduate student poster competition at the 85th Annual Meeting of the Society of Rheology, for her poster entitled "Spatiotemporal structure evolution and metastable states in shear banding wormlike micelles probed using LAOS and small angle neutron scattering."

Simon Rogers, a post-doc working with Prof. Norm Wagner at the University of Delaware won **2nd prize** in the post-doc poster competition at the 85th Annual Meeting of the Society of Rheology, for his poster on "The sequencing of dynamic rheological measurements."

Publications: August 1, 2012 to July 31, 2013

Abriola, S.A., Bashir, J., Balagurov, A., Das, A., Edwards, L., Gnäupel-Herold, T., Goh, B., Ionita, I., Mikula, P., Ohms, C., Ridikas, D., Schneider, R.P., Sutiarso, S., Torok, G., Venter, A., Wimpory, R., "Development and Application of Residual Stress Measurement using Neutron Beams," IAEA Tech. Rep. Series, edited by D.Ridikas, (International Atomic Energy Agency, Vienna, 2013), in press.

Abutaleb, M.O., Pushin, D.A., Huber, M.G., Majkrzak, C.F., Arif, M., Cory, D.G., "Design of Remnant Magnetization FeCoV Films as Compact, Heatless Neutron Spin Rotators," Appl. Phys. Lett. **101**(18), 182404 (2012).

Anderson, D.L., Cunningham, W.C., "Analysis of FDA In-House Food Reference Materials with Anticoincidence INAA," J. Radioanal. Nucl. Chem. **296**(1), 175 (2013).

Anderson, D.L., "Anticoincidence INAA Capabilities for Analysis of FDA Total Diet Study Seafoods," J. Radioanal. Nucl. Chem. **296**(1), 187 (2013).

Anderson, D.L., "INAA Study of Hg, Se, As, and Br Irradiation Losses from L-cysteine Treated and Untreated Reference Materials," J. Radioanal. Nucl. Chem. **296**(1), 181 (2013).

Anderson, D.L., "Effect of L-cysteine on Drying and Neutron Irradiation Loss of Hg, Se, As, and Br from Fish Tissue," J. Food Compos. Anal. **28**(2), 88 (2012).

Anovitz, L.M., Cole, D.R., Rother, G., Allard, L.F., Jackson, A.J., Littrell, K.C., "Diagenetic Changes in Macro- to Nano-Scale Porosity in the St. Peter Sandstone: An (Ultra) Small Angle Neutron Scattering and Backscattered Electron Imaging Analysis," Geochim. Cosmochim. Ac. **102**, 280 (2013). [CHRNS]

Anovitz, L.M., Cole, D.R., Faulder, D.D., Sheets, J., Wang, H.-W., Rother, G., Wasbrough, M., Hjelm, R., Hartl, M., Pipich, V., Fu, Z., "Analysis of Multiscale Porosity at the Coso Geothermal Field," in "Proceedings, Thirty-Eighth Workshop on Geothermal Reservoir Engineering," (Stanford Geothermal Workshop, February 2013, Stanford, CA) **SGP-TR-198** (2013). [CHRNS]

Arenas, D.J., Jegorel, T., Knab, C., Gasparov, L.V., Martin, C., Pajerowski, D.M., Kohno, H., Lufaso, M.W., "Raman Spectroscopy Evidence of Inhomogeneous Disorder in the Bismuth-Oxygen Framework of $Bi_{25}InO_{39}$ and Other Sillenites," Phys. Rev. B **86**(14), 144116 (2012).

Armstrong, C.L., Toppozini, L., Dies, H., Faraone, A., Nagao, M., Rheinstädter, M.C., "Incoherent Neutron Spin-Echo Spectroscopy as an Option to Study Long-Range Lipid Diffusion," ISRN Biophys. **2013**, 439758 (2013). [CHRNS]

Arnold, D.E., Bohor, B.F., Neff, H., Feinman, G.M., Williams, P.R., Dussubieux, L., Bishop, R., "The First Direct Evidence of Pre-Columbian Sources of Palygorskite for Maya Blue," J. Archaeol. Sci. **39**(7), 2252 (2012).

Azuah, R.T., Diallo, S.O., Adams, M.A., Kirichek, O., Glyde, H.R., "Phonon-Roton Modes of Liquid ^{4}He Beyond the Roton in the Porous Medium MCM-41," Phys. Rev. B **88**(2), 024510 (2013).

Bae, T.-H., Hudson, M.R., Mason, J.A., Queen, W.L., Dutton, J.J., Sumida, K., Micklash, K.J., Kaye, S.S., Brown, C.M., Long, J.R., "Evaluation of Cation-Exchanged Zeolite Adsorbents for Post-Combustion Carbon Dioxide Capture," Energ. Environ. Sci. **6**(1), 128 (2013).

Bao, W., Li, G.-N., Huang, Q.-Z., Chen, G.-F., He, J.-B., Wang, D.-M., Green, M.A., Qiu, Y.-M., Luo, J.-L., Wu, M.-M., "Superconductivity Tuned by the Iron Vacancy Order in $K_xFe_{2-y}Se_2$," Chinese Phys. Lett. **30**(2), 027402 (2013).

Bass, C.D., Beise, E.J., Breuer, H., Heimbach, C.R., Langford, T.J., Nico, J.S., "Characterization of a ^{6}Li-Loaded Liquid Organic Scintillator for Fast Neutron Spectrometry and Thermal Neutron Detection," Appl. Radiat. Isotopes **77**, 130 (2013).

Bazilevskaya, E., Lebedeva, M., Pavich, M., Rother, G., Parkinson, D.Y., Cole, D., Brantley, S.L., "Where Fast Weathering Creates Thin Regolith and Slow Weathering Creates Thick Regolith," Earth Surf. Proc. Land. **38**(8), 847 (2013). [CHRNS]

Bentley, P.M., Kennedy, S.J., Andersen, K.H., Rodríguez, D.M., Mildner, D.F.R., "Correction of Optical Aberrations in Elliptic Neutron Guides," Nucl. Instrum. Meth. A **693**, 268 (2012).

Bertrand, C.E., Chiang, W.-S., Tyagi, M., Chen, S.-H., "Low-Temperature Water Dynamics in an Aqueous Methanol Solution," J. Chem. Phys. **139**(1), 014505 (2013). [CHRNS]

Bertrand, C.E., Zhang, Y., Chen, S.-H., "Deeply-Cooled Water Under Strong Confinement: Neutron Scattering Investigations and the Liquid-Liquid Critical Point Hypothesis," Phys. Chem. Chem. Phys. **15**(3), 721 (2013). [CHRNS]

Bingham, P., Polsky, Y., Anovitz, L., "Neutron Imaging for Geothermal Energy Systems," in "Image Processing: Machine Vision Applications VI," edited by Bingham, P.R., Lam, E.Y., (Proc. of SPIE-IS&T Electronic Imaging) **8661**, 86610K (2013).

Bishop, R.L., Sears, E.L., Blackman, M.J., "Cerámicas en el borde occidental de las Tierras Baja Maya," in "Arqueología de la costa de Campeche: La época prehispánica," edited by Cobos, R., (Ediciones de la Universidad Autónoma de Yucatán, México) 187 (2012).

Blachowski, A., Ruebenbauer, K., Zajdel, P., Rodriguez, E.E., Green, M.A., "Mössbauer Study of the '11' Iron-based Superconductors Parent Compound $Fe_{1+x}Te$," J. Phys.: Condens. Matter **24**, 386006 (2012).

Blackburn, J.L., Engtrakul, C., Bult, J.B., Hurst, K., Zhao, Y., Xu, Q., Parilla, P.A., Simpson, L.J., Rocha, J.-D. R., Hudson, M.R., Brown, C.M., Gennett, T., "Spectroscopic Identification of Hydrogen Spillover Species in Ruthenium-modified High Surface Area Carbons by Diffuse Reflectance Infrared Fourier Transform Spectroscopy," J. Phys. Chem. C **116**(51), 26744 (2012).

Boggara, M.B., Mihailescu, M., Krishnamoorti, R., "Structural Association of Nonsteroidal Anti-Inflammatory Drugs with Lipid Membranes," J. Am. Chem. Soc. **134**(48), 19669 (2012).

Budvytyte, R., Valincius, G., Niaura, G., Voiciuk, V., Mickevicius, M., Chapman, H., Goh, H.-Z., Shekhar, P., Heinrich, F., Shenoy, S., Lösche, M., Vanderah, D.J., "Structure and Properties of Tethered Bilayer Lipid Membranes with Unsaturated Anchor Molecules," Langmuir **29**(27), 8645 (2013).

Budvytyte, R., Mickevicius, M., Vanderah, D.J., Heinrich, F., Valincius, G., "Modification of Tethered Bilayers by Phospholipid Exchange with Vesicles," Langmuir **29**(13), 4320 (2013).

Buss, H.L., Brantley, S.L., Scatena, F.N., Bazilievskaya, E.A., Blum, A., Schulz, M., Jiménez, R., White, A.F., Rother, G., Cole, D., "Probing the Deep Critical Zone Beneath the Luquillo Experimental Forest, Puerto Rico," Earth Surf. Proc. Land., in press. [CHRNS]

Cappelletti, R.L., editor, "2012 NIST Center for Neutron Research Accomplishments and Opportunities," **NIST SP 1143** (2012).

Castañeda, C.A., Kashyap, T.R., Nakasone, M.A., Krueger, S., Fushman, D., "Unique Structural, Dynamical, and Functional Properties of K11-Linked Polyubiquitin Chains," Structure **21**(7), 1168 (2013). [CHRNS]

Chatterjee, T., Nakatani, A.I., Adden, R., Brackhagen, M., Redwine, D., Shen, H., Li, Y., Wilson, T., Sammler, R.L., "Structure and Properties of Aqueous Methylcellulose Gels by Small-Angle Neutron Scattering," Biomacromolecules **13**(10), 3355 (2012). [CHRNS]

Chen, S.-H., Wang, Z., Kolesnikov, A.I., Zhang, Y., Liu, K.-H., "Search for the First-Order Liquid-to-Liquid Phase Transition in Low-Temperature Confined Water by Neutron Scattering," in "AIP Conference Proceedings," edited by Takuyama, M., Oppenheim, I., (4th International Symposium on Slow Dynamics in Complex Systems, November 2012, Sendai) **1518**, 77 (2013). [CHRNS]

Chen, W. C., Erwin, R., Watson, S.M., "Neutron Path Length Correction of a ^{3}He Spin Filter," in "Physics Procedia," edited by Otto F., (Physics Procedia, June 2012, Paris) **42**, 163 (2013). [CHRNS]

Chen, X., Zhang, Y., Wang, Y., Zhou, W., Knight, D.A., Yisgedu, T.B., Huang, Z., Lingam, H.K., Billet, B., Udovic, T.J., Brown, G.M., Shore, S.G., Wolverton, C., Zhao, J.-C., "Structure Determination of an Amorphous Compound AlB_4H_{11}," Chem. Sci. **3**(11), 3183 (2012).

Cheng, C.L., Kang, M., Perfect, E., Voisin, S., Horita, J., Bilheux, H.Z., Warren, J.M., Jacobson, D.L., Hussey, D.S., "Average Soil Water Retention Curves Measured by Neutron Radiography," Soil Sci. Soc. Am. J. **76**(4), 1184 (2012).

Cho, K.T., Mench, M.M., "Investigation of the Role of the Micro-Porous Layer in Polymer Electrolyte Fuel Cells with Hydrogen Deuterium Contrast Neutron Radiography," Phys. Chem. Chem. Phys. **14**(12), 4296 (2012).

Choi, D., Moon, J.H., Kim, H., Sung, B.J., Kim, M.W., Tae, G.Y., Satija, S.K., Akgun, B., Yu, C.-J., Lee, H.W., Lee, D.R., Henderson, J.M., Kwong, J.W., Lam, K.L., Lee, K.Y.C., Shin, K., "Insertion Mechanism of Cell-penetrating Peptides into Supported Phospholipid Membranes Revealed by X-ray and Neutron Reflection," Soft Matter **8**(32), 8294 (2012).

Choi, J., Hore, M.J.A., Meth, J.S., Clarke, N., Winey, K.I., Composto, R.J., "Universal Scaling of Polymer Diffusion in Nanocomposites," ACS Macro Letters **6**, 485 (2013). [CHRNS]

Choi, Y.J., Lee, N., Sharma, P.A., Kim, S.B., Vajk, O.P., Lynn, J.W., Oh, Y.S., Cheong, S.-W., "Giant Magnetic Fluctuations at the Critical Endpoint in Insulating $HoMnO_3$," Phys. Rev. Lett. **110**(15), 157202 (2013).

Chu, L., Wang, C., Bordet, P., Colin, C.V., Pairis, S., Na, Y., Yan, J., Huang, Q., "The Effect of Zn Vacancies on the Physical Properties of Antiperovskite Compounds Mn_3Zn_xN," Scripta Mater. **68**(12), 968 (2013).

Chung, J.-H., Lee, K.H., Song, Y.-S., Suzuki, T., Katsufuji, T., "Low Temperature Structural Instability of Tetragonal Spinel Mn_3O_4," J. Phys. Soc. Jpn. **82**, 034707 (2013).

Chupp, T.E., Cooper, R. L., Coulter, K.P., Freedman, S.J., Fujikawa, B.K., García, A., Jones, G.L., Mumm, H.P., Nico, J.S., Thompson, A.K., Trull, C.A., Wietfeldt, F.E., Wilkerson, J.F., "Search for a *T*-odd, *P*-even Triple Correlation in Neutron Decay," Phys. Rev. C **86**(3), 035505 (2012).

Chupp, T.E., Cooper, R.L., Coulter, K.P., Freedman, S.J., Fujikawa, B.K., Jones, G.L., García, A., Mumm, H.P., Nico, J.S., Thompson, A.K., Trull, C., Wietfeldt, F.E., Wilkerson, J.F., "Time Reversal and the Neutron Results of the emiT II Experiment," Hyperfine Interact. **214**(1-3), 97 (2013).

Clapham, L., Babbar, V., Gnaüpel-Herold, T.H., Batisse, R., Zarea, M., "Neutron Diffraction Studies of Residual Stresses around Gouges and Gouged Dents," in "Pipeline Integrity Management," edited by American Society of Mechanical Engineers, (9th International Pipeline Conference, September 2012, Calgary, Alberta, Canada) **2**, 747 (2012).

Clarkson, C.R., Solano, N., Bustin, R.M., Bustin, A.M.M., Chalmers, G.R.L., He, L., Melnichenko, Y.B., Radliński, A.P., Blach, T.P., "Pore Structure Characterization of North American Shale Gas Reservoirs using USANS/SANS, Gas Adsorption, and Mercury Intrusion," Fuel **103**, 606 (2013). [CHRNS]

Cockayne, E., Levin, I., Wu, H., Llobet, A., "Magnetic Structure of Bixbyite α-Mn_2O_3: A combined DFT+*U* and Neutron Diffraction Study," Phys. Rev. B **87**(18), 184413 (2013).

Colmenero, J. Arbe, A., "Recent Progress on Polymer Dynamics by Neutron Scattering: From Simple Polymers to Complex Materials", J. Polymer Science B: Polymer Physics **51**, 87 (2013).

Cooper, R.L., Alarcon, R., Bales, M.J., Bass, C.D., Beise, E.J., Breuer, H., Byrne, J., Chupp, T.E., Coakley, K.J., Dewey, M.S., Fu, C., Gentile, T.R., Mumm, H.P., Nico, J.S., O'Neill, B., Pulliam, K., Thompson, A.K., Wietfeldt, F.E., "A Gamma- and X-ray Detector for Cryogenic, High Magnetic Field Applications," Nucl. Instrum. Meth. A **691**, 64 (2012).

Crawford, M.K., Smalley, R.J., Cohen, G., Hogan, B., Wood, B., Kumar, S.K., Melnichenko, Y.B., He, L., Guise, W., Hammouda, B., "Chain Conformation in Polymer Nanocomposites with Uniformly Dispersed Nanoparticles," Phys. Rev. Lett. **110**(19), 196001 (2013).

Cruz, J., Mihailescu, M., Wiedman, G., Herman, K., Searson, P.C., Wimley, W.C., Hristova, K., "A Membrane-Translocating Peptide Penetrates into Bilayers without Significant Bilayer Perturbations," Biophys. J. **104**(11), 2419 (2013).

Curtis, J.E., Nanda, H., Khodadadi, S., Cicerone, M., Lee, H.J., McAuley, A., Krueger, S., "Small-Angle Neutron Scattering Study of Protein Crowding in Liquid and Solid Phases: Lysozyme in Aqueous Solution, Frozen Solution, and Carbohydrate Powders," J. Phys. Chem. B **116**, 9653 (2012). [CHRNS]

Curtis, J.E., McAuley, A., Nanda, H., Krueger, S., "Protein Structure and Interactions in the Solid State Studied by Small-Angle Neutron Scattering," Faraday Discuss. **158**, 285 (2012). [CHRNS]

Das, P., Baumbach, R.E., Huang, K., Maple, M.B., Zhao, Y., Helton, J.S., Lynn, J.W., Bauer, E.D., Janoschek, M., "Absence of a Static In-plane Magnetic Moment in the 'Hidden-Order' Phase of URu_2Si_2," New J. Phys. **15**, 053031 (2013).

Das, P., Densmore, J.M., Rastovski, C., Schlesinger, K.J., Laver, M., Dewhurst, C.D., Littrell, K., Bud'ko, S.L., Canfield, P.C., Eskildsen, M.R., "Field Dependence of the Superconducting Basal Plane Anisotropy of $TmNi_2Bi_2C$,"Phys. Rev. B **86**(14), 144501 (2012).

Diamond, D.J., Hanson, A.L., Baek, J-S., Brown, N.R., Cuadra, A., Cheng, L.-Y., O'Kelly, D.S., Williams, R.E., Rowe, J.M., "Progress with the Conversion of the NIST Research Reactor," in "Proceedings of RERTR 2012," (RERTR 2012 - 34th International Meeting on Reduced Enrichment for Research and Test Reactors, September 2012, Warsaw, Poland) (2012).

Dimeo, R., Ibberson, R., O'Kelly, S., Neumann, D., Cappelletti, R., Gehring, P., "The Expansion of the NIST Center for Neutron Research," Neutron News **24**(1), 29 (2013).

Duan, X., Yu, J., Cai, J., He, Y., Wu, C., Zhou, W., Yildirim, T., Zhang, Z., Xiang, S., O'Keeffe, M., Chen, B., Qian, G., "A Microporous Metal-Organic Framework of a Rare Sty Topology for High CH_4 Storage at Room Temperature," Chem. Commun. **49**(20), 2043 (2013).

Dumont, M.F., Risset, O.N., Knowles, E.S., Yamamoto, T., Pajerowski, D.M., Meisel, M.W., Talham, D.R., "Synthesis and Size Control of Iron(II) Hexacyanochromate(III) Nanoparticles and the Effect of Particle Size on Linkage Isomerism," Inorg. Chem. **52**(8), 4494 (2013).

Dun, Z.L., Choi, E.S., Zhou, H.D., Hallas, A.M., Silverstein, H.J., Qiu, Y., Copley, J.R.D., Gardner, J.S., Wiebe, C.R., "$Yb_2Sn_2O_7$: a Magnetic Coulomb Liquid at a Quantum Critical Point," Phys. Rev. B **87**(13), 134408 (2013). [CHRNS]

Eastman, S.A., Kim, S., Page, K.A., Rowe, B.W., Kang, S., DeCaluwe, S.C., Dura, J.A., Soles, C.L., Yager, K.G., "Effect of Confinement on Structure, Water Solubility, and Water Transport in Nafion Thin Films," Macromolecules **45**(19), 7920 (2012).

Eberbeck, D., Dennis, C.L., Huls, N.F., Krycka, K.L., Grüttnerr, C., Westphal, F., "Multicore Magnetic Nanoparticles for Magnetic Particle Imaging," IEEE T. Magn. **49**(1), 269 (2013). [CHRNS]

Elliott, L.C.C., Jing, B., Akgun, B., Zhu, Y., Bohn, P.W., Fullerton-Shirey, S.K., "Loading and Distribution of a Model Small Molecule Drug in Poly(*N*- isopropylacrylamide) Brushes: a Neutron Reflectometry and AFM Study," Langmuir **29**(10), 3259 (2013).

Enoki, M., Fujita, M., Nishizaki, T., Iikubo, S., Singh, D.K., Chang, S., Tranquada, J.M., Yamada, K., "Spin-Stripe Density Varies Linearly with the Hole Content in Single-Layer $Bi_{2+x}Sr_{2-x}CuO_{6+y}$ Cuprate Superconductors," Phys. Rev. Lett. **110**(1), 017004 (2013). [CHRNS]

Eriksson, S.M., Mackey, E.A., Lindstrom, R.M., Lamaze, G.P., Grogan, K.P., Brady, D.E., "Delayed-Neutron Activation Analysis at NIST," J. Radioanal. Nucl. Chem., in press.

Fairweather, J.D., Spernjak, D., Weber, A.Z., Harvey, D., Wessel, S., Hussey, D.S., Jacobson, D.L., Artyushkova, K., Mukundan, R., Borup, R.L., "Effects of Cathode Corrosion on Through-Plane Water Transport in Proton Exchange Membrane Fuel Cells," J. Electrochem. Soc. **160**(9), F980 (2013).

Ferguson, P.P., Fleischauer, M.D., LaForge, J.M., Todd, A.D.W., Li, P., Dahn, J.R., "Studies of CoSn Grains in the Carbon Matrix Structure of Nanostructured Tin-Cobalt-Carbon," J. Alloy Compd. **541**, 168 (2012). [CHRNS]

FitzGerald, P.A., McDonald, D.M., Warr, G.G., "The Effect of Degree of Polymerization on Intra- and Interchain Micellization of a Tail-Type Cationic Polysoap," Soft Matter **9**, 2711 (2013). [CHRNS]

FitzGerald, P.A., Warr, G.G., "Structure of Polymerizable Surfactant Micelles: Insights from Neutron Scattering," Adv. Colloid. Interfac. Sci. **179-182**, 14 (2012). [CHRNS]

Foias, A.E., Bishop, R.L., "Ceramics, Production, and Exchange in the Petexbatun Region: The Economic Parameters of the Classic Maya Collapse," in "Vanderbilt Institute of Mesoamerican Archaeology Series," (Vanderbilt University Press) **7** (2013).

Fournier, P., Blackman, M.J., Bishop, R.L., "La arqueología histórica, etnoarqueología, y arqueometría aplicadas al estudio de las lozas vidriadas en Mexico: aproximaciones diacrónicas," in "Haciendo Arqueología: Teoría, métodos y técnicas," edited by Ladron, S. de Guevara, L. Budar, R. Lunagomez, (Universidad Veracruzana, Xalapa, Veracruz, Mexico) 131 (2012).

Fratini, E., Faraone, A., Ridi, F., Chen, S.-H., Baglioni, P., "Hydration Water Dynamics in Tricalcium Silicate Pastes by Time-Resolved Incoherent Elastic Neutron Scattering," J. Phys. Chem. C **117**(14), 7358 (2013).

Fritsch, K., Ross, K.A., Qiu, Y., Copley, J.R.D., Guidi, T., Bewley, R.I., Dabkowska, H.A., Gaulin, B.D., "Antiferromagnetic Spin Ice Correlations at (½,½,½) in the Ground State of the Pyrochlore Magnet $Tb_2Ti_2O_7$," Phys. Rev. B **87**(9), 094410 (2013). [CHRNS]

Fritsch, K., Yamani, Z., Chang, S., Qiu, Y., Copley, J.R.D., Ramazanoglu, M., Dabkowska, H.A., Gaulin, B.D., "Magnetic Order and Fluctuations in the Presence of Quenched Disorder in the Kagome Staircase System $(Co_{1-x}Mg_x)_3V_2O_8$," Phys. Rev. B **86**(17), 174421 (2012). [CHRNS]

Fu, R.S., Pasaogullari, U., Shiomi, T., Tabuchi, Y., Hussey, D.S., Jacobson, D.L., "High-Resolution Neutron Radiography of Through-Plane Liquid Water Distribution in Polymer Electrolyte Membrane and Gas Diffusion Layer," J. Electrochem. Soc. **159**(9), F545 (2012).

Fujita, S., Kamazawa, K., Yamamoto, S., Tyagi, M., Araki, T., Sugiyama, J., Hasegawa, N., Kawasumi, M., "Proton Conductivity under Dry Conditions for Mesoporous Silica with Highly Dense Sulfonic Acid Groups," J. Phys. Chem. C **117**(17), 8727 (2013). [CHRNS]

García Sakai, V., Khodadadi, S., Cicerone, M.T., Curtis, J. E., Sokolov, A.P., Roh, J.H., "Solvent Effects on Protein Fast Dynamics: Implications for Biopreservation," Soft Matter **9**(22), 5336 (2013). [CHRNS]

García, A., Chupp, T.E., Cooper, R.L., Coulter, K.P., Freedman, S.J., Fujikawa, B.K., Jones, G.L., Mumm, H.P., Nico, J.S., Thompson, A.K., Trull, C.A., Wietfeldt, F.E., Wilkerson, J.F., "Search for T Violation in Neutron Decay: the emiT Experiment," Lett. Nuovo Cimento **35C**(4), 68 (2012).

Gaultois, M.W., Barton, P.T., Birkel, C.S., Misch, L.M., Rodriguez, E.E., Stucky, G.D., Seshadri, R., "Structural Disorder, Magnetism, and Electrical and Thermoelectric Properties of Pyrochlore $Nd_2Ru_2O_7$," J. Phys.: Condens. Matter **25**(18), 186004 (2013).

Geier, S.J., Mason, J.A., Bloch, E.D., Queen, W.L., Hudson, M.R., Brown, C.M., Long, J.R., "Selective Adsorption of Ethylene over Ethane and Propylene over Propane in the Metal-Organic Frameworks M_2 (dobdc) (M = Mg, Mn, Fe, Co, Ni, Zn)," Chem. Sci. **4**(5), 2054 (2013).

Gentile, T.R., Hayden, M.E., Nacher, P.J., Petukhov, A.K., Saam, B., Walker, T.G., "Comment on 'Enhanced Polarization and Mechanisms in Optically Pumped Hyperpolarized ^{3}He in the Presence of ^{4}He,'" Phys. Rev. A **88**(1), 017401 (2013).

Gericke, A., Leslie, N.R., Lösche, M., Ross, A.H., "PtdIns(4,5)P_2-Mediated Cell Signaling: Emerging Principles and PTEN as a Paradigm for Regulatory Mechanism," in "Advances in Experimental Medicine and Biology," edited by Lambris, J.D., in press.

Gin, P., Jiang, N., Liang, C., Taniguchi, T., Akgun, B., Satija, S.K., Endoh, M.K., Koga, T., "Revealed Architectures of Adsorbed Polymer Chains at Solid-Polymer Melt Interfaces," Phys. Rev. Lett. **109**(26), 265501 (2012).

Glassman, M.J., Olsen, B.D., "Structure and Mechanical Response of Protein Hydrogels Reinforced by Block Copolymer Self-Assembly," Soft Matter, in press.

Gnäupel-Herold, T.H., Iadicola, M.A., Creuziger, A.A., Foecke, T., Hu, L., "Interpretation of Diffraction Data from In-situ Stress Measurements during Biaxial Sheet Metal Forming," Mater. Sci. Forum, in press.

Gnäupel-Herold, T.H., Green, D.E., Foecke, T.J., Iadicola, M.A., "Through-Thickness Stresses in Automotive Sheet Metal after Plane Strain Channel Draw," Mater. Sci. Forum, in press.

Gorbachev, V.V., Cleveland, B.T., Gavrin, V.N., Ibragimova, T.V., Kalikhov, A.V., Nico, J.S., Veretenkin, E.P.V., "Ga Source Experiment for Detection of Short Baseline Neutrino Oscillations," J. Phys.: Conf. Ser. **375**(4), 042068 (2012).

Granado, E., Lynn, J.W., Jardim, R.F., Torikachvili, M.S., "Two-Dimensional Magnetic Correlations and Partial Long-Range Order in Geometrically Frustrated Sr_2YRuO_6," Phys. Rev. Lett. **110**(1), 017202 (2013).

Gupta, K., Curtis, J.E., Krueger, S., Hwang, Y., Cherepanov, P., Bushman, F.D., Van Duyne, G.D., "Solution Conformations of Prototype Foamy Virus Integrase and its Stable Synaptic Complex with U5 Viral DNA," Structure **20**(11), 1918 (2012). [CHRNS]

Guralnick, B., Kirby, B.J., Majkrzak, C.F., Mackay, M.E., "Morphological Characterization of Plastic Solar Cells using Polarized Neutron Reflectivity," Appl. Phys. Lett. **102**(8), 083305 (2013).

Hallas, A.M., Paddison, J.A.M., Silverstein, H.J., Goodwin, A.L., Stewart, J.R., Wildes, A.R., Cheng, J.G., Zhou, J.S., Goodenough, J.B., Choi, E.S., Ehlers, G., Gardner, J.S., Wiebe, C.R., Zhou, H.D., "Statics and Dynamics of the Highly Correlated Spin Ice, $Ho_2Ge_2O_7$," Phys. Rev. B **86**(13), 134431 (2012).

Hammouda, B., "Temperature Effect on the Nanostructure of SDS Micelles in Water," J. Res. Natl. Inst. Stan. Tech. **118**, 151 (2013). [CHRNS]

Hammouda, B., Mildner, D.F.R., Brûlet, A., Desert, S., "Insight into Neutron Focusing: the Out-of-Focus Condition," J. Appl. Crystallogr., in press. [CHRNS]

Han, T.-H., Helton, J.S., Chu, S., Nocera, D.G., Rodriguez-Rivera, J.A., Broholm, C., Lee, Y.S., "Fractionalized Excitations in the Spin-Liquid State of a Kagome-Lattice Antiferromagnet," Nature **492**, 406 (2012). [CHRNS]

Hansen, F., Peters, G.H., Taub, H., Miskowiec, A., "Diffusion of Water and Selected Atoms in DMPC Lipid Bilayer Membranes," J. Chem. Phys. **137**(20), 204910 (2012). [CHRNS]

Hardy, G.J., Nayak, R., Alam, S.M., Shapter, J.G., Heinrich, F., Zauscher, S., "Biomimetic Supported Lipid Bilayers with High Cholesterol Content Formed by α-helical Peptide-induced Vesicle Fusion," J. Mater. Chem. **22**, 19506 (2012).

Harriger, L.W., Liu, M., Luo, H., Ewings, R.A., Frost, C.D., Perring, T.G., Dai, P., "Temperature Dependence of the Paramagnetic Spin Excitations in $BaFe_2As_2$," Phys. Rev. B **86**(14), 140403 (2012).

Hayes, D.G., Alkhatib, M.H., Gomez del Rio, J., Urban, V.S., "Physicochemical Characterization of Water-in-oil Microemulsions formed by a Binary 1,3-dioxolane Alkyl Ethoxylate/Aerosol-OT Surfactant System," Colloids Surf., A **417**, 99 (2013). [CHRNS]

Hayre, N.R., Ross, K.A., Applegate, R., Lin, T., Singh, R.R.P., Gaulin, B.D., Gingras, M.J.P., "Thermodynamic Properties of $Yb_2Ti_2O_7$ Pyrochlore as a Function of Temperature and Magnetic Field: Validation of a Quantum Spin Ice Exchange Hamiltonian," Phys. Rev. B **87**(18), 184423 (2013).

He, C., Grutter, A.J., Gu, M., Browning, N.D., Takamura, Y., Kirby, B.J., Borchers, J.A., Kim, J.W., Fitzsimmons, M.R., Zhai, X., Mehta, V.V., Wong, F.J., Suzuki, Y., "Interfacial Ferromagnetism and Exchange Bias in $CaRuO_3$/$CamnO_3$ Superlattices," Phys. Rev. Lett. **109**(19), 197202 (2012).

He, T., Wu, H., Chen, J., Zhou, W., Wu, G., Xiong, Z., Zhang, T., Chen, P., "Alkali and Alkaline-Earth Metal Borohydride Hydrazinates: Synthesis, Structures and Dehydrogenation," Phys. Chem. Chem. Phys. **15**(25), 10487 (2013).

He, Y., Xiang, S., Zhang, Z., Xiong, S., Wu, C., Zhou, W., Yildirim, T., Krishna, R., Chen, B., "A Microporous Metal-Organic Framework Assembled from an Aromatic Tetracarboxylate for H_2 Purification," J. Mater. Chem. A **1**(7), 2543 (2013).

He, Y., Zhou, W., Krishna, R., Chen, B., "Microporous Metal-Organic Frameworks for Storage and Separation of Small Hydrocarbons," Chem. Commun. **48**(97), 11813 (2012).

He, Y., Zhou, W., Yildirim, T., Chen, B., "A Series of Metal-Organic Frameworks with High Methane Uptake and an Empirical Equation for Predicting Methane Storage Capacity," Energy Environ. Sci., in press.

Heeger, K.M., Tobin, M.N., Littlejohn, B.R., Mumm, H.P., "Experimental Parameters for a Reactor Antineutrino Experiment at Very Short Baselines," Phys. Rev. D **87**(7), 073008 (2013).

Heinen, J.M., Blom, A.C.M., Hawkett, B.S., Warr, G.G., "Phase Behavior of Amphiphilic Diblock Co-oligomers with Nonionic and Ionic Hydrophilic Groups," J. Phys. Chem. B **117**(10), 3005 (2013).

Herm, Z.R., Wiers, B.M., Mason, J.A., van Baten, J.M., Hudson, M.R., Zajdel, P., Brown, C.M., Masciocchi, N., Krishna, R., Long, J.R., "Separation of Hexane Isomers in a Metal-Organic Framework with Triangular Channels," Science **340**, 960 (2013).

Herman, T.K., Parks, S.C., Scherschligt, J., "Thermal Equilibration of Samples for Neutron Scattering," J. Appl. Crystallogr. **46**, 279 (2013). [CHRNS]

Hirai, D., Bremholm, M., Allred, J.M., Krizan, J., Schoop, L.M., Huang, Q., Tao, J., Cava, R.J., "Spontaneous Formation of Zigzag Chains at the Metal-Insulator Transition in the β-Pyrochlore CsW_2P_6," Phys. Rev. Lett. **110**(16), 166402 (2013).

Hong, L., Glass, D.C., Nickels, J.D., Perticaroli, S., Yi, Z., Tyagi, M., O'Neill, H., Zhang, Q., Sokolov, A.P., Smith, J.C., "Elastic and Conformational Softness of a Globular Protein," Phys. Rev. Lett. **110**(2), 028104 (2013). [CHRNS]

Hong, T., Zhu, L.Y., Ke, X., Garlea, V.O., Qiu, Y., Nambu, Y., Yoshizawa, H., Zhu, M., Granroth, G.E., Savici, A.T., Gai, Z., Zhou, H.D., "Structural and Magnetic Properties in the Quantum S=½ Dimer System $Ba_3(Cr_{1-x}V_x)_2O_8$ with Site Disorder," Phys. Rev. B **87**(14), 144427 (2013). [CHRNS]

Hore, M.J.A., Composto, R.J., "Strategies for Dispersing, Assembling, and Orienting Nanorods in Polymers," Curr. Opin. Chem. Eng. **2**(1), 95 (2013).

Horkay, F., Basser, P.J., Hecht, A.-M., Geissler, E., "Hierarchy and Organization of Hyaluronic Acid in Physiological Salt Solutions," Polym. Mater. Sci. Eng. **107**, 277 (2012). [CHRNS]

Horkay, F., "Interactions of Cartilage Extracellular Matrix Macromolecules," J. Polym. Sci. B: Polym. Phys. **50**(24), 1699 (2012). [CHRNS]

Hou, H.-C., Kirby, B.J., Gao, K.Z., Lai, C.-H., "Characterizing Formation of Interfacial Domain Wall and Exchange Coupling Strength in Laminated Exchange Coupled Composites," Appl. Phys. Lett. **102**(16), 162408 (2013).

Hould, N., Haouas, M., Nikolakis, V., Taulelle, F., Lobo, R.F., "Mechanisms of Quick Zeolite Beta Crystallization," Chem. Mater. **24**(18), 3621 (2012). [CHRNS]

Huang, B., Zhang, Y., Shu, X., Liu, Y., Penumadu, D., Ye, X. P., "Neutron Scattering for Moisture Detection in Foamed Asphalt," J. Mater. Civil Eng. **25**(7), 932 (2013).

Hussey, D.S., Coakley, K.J., Baltic, E., Jacobson, D.L., "Improving Quantitative Neutron Radiography through Image Restoration," Nucl. Instrum. Meth. A, in press.

Hussey, D.S., Spernjak, D., Weber, A.Z., Mukundan, R., Fairweather, J., Brosha, E.L., Davey, J., Spendelow, J.S., Jacobson, D.L., Borup, R.L., "Accurate Measurement of the Through-Plane Water Content of Proton-Exchange Membranes using Neutron Radiography," J. Appl. Phys. **112**(10), 104906 (2012).

Iida, K., Lee, S.-H., Onimaru, T., Matsubayashi, K., Sato, T.J., "Determination of Spin Hamiltonian in the Ni_4 Magnetic Molecule," Phys. Rev. B **86**(6), 064422 (2012). [CHRNS]

Inceoglu, S., Young, N.P., Jackson, A.J., Kline, S.R., Costeux, S., Balsara, N.P., "Effect of Supercritical Carbon Dioxide on the Thermodynamics of Model Blends of Styrene-Acrylonitrile Copolymer-Poly(methyl methacrylate) Studied by Small-Angle Neutron Scattering," Macromolecules, in press. [CHRNS]

Jang, Y., Seo, J., Akgun, B., Satija, S., Char, K., "Molecular Weight Dependence on the Disintegration of Spin-Assisted Weak Polyelectrolyte Multilayer Films," Macromolecules **46**(11), 4580 (2013).

Janson, O., Chen, S., Tsirlin, A.A., Hoffmann, S., Sichelschmidt, J., Huang, Q., Zhang, Z.-J., Tang, M.-B., Zhao, J.-T., Kniep, R., Rosner, H., "Structure and Magnetism of $Cr_2[BP_3O_{12}]$: Towards the Quantum-Classical Crossover in a Spin-3/2 Alternating Chain," Phys. Rev. B **87**(6), 064417 (2013).

Jiang, P., Li, J., Ozarowski, A., Sleight, A.W., Subramanian, M.A., "Intense Turquoise and Green Colors in Brownmillerite-Type Oxides Based on Mn^{5+} in $Ba_2In_{2-x}Mn_xO_{5+x}$," Inorg. Chem. **52**(3), 1349 (2013).

Kalinowski, A., Qin, Z., Coffey, K., Kodali, R., Buehler, M.J., Lösche, M., Dahl, K.N., "Calcium Causes a Conformational Change in Lamin A Tail Domain that Promotes Farnesyl-Mediated Membrane Association," Biophys. J. **104**(10), 2246 (2013).

Kihm, K., Kirchoff, E., Golden, M., Rosenfeld, J., Rawal, S., Pratt, D., Swanson, A., Bilheux, H., Walker, L., Voisin, S., Hussey, D.S., Jacobson, D.L., "Neutron Imaging of Alkali Metal Heat Pipes," Physics Procedia **43**, 323 (2013).

Kilburn, D., Roh, J.H., Behrouzi, R., Briber, R.M., Woodson, S.A., "Crowders Perturb the Entropy of RNA Energy Landscapes to Favor Folding," J. Am. Chem. Soc. **135**(27), 10055 (2013).

Kim, J.M., Fang, J., Eberle, A.P.R., Castañeda-Priego, R., Wagner, N.J., "Gel Transition in Adhesive Hard-Sphere Colloidal Dispersions: The Role of Gravitational Effects," Phys. Rev. Lett. **110**(20), 208302 (2013). [CHRNS]

Kim, J., Gao, Y., Hebebrand, C., Peirtsegaele, E., Helgeson, M.E., "Polymer-Surfactant Complexation as a Generic Route to Responsive Viscoelastic Nanoemulsions," Soft Matter, in press. [CHRNS]

Kim, S., Dura, J.A., Page, K.A., Rowe, B.W., Yager, K.G., Lee, H.-J., Soles, C.L., "Surface-Induced Nanostructure and Water Transport of Thin Proton-Conducting Polymer Films," Macromolecules **46**(14), 5630 (2013).

Kimura, K., Nakatsuji, S., Wen, J.-J., Broholm, C., Stone, M.B., Nishibori, E., Sawa, H., "Quantum Fluctuations in Spin-ice-like $Pr_2Zr_2O_7$," Nat. Commun. **4**(1934), 1 (2013). [CHRNS]

Kirby, B.J., Rahman, M.T., Dumas, R.K., Davies, J.E., Lai, C.-H., Liu, K., "Depth-resolved Magnetization Reversal in Nanoporous Perpendicular Anisotropy Multilayers," J. Appl. Phys. **113**(3), 033909 (2013).

Kirshenbaum, K., Butch, N.P., Saha, S.R., Zavalij, P.Y., Ueland, B.G., Lynn, J.W., Paglione, J., "Tuning Magnetism in FeAs-Based Materials via a Tetrahedral Structure," Phys. Rev. B **86**(6), 060504 (2012).

Kitchen, B.B., Verdal, N., Udovic, T.J., Rush, J.J., Hartman, M.R., DeVries, D.J., "Investigation of an Unusual Low-Temperature Phase Transformation in $RbBH_4$ by Neutron Diffraction," J. Solid State Chem. **203**, 51 (2013).

Kizilay, E., Dinsmore, A.D., Hoagland, D.A., Sun, L., Dubin, P.L., "Evolution of Hierarchical Structures in Polyelectrolyte-Micelle Coacervates," Soft Matter, in press. [CHRNS]

Kofu, M., Nagao, M., Ueki, T., Kitazawa, Y., Nakamura, Y., Sawamura, S., Watanabe, M., Yamamuro, O., "Heterogeneous Slow Dynamics of Imidazolium-Based Ionic Liquids Studied by Neutron Spin Echo," J. Phys. Chem. B **117**(9), 2773 (2013). [CHRNS]

Krycka, K.L., Borchers, J.A., Laver, M., Salazar-Alvarez, G., López-Ortega, A., Estrader, M., Suriñach, S., Baró, M.D., Sort, J., Nogués, J., "Correlating Material-Specific Layers and Magnetic Distributions within Onion-Like Fe_3O_4|MnO|γ-Mn_2O_3 Core/Shell Nanoparticles,"J. Appl. Phys. **113**(17), 17B531-1 (2013). [CHRNS]

Krycka, K.L., Borchers, J.A., Salazar-Alvarez, G., López-Ortega, A., Estrader, M., Estradé, S., Winkler, E., Zysler, R.D., Sort, J., Peiró, F., Baró, M.D., Kao, C.-C., Nogués, J., "Resolving Material-Specific Structures within Fe_3O_4|γ-Mn_2O_3 Core|Shell Nanoparticles Using Anomalous Small-Angle X-ray Scattering," ACS Nano **7**(2), 921 (2013). [CHRNS]

Kumari, H., Kline, S.R., Dennis, C.L., Mossine, A.V., Paul, R.L., Deakyne, C.A., Atwood, J.L., "Solution-Phase and Magnetic Approach Towards Understanding Iron Gall Ink-like Nanoassemblies," Angew. Chem. Int. Ed. **37**, 9263 (2012).

Kumari, H., Kline, S.R., Wycoff, W.G., Atwood, J.L., "Investigating Structural Alterations in Pyrogallol[4] Arene-Pyrene Nanotubular Frameworks," Small **8**(21), 3321 (2012).

Kumi, B.C., Greer, S.C., "Micelles of Polybutadiene-*b*-poly(ethylene oxide) in Deuterated Methanol and Deuterated Cyclohexane," J. Colloid Interf. Sci. **386**(1), 212 (2012). [CHRNS]

Langford, T.J., Bass, C.D., Beise, E.J., Breuer, H., Erwin, D.K., Heimbach, C.R., Nico, J.S., "Event Identification ^{3}He Proportional Counters using Risetime Discrimination," Nucl. Instrum. Meth. A **717**, 51 (2013).

Lee, H.B., Chun, S.H., Shin, K.W., Jeon, B.-G., Chai, Y.S., Kim, K.H., Schefer, J., Chang, H., Yun, S.-N., Joung, T.-Y., Chung, J.-H., "Heliconical Magnetic Order and Field-Induced Multiferroicity of the Co_2Y-type Hexaferrite $Ba_{0.3}Sr_{1.7}Co_2Fe_{12}O_{22}$," Phys. Rev. B **86**(9), 094435 (2012).

Lee, H.-Y., Hashizaki, K., Diehn, K., Raghavan, S.R., "Reverse Self-Assembly of Lipid Onions Induced by Gadolinium and Calcium Ions," Soft Matter **9**(1), 200 (2013). [CHRNS]

Lee, J., Stone, M.B., Huq, A., Yildirim, T., Ehlers, G., Mizuguchi, Y., Miura, O., Takano, Y., Deguchi, K., Demura, S., Lee, S.-H., "Crystal Structure, Lattice Vibrations, and Superconductivity of $LaO_{1-x}F_xBiS_2$," Phys. Rev. B **87**(20), 205134 (2013).

Li, G., Rao, G., Huang, Q., Gao, Q., Luo, J., Liu, G., Li, J., Liang, J., "Phase Precipitation in the $Bi_{1-x}Ca_xMnO_3$ Compounds (x=0.4-0.6)," Europhys. Lett. **101**, 67004 (2013).

Li, X., Malardier-Jugroot, C., "Confinement Effect in the Synthesis of Polypyrrole within Polymeric Templates in Aqueous Environments," Macromolecules **46**(6), 2258 (2013). [CHRNS]

Lin, K.-J., Maranas, J.K., "Cation Coordination and Motion in a Poly(ethylene oxide)-Based Single Ion Conductor," Macromolecules **45**, 6230 (2012). [CHRNS]

Liu, D., Hussey, D., Gubarev, M.V., Ramsey, B.D., Jacobson, D., Arif, M., Moncton, D.E., Khaykovich, B., "Demonstration of Achromatic Cold-Neutron Microscope Utilizing Axisymmetric Focusing Mirrors," Appl. Phys. Lett. **102**(18), 183508 (2013).

Liu, X., Majzoub, E.H., Stavila, V., Bhakta, R.K., Allendorf, M.D., Shane, D.T., Conradi, M.S., Verdal, N., Udovic, T.J., Hwang, S.-J., "Probing the Unusual Anion Mobility of $LiBH_4$ Confined in Highly Ordered Nanoporous Carbon Frameworks via Solid State NMR and Quasielastic Neutron Scattering," J. Phys. Chem. A, in press. [CHRNS]

Liu, Y., Brown, C.M., Neumann, D.A., Geohegan, D.B., Puretzky, A.A., Rouleau, C.M., Hu, H., Styers-Barnett, D., Krasnov, P.O., Yakobson, B.I., "Metal-Assisted Hydrogen Storage on Pt-Decorated Single-Walled Carbon Nanohorns," Carbon **50**(13), 4953 (2012).

Livingston, R., Nemes, N., Neumann, D., "Quasi-Elastic Neutron Scattering Investigation of the Effect of Water/Cement Ratio on Tricalcium Silicate Hydration," in "13th International Conference on the Chemistry of Cement," edited by Palomo, A., Zaragoze A., Agui, J., (ICCC, 2011, Madrid, Conf. Proc.) (2011).

Long, G.G., Chapman, K.W., Chupas, P.J., Bendersky, L.A., Levine, L.E., Mompiou, F., Stalick, J.K., Cahn, J.W., "Highly Ordered Noncrystalline Metallic Phase," Phys. Rev. Lett. **111**(1), 015502 (2013).

López-Barrón, C.R., Wagner, N.J., "Structural Transitions of CTAB Micelles in a Protic Ionic Liquid," Langmuir **28**(35), 12722 (2012).

López-Barrón, C.R., Li, D., DeRita, L., Basavaraj, M.G., Wagner, N.J., "Spontaneous Thermoreversible Formation of Cationic Vesicles in a Protic Ionic Liquid," J. Am. Chem. Soc. **134**(51), 20728 (2012). [CHRNS]

Lott, J.R., McAllister, J.W., Arvidson, S.A., Bates, F.S., Lodge, T.P., "Fibrillar Structure of Methylcellulose Hydrogels," Biomacromolecules, in press.

Luo, J., Wu, H., Zhou, W., Kang, X., Wang, P., "$Li_2(NH_2BH_3)(BH_4)/LiNH_2BH_3$: the First Metal Amidoborane Borohydride Complex with Inseparable Amidoborane Precursor for Hydrogen Storage," Int. J. Hydrogen Energ. **38**(1), 197 (2013).

Luzin, V., Prask, H. J., Gnäupel-Herold, T., Gordon, J., Wexler, D., Rathod, C.H., Pal, S., Daniel, W., Atrens, A., "Neutron Residual Stress Measurements in Rails," Neutron News **24**(3), 9 (2013).

Lynn, J.W., "Magnetic Neutron Scattering," in "Characterization of Materials, 1st ed.," edited by Kaufmann, E.N. (Wiley & Sons, Inc., Hoboken, NJ), 1328 (2012).

Magiera, J., "Validation of an Experimental Technique with the Physically Based Global Method," CAMES **19**(4), 369 (2012).

Majkrzak, C., Borchers, J., "2012 American Conference on Neutron Scattering (ACNS 2012)," Neutron News **23**(4), 7 (2012).

Manahan, M.P., Mench, M.M., "Laser Perforated Fuel Cell Diffusion Media: Engineered Interfaces for Improved Ionic and Oxygen Transport," J. Electrochem. Soc. **159**(7), F322 (2012).

Mang, J.T., Hjelm, R.P., "Fractal Networks of Inter-Granular Voids in Pressed TATB," Propell. Explos. Pyrot., in press.

Manson, J.L., Brown, C.M., Huang, Q., Schlueter, J.A., Lancaster, T., Blundell, S.J., Singleton, J., Lynn, J.W., Pratt, F.L., "$Mn(dca)_2$(o-phen){dca = dicyanamide; o- phen =1,10-Phenanthroline}: Long-Range Magnetic Order in a Low-Dimensional Mn-dca Polymer," Polyhedron **52**, 679 (2013).

Marquardt, D., Williams, J.A., Kučerka, N., Atkinson, J., Wassall, S.R., Katsaras, J., Harroun, T.A., "Tocopherol Activity Correlates with Its Location in a Membrane: A New Perspective on the Antioxidant Vitamin E," J. Am. Chem. Soc. **135**(20), 7523 (2013).

Mastalerz, M., He, L., Melnichenko, Y.B., Rupp, J.A., "Porosity of Coal and Shale: Insights from Gas Adsorption and SANS/USANS Techniques," Energ. Fuel. **26**(8), 5109 (2012). [CHRNS]

Miao, Y., Yi, Z., Cantrell, C., Glass, D.C., Baudry, J., Jain, N., Smith, J.C., "Coupled Flexibility Change in Cytochrome P450cam Substrate Binding Determined by Neutron Scattering, NMR, and Molecular Dynamics Simulation," Biophys. J. **103**(10), 2167 (2012). [CHRNS]

Miao, Y., Yi, Z., Glass, D.C., Hong, L., Tyagi, M., Baudry, J., Jain, N., Smith, J.C., "Temperature-Dependent Dynamical Transitions of Different Classes of Amino Acid Residue in a Globular Protein," J. Am. Chem. Soc. **134**(48), 19576 (2012). [CHRNS]

Mossine, A.V., Kumari, H., Fowler, D.A., Shih, A., Kline, S.R., Barnes, C.L., Atwood, J.L., "Ferrocene Species Included within a Pyrogallo[4]arene Tube," Chem.-Eur. J. **18**(33), 10258 (2012).

Mulligan, P.L., Cao, L.R., Turkoglu, D., "A Multi-detector, Digitizer Based Neutron Depth Profiling Device for Characterizing Thin Film Materials," Rev. Sci. Instrum. **83**(7), 073303 (2012).

Murnen, H.K., Rosales, A.M., Dobrynin, A.V., Zuckermann, R.N., Segalman, R.A., "Persistence Length of Polyelectrolytes with Precisely Located Charges," Soft Matter **9**(1), 90 (2013). [CHRNS]

Nagpure, S.C., Downing, R.G., Bhushan, B., Babu, S.S., "Discovery of Lithium in Copper Current Collectors used in Batteries," Scripta Mater. **67**(7-8), 669 (2012).

Nakano, K., Yajima, T., Takeiri, F., Green, M.A., Hester, J., Kobayashi, Y., Kageyama, H., "*Tc* Enhancement by Aliovalent Anionic Substitution in Superconducting $BaTi_2(Sb_{1-x}Sn_x)_2O$," J. Phys. Soc. Jpn. **82**(7), 074707 (2013).

Natali Sora, I., Caronna, T., Fontana, F., de Julián Fernández, C., Caneschi, A., Green, M.A., Bonville, P., "Charge Compensation and Magnetic Properties in Sr and Cu Doped La-Fe Perovskites," EPJ Web of Conferences **40**, 15005 (2013).

Navarre-Sitchler, A.K., Cole, D.R., Rother, G., Jin, L., Buss, H.L., Brantley, S.L., "Porosity and Surface Area Evolution during Weathering of Two Igneous Rocks," Geochim. Cosmochim. Acta. **109**, 400 (2013). [CHRNS]

Newbloom, G.M., Weigandt, K.M., Pozzo, D.C., "Structure and Property Development of Poly(3-hexylthiophene) Organogels Probed with Combined Rheology, Conductivity and Small Angle Neutron Scattering," Soft Matter **8**(34), 8854 (2012).

Nickels, J.D., O'Neill, H., Hong, L., Tyagi, M., Ehlers, G., Weiss, K.L., Zhang, Q., Yi, Z., Mamontov, E., Smith, J.C., Sokolov, A.P., "Dynamics of Protein and its Hydration Water: Neutron Scattering Studies on Fully Deuterated GFP," Biophys. J. **103**(7), 1566 (2012). [CHRNS]

Njauw, C.-W., Cheng, C.-Y., Ivanov, V.A., Khokhlov, A.R., Tung, S.-H., "Molecular Interactions between Lecithin and Bile Salts/Acids in Oils and Their Effects on Reverse Micellization," Langmuir **29**(12), 3879 (2013).

Ogunsola, O.A., Kraeling, M.E., Zhong, S., Pochan, D.J., Bronaugh, R.L., Raghavan, S.R., "Structural Analysis of 'Flexible' Liposome Formulations: New Insights into the Skin-Penetrating Ability of Soft Nanostructures," Soft Matter **8**(40), 10226 (2012). [CHRNS]

Oh, H., Ketner, A.M., Heymann, R., Kesselman, E., Danino, D., Falvey, D.E., Raghavan, S.R., "A Simple Route to Fluids with Photo-Switchable Viscosities based on a Reversible Transition between Vesicles and Wormlike Micelles," Soft Matter **9**(20), 5025 (2013).

Olds, D.P., Duxbury, P.M., Kiel, J.W., Mackay, M.E., "Percolating Bulk Heterostructures from Neutron Reflectometry and Small-Angle Scattering Data," Phys. Rev. E **86**(6), 061803 (2012). [CHRNS]

Omenya, F., Chernova, N.A., Wang, Q., Zhang, R., Whittingham, M.S., "The Structural and Electrochemical Impact of Li and Fe Site Substitution in $LiFePO_4$," Chem. Mater. **25**(13), 2691 (2013).

Page, K.A., England, D., Texter, J., "Capturing Nanoscale in Network Gels by Microemulsion Polymerization," ACS Macro. Letters **1**(12), 1398 (2012). [CHRNS]

Pajerowski, D.M., Rotundo, C.R., Lynn, J.W., Birgeneau, R.J., "Magnetic Neutron Diffraction Study of $Ba(Fe_{1-x}Co_x)_2As_2$ Critical Exponents through the Tricritical Doping," Phys. Rev. B **87**(13), 134507 (2013).

Pajerowski, D.M., Garlea, V.O., Knowles, E.S., Andrus, M.J., Dumont, M.F., Calm, Y.M., Nagler, S.E., Tong, X., Talham, D.R., Meisel, M.W., "Magnetic Neutron Scattering of Thermally Quenched K-Co-Fe Prussian Blue Analogue Photomagnet," Phys. Rev. B **86**(5), 054431 (2012).

Pajerowski, D.M., Zakrzewksi, B.M., Ravel, B., "X-ray Structural Studies of Prussian Blue Analog Heterostructures on Poly(ethylene terephthalate) Supports," Thin Solid Films **526**, 34 (2012).

Pan, C., Li, H., Akgun, B., Satija, S.K., Zhu, Y., Xu, D., Ortiz, J., Gersappe, D., Rafailovich, M.H., "Enhancing the Efficiency of Bulk Heterojunction Solar Cells via Templated Self-Assembly," Macromolecules **46**(5), 1812 (2013).

Pan, J., Heberle, F.A., Tristram-Nagle, S., Szymanski, M., Koepfinger, M., Katsaras, J., Kučerka, N., "Molecular Structures of Fluid Phase Phosphatidylglycerol Bilayers as Determined by Small Angle Neutron and X-ray Scattering," Biochem. Biophys. Acta **1818**, 2135 (2012). [CHRNS]

Pandey, A., Ueland, B.G., Yeninas, S., Kreyssig, A., Sapkota, A., Zhao, Y., Helton, J.S., Lynn, J.W., McQueeny, R.J., Furukawa, Y., Goldman, A.I., Johnston, D.C., "Coexistence of Half-Metallic Itinerant Ferromagnetism with Local-Moment Antiferromagnetism in $Ba_{0.60}K_{0.40}Mn_2As_2$," Phys. Rev. Lett. **111**(4), 047001 (2013).

Pandey, A., Khan, A.S., Kim, E.-Y., Choi, S.-H., Gnäupel-Herold, T., "Experimental and Numerical Investigations of Yield Surface, Texture, and Deformation Mechanisms in AA5754 Over Low to High Temperatures and Strain Rates," Int. J. Plasticity **41**, 165 (2013).

Pangelis, S., Olsen, S.R., Scherschlight, J., Leão, J.B., Pullen, S.A., Dender, D., Hester, J.R., Imperia, P., "Safety Interlock and Vent System to Alleviate Potentially Dangerous Ice Blockage of Top-loading Cryostat Sample Sticks.," J. Appl. Crystallogr., in press. [CHRNS]

Patterson, J.P., Kelley, E.G., Murphy, R.P., Moughton, A.O., Robin, M.P., Lu, A., Colombani, O., Chassenieux, C., Cheung, D., Sullivan, M.O., Epps, III, T.H., O'Reilly, R.K., "Structural Characterization of Amphiphilic Homopolymer Micelles using Light Scattering, SANS, and Cryo-TEM," Macromolecules, in press.

Patterson, J.P., Cotanda, P., Kelley, E.G., Moughton, A.O., Lu, A., Epps, III, T.H., O'Reilly, R.K., "Catalytic Y-Tailed Amphiphilic Homopolymers - Aqueous Nanoreactors for High Activity, Low Loading SCS Pincer Catalysts," Polym. Chem. **4**(6), 2033 (2013).

Paul, R.L., "Determination of Arsenic in Food and Dietary Supplement Standard Reference Materials by Neutron Activation Analysis," J. Radioanal. Nucl. Ch., in press.

Paul, R.L., Lindstrom, R.M., "Preparation and Certification of Hydrogen in Titanium Alloy Standard Reference Materials," Metall. Trans. A **43**(12), 4888 (2012).

Peng, J., Xu, W., Yan, Y., Yang, J., Fu, L., Kang, H., He, J., "Study on Lattice Dynamics of filled Skutterudites $In_xYb_yCo_4Sb_{12}$," J. Appl. Phys. **112**(2), 024909 (2012).

Peng, Y., Krungleviciute, V.N., Eryazici, I., Hupp, J.T., Farha, O.K., Yildirim, T., "Methane Storage in Metal-Organic Frameworks: Current Records, Surprise Findings, and Challenges," J. Am. Chem. Soc., in press.

Peng, Y., Srinivas, G., Wilmer, C.E., Eryazici, I., Snurr, R.Q., Hupp, J.T., Yildirim, T., Farha, O.K., "Simultaneously High Gravimetric and Volumetric Methane Uptake Characteristics of the Metal-Organic Framework NU-111," Chem. Commun. **49**(29), 2992 (2013).

Perez Mendez, M., Hammouda, B., "SAXS and SANS Investigation of Synthetic Cholesteric Liquid-Crystal Polymers for Biomedical Applications," J. Mtls. Sci. Eng. B **3**(2), 104 (2013). [CHRNS]

Petzetakis, N., Robin, M.P., Patterson, J.P., Kelley, E.G., Cotanda, P., Bomans, P.H.H., Sommerdijk, N.A.J., Dove, A.P., Epps, III, T.H., O'Reilly, R.K., "Hollow Block Copolymer Nanoparticles through a Spontaneous One-Step Structural Reorganization," ACS Nano **7**(2), 1120 (2013).

Pimpinella, R.E., Zhang, D., McCartney, M.R., Smith, D.J., Krycka, K.L., Kirby, B.J., O'Dowd, B.J., Sonderhouse, L., Leiner, J., Liu, X., Dobrowolska, M., Furdyna, J.K., "Magnetic Properties of GaAs/Fe Core/Shell Nanowires," J. Appl. Phys. **113**(17), 17B5201 (2013). [CHRNS]

Polsky, Y., Anovitz, L.M., Bingham, P., Carmichael, J., "Application of Neutron Imaging to Investigate Flow Through Fractures for EGS," in "Proceedings, Thirty-Eighth Workshop on Geothermal Reservoir Engineering," (Stanford Geothermal Workshop, February 2013, Stanford, CA) **SGP-TR-198** (2013).

Pratt, D.K., Chang, S., Tain, W., Taskin, A.A., Ando, Y Zarestky, J.L., Kreyssig, A., Goldman, A.I., McQueeney, R., "Checkerboard to Stripe Charge Ordering Transition in $TbBaFe_2O_5$," Phys. Rev. B **87**(4), 045127 (2013).

Purewal, J., Keith, J.B., Ahn, C.C., Brown, C.M., Tyagi, M., Fultz, B., "Hydrogen Diffusion in Potassium Intercalated Graphite Studied by Quasielastic Neutron Scattering," J. Chem. Phys. **137**(22), 224704 (2012). [CHRNS]

Qajar, A., Peer, M., Rajagopalan, R., Liu, Y., Brown, C., Foley, H.C., "Surface Compression of Light Adsorbates Inside Microporous PFA-Derived Carbons," Carbon **60**, 538 (2013).

Qian, K.K., Zhou, W., Xu, X., Udovic, T.J., "Characterization of Medicinal Compounds Confined in Porous Media by Neutron Vibrational Spectroscopy and First-Principles Calculations: A Case Study with Ibuprofen," Pharm. Res. **29**(9), 2432 (2012).

Rao, X., Cai, J., Yu, J., He, Y., Wu, C., Zhou, W., Yildirim, T., Chen, B., Qian, G., "A Microporous Metal-Organic Framework with Both Open Metal and Lewis Basic Pyridyl Sites for High C_2H_2 and CH4 Storage at Room Temperature," Chem. Commun., in press.

Ratcliff, II, W., Yamani, Z., Anbusathaiah, V., Gao, T.R., Kienzle, P.A., Cao, H., Takeuchi, I., "Electric-Field-Controlled Antiferromagnetic Domains in Epitaxial $BiFeO_3$ Thin Films Probed by Neutron Diffraction," Phys. Rev. B **87**(14), 140405 (2013).

Reents-Budet, D., Stanley, G., Bishop, R.L., Blackman, M.J., "Identity and Interaction: Ceramic Styles and Social History of the Ik' Polity, Guatemala," in "Motul de San José: politics, history and economy in a Maya polity," edited by Foias, A.E. and Emery, K.F., (University of Florida Press, Gainesville) 67 (2012).

Reents-Budet, D., Bishop, R.L., "Classic Maya Painted Ceramics: Artisans, Workshops, and Distribution," in "Ancient Maya Art at Dumbarton Oaks," edited by Pillsbury, J., Doutriaux , M., Ishihara-Brito, R., Tokovinine, A., (Pre-columbian Art at Dumbarton Oaks, Number 4. Dumbarton Oaks Research Library and Collection, Washington, D.C.) (2012).

Rehm, C., Barker, J., Bouwman, W.G., Pynn, R., "DCD USANS and SESANS: a Comparison of Two Neutron Scattering Techniques Applicable for the Study of Large-Scale Structures," J. Appl. Crystallogr. **46**(2), 354 (2013). [CHRNS]

Reyes-Ortiz, V., Heins, R.A., Cheng, G., Kim, E.Y., Vernon, B.C., Elandt, R.B., Adams, P.D., Sale, K.L., Hadi, M.Z., Simmons, B.A., Kent, M.S., Tullman-Ercek, D., "Addition of a Carbohydrate-binding Module Enhances Cellulase Penetration into Cellulose Substrates," Biotechnol Biofuels **6**, 93 (2013).

Rikkou-Kalourkoti, M., Patrickios, C.S., "Synthesis and Characterization of End-Linked Amphiphilic Copolymer Conetworks Based on a Novel Bifunctional Cleavable Chain Transfer Agent," Macromolecules **45**(19), 7890 (2012).

Ro, H.W., Akgun, B., O'Connor, B.T., Hammond, M., Kline, R.J., Snyder, C.R., Satija, S.K., Ayzner, A.L., Toney, M.F., Soles, C.L., DeLongchamp, D.M., "Poly(3-hexylthiophene) and [6,6]-Phenyl-C_{61}-butyric Acid Methyl Ester Mixing in Organic Solar Cells," Macromolecules **45**(16), 6587 (2012).

Rubinson, K.A., Meuse, C.W., "Deep Hydration: Poly(ethylene glycol) M_w 2000-8000 Da Probed by Vibrational Spectrometry and Small-Angle Neutron Scattering and Assignment of ΔG° to Individual Water Layers," Polymer **54**(2), 709 (2013). [CHRNS]

Rubinson, K.A., Pokalsky, C., Krueger, S., Prochaska, L.J., "Structure Determination of Functional Membrane Proteins using Small-Angle Neutron Scattering (SANS) with Small, Mixed-Lipid Liposomes: Native Beef Heart Mitochondrial Cytochrome *c* Oxidase Forms Dimers," Protein J. **32**(1), 27 (2013). [CHRNS]

Ruppert, L.F., Sakurovs, R., Blach, T.P., He, L., Melnichenko, Y.B., Mildner, D.F.R., Alcantar-Lopez, L., "A USANS/SANS Study of the Accessibility of Pores in the Barnett Shale to Methane and Water," Energ. Fuel. **27**(2), 772 (2013). [CHRNS]

Sadakane, K., Horikawa, Y., Nagao, M., Seto, H., "The Effect of Tetraphenylphosphonium Chloride on Phase Behavior and Nanoscale Structures in a Mixture of D_2O and 3-Methylpyridine," Chem. Lett. **41**(10), 1075 (2012).

Satsoura, D., Kučerka, N., Shivakumar, S., Pencer, J., Groffiths, C., Leber, B., Andrews, D.W., Katsaras, J., Fradin, C., "Interaction of the Full-Length Bax Protein with Biomimetic Mitochondrial Liposomes: A Small-Angle Neutron Scattering and Fluorescence Study," Biochim. Biophys. Acta, Biomembr. **1818**(3), 384 (2013). [CHRNS]

Savary, L., Ross, K.A., Gaulin, B.D., Ruff, J.P.C., Balents, L., "Order by Quantum Disorder in $Er_2Ti_2O_7$," Phys. Rev. Lett. **109**(16), 167201 (2012). [CHRNS]

Selamet, O.F., Pasaogullari, U., Spernjak, D., Hussey, D.S., Jacobson, D.L., Mat, M.D., "Two-phase Flow in a Proton Exchange Membrane Electrolyzer Visualized *in situ* by Simultaneous Neutron Radiography and Optical Imaging," Int. J. Hydrogen Energ. **38**(14), 5823 (2013).

Shenoy, S.S., Nanda, H., Lösche, M., "Membrane Association of the PTEN Tumor Suppressor: Electrostatic Interaction with Phosphatidylserine-Containing Bilayers and Regulatory Role of the C-Terminal Tail," J. Struct. Biol. **180**(3), 394 (2012).

Shin, N., Kang, J., Richter, L.J., Prabhu, V.M., Kline, R.J., Fischer, D.A., DeLongchamp, D.M., Toney, M.F., Satija, S.K., Gundlach, D.J., Purushothaman, B., Anthony, J.E., Yoon, D.Y., "Vertically Segregated Structure and Properties of Small Molecule-Polymer Blend Semiconductors for Organic Thin-Film Transistors," Adv. Funct. Mater. **23**(3), 366 (2013).

Siegel, J.B., Stefanopoulou, A.G., Hagans, P., Ding, Y., Gorsich, D., "Expansion of Lithium Ion Pouch Cell Batteries: Observations from Neutron Imaging," J. Electrochem. Soc. **160**(8), A1031 (2013).

Simmons, D.S., Cicerone, M.T., Zhong, Q., Tyagi, M., Douglas, J.F., "Generalized Localization Model of Relaxation in Glass-forming Liquids," Soft Matter **8**(45), 11455 (2012). [CHRNS]

Singh, D.K., Lee, Y., "Nonconventional Spin Glass Transition in a Chemically Ordered Pyrochlore," Phys. Rev. Lett. **109**(24), 247201 (2012). [CHRNS]

Singh, D.K., Thamizhavel, A., Lynn, J.W., Dhar, S.K., Hermann, T., "Multiple Magnetic Structures of Correlated Ce-ions in Intermetallic $CeAu_2Ge_2$," Phys. Rev. B **86**(6), 060405 (2012). [CHRNS]

Snow, W.M., Anderson, E., Barrón-Palos, L., Bass, C.D., Bass, T.D., Crawford, B.E., Fry, J., Gan, K., Heckel, B.R., Luo, D., Malone, R.C., Markoff, D.M., Micherdzinska, A.M., Mumm, H.P., Nico, J.S., Opper, A.K., Penn, S., Santra, S., Sarsour, M., Sharapov, E.I., Swanson, H.E., Van Sciver, S., Walbridge, S.B., Zhumabekova, V., "Parity Violating Neutron Spin Rotation in ^{4}He and H," Il Nuovo Cimento **35**(4), 57 (2012).

Song, Y., Carr, S.V., Lu, X., Zhang, C., Sims, Z.C., Luttrell, N.F., Chi, S., Zhao, Y., Lynn, J.W., Dai, P., "Uniaxial Pressure Effect on Structural and Magnetic Phase Transitions in NaFeAs and its Comparison with As-Grown and Annealed $BaFe_2As_2$," Phys. Rev. B **87**(18), 184511 (2013).

Sorte, E.G., Bowman, Jr., R.C., Majzoub, E.H., Verkuijlen, M.H.W., Udovic, T.J., Conradi, M.S., "Mobile Species in $NaAlH_4$," J. Phys. Chem. C **117**(16), 8015 (2013).

Srinivas, G., Travis, W., Ford, J., Wu, H., Guo, Z.-X., Yildirim, T., "Nanoconfined Ammonia Borane in a Flexible Metal-Organic Framework Fe-MIL-53: Clean Hydrogen Release with Fast Kinetics," J. Mater. Chem. A **1**(13), 4167 (2013).

Stalick, J.K., Wang, K., Waterstrat, R.M., "The Crystal Structure and Phase Transition of Hf_2Pt_3," J. Phase Equilib. Diff. **1**, (1) (2013).

Starowicz, P., Schwab, H., Goraus, J., Zajdel, P., Forster, F., Rak, J.R., Green, M.A., Vobornik, I., Reinert, F., "A Flat Band at the Chemical Potential of a $Fe_{1.03}Te_{0.94}S_{0.06}$ Superconductor Observed by Angle-Resolved Photoemission Spectroscopy," J. Phys.: Condens. Matter **25**(19), 195701 (2013).

Stock, C., Broholm, C., Zhao, Y., Demmel, F., Kang, H.J., Rule, K.C., Petrovic, C., "Magnetic Field Splitting of the Spin Resonance in $CeCoIn_5$," Phys. Rev. Lett. **109**(16), 167207 (2012). [CHRNS]

Stock, C., Broholm, C., Demmel, F., Van Duijn, J., Taylor, J.W., Kang, H.J., Hu, R., Petrovic, C., "From Incommensurate Correlations to Mesoscopic Spin Resonance in $YbRh_2Si_2$," Phys. Rev. Lett. **109**(12), 127201 (2012).

Stock, C., Gehring, P.M., Hiraka, H., Swainson, I., Xu, G., Ye, Z.-G., Luo, H., Li, J.-F., Viehland, D., "Evidence for Anisotropic Polar Nanoregions in Relaxor $Pb(Mg_{1/3}Nb_{2/3})O_3$: A Neutron Study of the Elastic Constants and Anomalous TA Phonon Damping in PMN," Phys. Rev. B **86**(10), 104108 (2012). [CHRNS]

Subramanian, D., Boughter, C.T., Klauda, J.B., Hammouda, B., Anisimov, M.A., "Mesoscale Inhomogeneities in Aqueous Solutions of Small Amphiphilic Molecules," Faraday Discuss., in press. [CHRNS]

Swain, M., Singh, S., Basu, S., Gupta, M., "Effect of Interface Morphology on Intermetallics Formation upon Annealing of Al-Ni Multilayer," J. Alloy Compd., in press.

Tang, Z., Tan, Y., Wu, H., Gu, Q., Zhou, W., Jensen, C.M., Yu, X., "Metal Cation-Promoted Hydrogen Generation in Activated Aluminium Borohydride Ammoniates," Acta Mater. **61**(13), 4787 (2013).

Tarasevich, B.J., Perez-Salas, U., Masica, D.L., Philo, J., Kienzle, P., Krueger, S., Majkrzak, C.F., Gray, J.L., Shaw, W.J., "Neutron Reflectometry Studies of the Adsorbed Structure of the Amelogenin, LRAP," J. Phys. Chem. B **117**(11), 3098 (2013).

Tong, P., Louca, D., Wang, G., Liaw, P.K., Yokoyama, Y., Llobet, A., Kawaji, H., Qiu, Y., Shi, Y., "Structural Irreversibility in Enhanced Brittleness under Fatigue in Zr-Based Amorphous Solids," Metals **2**(4), 529 (2012). [CHRNS]

Tong, X., Jiang, C.Y., Lauter, V., Ambaye, H., Brown, D., Crow, L., Gentile, T.R., Goyette, R., Lee, W.T., Parizzi, A., Robertson, J.L., "*In situ* polarized ^{3}He System for the Magnetism Reflectometer at the Spallation Neutron Source," Rev. Sci. Instrum. **83**(7), 075101 (2012).

Toppozini, L., Armstrong, C.L., Barrett, M.A., Zheng, S., Luo, L., Nanda, H., García Sakai, V., Rheinstädter, M.C., "Partitioning of Ethanol into Lipid Membranes and its Effect on Fluidity and Permeability as seen by X-ray and Neutron Scattering," Soft Matter **8**, 11839 (2012). [CHRNS]

Tung, W.-S., Bird, V., Composto, R.J., Clarke, N., Winey, K.I., "Polymer Chain Conformations in CNT/PS Nanocomposites from Small Angle Neutron Scattering," Macromolecules **46**(13), 5345 (2013). [CHRNS]

Udovic, T.J., Verdal, N., Rush, J.J., De Vries. D.J., Hartman, M.R., Vajo, J.J., Gross, A.F., Skripov, A.V., "Mapping Trends in the Reorientational Mobilities of Tetrahydroborate Anions via Neutron-Scattering Fixed-Window Scans," J. Alloy Compd., in press. [CHRNS]

Vaish, A., Silin, V., Walker, M.L., Steffens, K.L., Krueger, S., Yeliseev, A.A., Gawrisch, K., Vanderah, D.J., "A Generalized Strategy for Immobilizing Uniformly Oriented Membrane Proteins at Solid Interfaces," Chem. Commun. **49**, 2685 (2013).

Van Dyk, A., Nakatani, A., "Shear Rate-Dependent Structure of Polymer-Stabilized TiO_2 Dispersions," J. Coating. Tech. Res. **10**(3), 297 (2013). [CHRNS]

Verdal, N., Udovic, T.J., Zhou, W., Rush, J.J., De Vries, D.J., Hartman, M.R., "Vibrational Spectroscopic Study of Subtle Phase Transitions in Alkali Borohydrides: Comparison with First-Principles Calculations," J. Phys. Chem. C **117**(2), 876 (2013).

Verdal, N., Udovic, T.J., Rush, J.J., Wu, H., Skripov, A.V., "Evolution of the Reorientational Motions of the Tetrahydroborate Anions in Hexagonal $LiBH_4$-LiI Solid Solution by High-*Q* Quasielastic Neutron Scattering," J. Phys. Chem. C **117**(23), 12010 (2013). [CHRNS]

Wagman, J.J., Van Gastel, G., Ross, K.A., Yamani, Z., Zhao, Y., Qiu, Y., Copley, J.R.D., Kallin, A.B., Mazurek, E., Carlo, J.P., Dabkowska, H.A., Gaulin, B.D., "Two-Dimensional Incommensurate and Three Dimensional Commensurate Magnetic Order and Fluctuations in $La_{2-x}Ba_xCuO_4$," Phys. Rev. B **88**(1), 014412 (2013). [CHRNS]

Wang, H.-W., Wesolowski, D.J., Proffen, T.E., Vlcek, L., Wang, W., Allard, L.F., Kolesnikov, A.I., Feygenson, M., Anovitz, L.M., Paul, R.L., "Structure and Stability of SnO_2 Nanocrystals and Surface-Bound Water Species," J. Am. Chem. Soc. **135**(18), 6885 (2013).

Wang, R., Yang, C., Fan, M., Wu, M., Wang, C., Yu, X., Zhu, J., Zhang, J., Li, G., Huang, Q., Chen, D., Jin, T., Kamiyama, T., Liao, F., Lin, J., "Phase Relationship of the $TbO_{1.81}$-Mn_3O_4-Fe_2O_3 System Synthesized at 1200 °C," J. Alloy Compd. **554**, 385 (2013).

Watson, B.J., Hammouda, B., Briber, R.M., Hutcheson, S.W., "Influence of Organic Liquids on the Nanostructure of Precipitated Cellulose," J. Appl. Polym. Sci. **127**(4), 2620 (2013). [CHRNS]

Watson, M.C., Curtis, J.E., "Rapid and Accurate Calculation of Small-Angle Scattering Profiles using the Golden Ratio," J. Appl. Cryst., in press.

Weigandt, K.M., White, N., Chung, D., Ellingson, E., Wang, Y., Fu, X., Pozzo, D.C., "Fibrin Clot Structure and Mechanics Associated with Specific Oxidation of Methionine Residues in Fibrinogen," Biophys. J. **103**(11), 2399 (2012). [CHRNS]

Welch, C., Labouriau, A., Hjelm, R., Orler, B., Johnston, C., Kim, Y.S., "Nafion in Dilute Solvent Systems: Dispersion or Solution?," ACS Macro Letters **1**, 1403 (2012). [CHRNS]

Wignall, G.D., Littrell, K.C., Heller, W.T., Melnichenko, Y.B., Bailey, K.M., Lynn, G.W., Myles, D.A., Urban, V.S., Buchanan, M.V., Selby, D.L., Butler, P.D., "The 40 m General Purpose Small-Angle Neutron Scattering Instrument at Oak Ridge National Laboratory," J. Appl. Crystallogr. **45**(5), 990 (2012).

Wilmer, C.E., Farha, O.K., Yildirim, T., Eryazici, I., Krungleviciute, V., Sarjeant, A.A., Snurr, R.Q., Hupp, J.T., "Gram-Scale, High-Yield Synthesis of a Robust Metal-Organic Framework for Storing Methane and Other Gases," Energy Environ. Sci. **6**(4), 1158 (2013).

Wong-Ng, W., Kaduk, J.A., Wu, H., Suchomel, M., "Synchrotron X-Ray Studies of Metal-Organic Framework M_2(2,5-Dihydroxyterephthalate), *M*=(Mn, Co, Ni, Zn) (MOF74)," Powder Diffr. **27**(4), 256 (2012).

Wong-Ng, W., Kaduk, J.A., Huang, Q., Espinal, L., Li, L., Burress, J.W., "Investigation of NaY Zeolite with Adsorbed CO_2 by Neutron Powder Diffraction," Micropor. Mesopor. Mat. **172**, 95 (2013).

Wright, N.T., Raththagala, M., Hemmis, C.W., Edwards, S., Curtis, J.E., Krueger, S., Schildbach, J.F., "Solution Structure and Small Angle Scattering Analysis of Tral (381-569)," Proteins **80**(9), 2250 (2012). [CHRNS]

Wu, B., Liu, Y., Li, X., Mamontov, E., Kolesnikov, A.I., Diallo, S.O., Do, C., Porcar, L., Hong, K., Smith, S.C., Liu, L., Smith, G.S., Egami, T., Chen, W.-R., "Charge-Dependent Dynamics of a Polyelectrolyte Dendrimer and Its Correlation with Invasive Water," J. Am. Chem. Soc. **135**(13), 5111 (2013). [CHRNS]

Wu, B., Chen, W.-R., Egami, T., Li, X., Liu, Y., Wang, Y., Do, C., Porcar, L., Hong, K., Liu, L., Smith, G.S., Smith, S.C., "Molecular Dynamics and Neutron Scattering Study of the Dependence of Polyelectrolyte Dendrimer Conformation on Counterion Behavior," J. Chem. Phys. **137**(6), 064902 (2012).

Wu, H., Chua, Y.S., Krungleviciute, V., Tyagi, M., Chen, P., Yildirim, T., Zhou, W., "Unusual and Highly Tunable Missing-Linker Defects in Zirconium Metal-Organic Framework UiO-66 and Their Important Effects on Gas Adsorption," J. Am. Chem. Soc. **135**(28), 10525 (2013). [CHRNS]

Wu, H., Yildirim, T., Zhou, W., "Exceptional Mechanical Stability of Highly Porous Zirconium Metal-Organic Framework UiO-66 and its Important Implications," J. Phys. Chem. Lett. **4**(6), 925 (2013).

Xie, W., Hitchcock, D.A., Kang, H.J., He, J., Tang, X., Laver, M., Hammouda, B., "The Microstructure Network and Thermoelectric Properties of Bulk $(BiSb)_2Te_3$," Appl. Phys. Lett. **101**(11), 113902 (2012). [CHRNS]

Xu, L., Zhang, Q., Hou, G., Chen, P., Li, G., Pajerowski, D.M., Dennis, C.L., "Syntheses, Structures, and Magnetic Properties of Salen Type Cu-Gd Dimer and Hexamer Complexes with Strong Ferromagnetic Interactions," Polyhedron **52**, 91 (2013).

Xu, Z., Wen, J., Berlijn, T., Gehring, P.M., Stock, C., Stone, M.B., Ku, W., Gu, G., Shapiro, S.M., Birgeneau, R.J., Xu, G., "Thermal Evolution of the Full Three-Dimensional Magnetic Excitations in the Multiferroic $BiFeO_3$," Phys. Rev. B **86**(17), 174419 (2012).

Xu, Z., Wen, J., Zhao, Y., Matsuda, M., Ku, W., Liu, X., Gu, G., Lee, D.-H., Birgeneau, R.J., Tranquada, J.M., Xu, G., "Temperature-Dependent Transformation of the Magnetic Excitation Spectrum on Approaching Superconductivity in $Fe_{1+y-x}(Ni/Cu)_xTe_{0.5}Se_{0.5}$," Phys. Rev. Lett. **109**(22), 227002 (2012).

Xu, Z., Wen, J., Mamontov, E., Stock, C., Gehring, P.M., Xu, G., "Freezing of the Local Dynamics in the Relaxor Ferroelectric $[Pb(Zn_{1/3}Nb_{2/3})O_3]_{0.955}[PbTiO_3]_{0.045}$," Phys. Rev. B **86**(14), 144106 (2012).

Yamada, T., Yamada, T., Tyagi, M., Nagao, M., Kitagawa, H., Yamamuro, O., "Phase Transition and Dynamics of Water Confined in Hydroxyethyl Copper Rubeanate Hydrate," J. Phys. Soc. Jpn., in press. [CHRNS]

Yamaguchi, H., Gin, P., Arita, H., Kobayashi, M., Bennett, S., Satija, S.K., Asada, M., Koga, T., Takahara, A., "Effect of Supercritical Carbon Dioxide on Molecular Aggregation States of Side Chains of Semicrystalline Poly{2-(perfluorooctyl)ethyl Acrylate} Brush Thin Films," RSC Advances **3**(14), 4778 (2013).

Yan, H., Snow, W.M., "New Limit on Possible Long-Range Parity-Odd Interactions of the Neutron from Neutron-Spin Rotation in Liquid ^4He," Phys. Rev. Lett. **110**(8), 082003 (2013).

Yang, Y.B., Chen, X.G., Guo, S., Yan, A.R., Huang, Q.Z., Wu, M.M., Chen, D.F., Yang, Y.C., Yang, J.B., "Temperature Dependences of Structure and Coercivity for Melt-Spun MnBi Compound," J. Magn. Magn. Mater. **330**, 106 (2013).

Yao, J., Rudyk, B.W., Brunetta, C.D., Knorr, K.B., Figore, H.A., Mar, A., Aitken, J.A., "Mn Incorporation in $CuInS_2$ Chalcopyrites: Structure, Magnetism and Optical Properties," Mater. Chem. Phys. **136**(2-3), 415 (2012).

Ye, Q., Gentile, T.R., Anderson, J., Broholm, C., Chen, W.C., DeLand, Z., Erwin, R.W., Fu, C.B., Fuller, J., Kirchhoff, A., Rodriguez-Rivera, J.A., Thampy, V., Walker, T.G., Watson, S., "Wide Angle Polarization Analysis with Neutron Spin Filters," Physics Procedia **42**, 206 (2013). [CHRNS]

Yeon, J., Kim, S.-H., Green, M.A., Bhatti, K.P., Leighton, C., Halasyamani, P.S., "Syntheses, Crystal Structures, and Characterization of Two New Tl^+-Cu^{2+}-Te^{6+} Oxides: Tl_4CuTeO_6 and $Tl_6CuTe_2O_{10}$," J. Solid State Chem. **196**, 607 (2012).

Yildirim, T., "Ferroelectric Soft Phonons, Charge Density Wave Instability, and Strong Electron-Phonon Coupling in BiS_2 Layered Superconductors: A First-Principles Study," Phys. Rev. B **87**(2), 020506 (2013).

Yin, L., Lodge, T.P., Hillmyer, M.A., "A Stepwise 'Micellization-Crystallization' Route to Oblate Ellipsoidal, Cylindrical, and Bilayer Micelles with Polyethylene Cores in Water," Macromolecules **45**(23), 9460 (2012).

Yoon, I., Ma, H.B., Winholtz, R.A., "Study of the Effects of Liquid Fraction and Vapor Volume on the Fluctuating Temperature in an Oscillating Heat Pipe using Neutron Imaging," Heat Transfer Research **44**(1), 43 (2013).

Yoon, I., Wilson, C., Borgmeyer, B., Winholtz, R.A., Ma, H.B., Jacobson, D.L., Hussey, D.S., "Neutron Phase Volumetry and Temperature Observations in an Oscillating Heat Pipe," Int. J. Therm. Sci. **60**, 52 (2012).

Yu, J., Phelan, D., Rodriguez-Rivera, J.A., Podlesnyak, A., Louca, D., "Magneto-Polaron Formation and Field-Induced Effects with Dilute Doping in $LaCo_{1-y}Ni_yO_3$" J. Supercond. Nov. Magn., in press. [CHRNS]

Yu, L.L., Jarrett, J.M., Davis, W.C., Kilpatrick, E.L., Oflaz, R., Turk, G.C., Leber, D.D., Valentin, L., Morel-Espinosa, M., Blount, B.C., "Characterization of Perchlorate in a New Frozen Human Urine Standard Reference Material," Anal. Bioanal. Chem. **404**(6-7), 1877 (2012).

Yu, W., Peri, S.R., Akgun, B., Foster, M.D., "Manipulation of Polymer/Polymer Interface Width from Nonequilibrium Deposition," ACS Appl. Mater. Interfaces **5**(8), 2976 (2013).

Yue, M., Liu, D., Huang, Q., Wang, T., Hu, F., Li, J., Rao, G., Shen, B., Lynn, J.W., Zhang, J., "Structure Evolution and Entropy Change of Temperature and Magnetic Field Induced Magneto-Structural Transition in $Mn_{1.1}Fe_{0.9}P_{0.76}Ge_{0.24}$," J. Appl. Phys. **113**(4), 043925 (2013).

Zan, G.H., Tan, C., Deserno, M., Lanni, F., Lösche, M., "Hemifusion of Giant Unilamellar Vesicles with Planar Hydrophobic Surfaces: A Fluorescence Microscopy Study," Soft Matter **8**(42), 10877 (2012).

Zeissler, C.J., Forsley, L.P.G., Lindstrom, R.M., Newsome, S., Kirk, A., Mosier-Boss, P.A., "Radio-microanalytical Particle Measurements Method and Application to Fukushima Aerosols Collected in Japan," J. Radioanal. Nucl. Chem. **296**(2), 1079 (2013).

Zhang, G., Wu, H., Li, G., Huang, Q., Yang, C., Huang, F., Liao, F., Lin, J., "New High T_c Multiferroics $KBiFe_2O_5$ with Narrow Band Gap and Promising Photovoltaic Effect," Sci. Rep. **3**, 1265 (2013).

Zhang, M., Liu, D., Liu, C., Huang, Q., Wang, S., Zhang, H., Yue, M., "Research of the Relationship between Phase Transition Process and Magnetic Properties in Magnetic Refrigeration Material $Mn_{1.2}Fe_{0.8}P_{0.76}Ge_{0.24}$," Acta Meteorol. Sin. **49**(7), 783 (2013).

Zhao, J., Rotundu, C.R., Marty, K., Matsuda, M., Zhao, Y., Setty, C., Bourret-Courchesne, E., Hu, J., Birgeneau, R.J., "Effect of Electron Correlations on Magnetic Excitations in the Isovalently Doped Iron-Based Superconductor $Ba(Fe_{1-x}Ru_x)_2As_2$," Phys. Rev. Lett. **110**(14), 147003 (2013).

Zhao, L.L., Wu, S., Wang, J.K., Hodges, J.P., Broholm, C., Morosan, E., "Quasi-two-Dimensional Noncollinear Magnetism in the Mott Insulator $Sr_2F_2Fe_2OS_2$," Phys. Rev. B **87**(2), 020406 (2013).

Zhou, H.D., Xu, C., Hallas, A.M., Silverstein, H.J., Wiebe, C.R., Umegaki, I., Yan, J.Q., Murphy, T.P., Park, J.-H., Qiu, Y., Copley, J.R.D., Gardner, J.S., Takano, Y., "Successive Phase Transitions and Extended Spin-Excitation Continuum in the S=½ Triangular-Lattice Antiferromagnet $Ba_3CoSb_2O_9$," Phys. Rev. Lett. **109**(26), 267206 (2012). [CHRNS]

Zhu, J., Feng, S., Liu, Q., Zhang, J., Xu, H., Li, Y., Li, X., Liu, J., Huang, Q., Zhao, Y., Jin, C., "Temperature and Pressure Effects of Multiferroic Bi_2NiTiO_6 Compound," J. Appl. Phys. **113**(14), 143514 (2013).

Zilcha, O., Quinn, G.D., Rowe, J.M., Pierce, D.J., "Investigation into the Mechanical Cause of Failure of Neutron Guide NG-2 at the NIST Research Reactor," J. Fail. Anal. and Preven. **12**(6), 604 (2012).

Instruments and Contacts (Name, tel. 301-975-xxxx, email)

High resolution powder diffractometer (BT-1):
- J. K. Stalick, 6223, judith.stalick@nist.gov
- H. Wu, 2387, hui.wu@nist.gov
- Q. Z. Huang, 6164, qing.huang@nist.gov
- C. M. Brown, 5134, craig.brown@nist.gov

Residual stress diffractometer (BT-8):
- T. Gnaeupel-Herold, 5380, thomas.gnaeupel-herold@nist.gov

30-m SANS instrument (NG-7):
- Y. Liu, 6235, yun.liu@nist.gov
- B. Akgun, 6469, bulent.akgun@nist.gov
- P. D. Butler, 2028, paul.butler@nist.gov
- J. R. Krzywon, 6650, jkrzywon@nist.gov

30-m SANS instrument (NG-3) (CHRNS):
- B. Hammouda, 3961, hammouda@nist.gov
- S. Krueger, 6734, susan.krueger@nist.gov
- C. Gagnon, 2020, cedric.gagnon@nist.gov

10-m SANS instrument (NG-B) (nSoft):
- R. Jones, 4624, ronald.jones@nist.gov
- K. Weigandt, 8396, kathleen.weigandt@nist.gov
- K. Page, 5030, kirt.page@nist.gov
- T. Perevozchikova, 8498, tatiana.perevozchikova@nist.gov

USANS, Perfect Crystal SANS (BT-5) (CHRNS):
- D. F. R. Mildner, 6366, david.mildner@nist.gov
- M. J. Wasbrough, 6017, matthew.wasbrough@nist.gov
- P. D. Butler, 2028, paul.butler@nist.gov

Polarized Beam Reflectometer/Diffractometer (NG-D):
- B. J. Kirby, 8395, brian.kirby@nist.gov
- J. A. Borchers, 6597, julie.borchers@nist.gov
- C. F. Majkrzak, 5251, cmajkrzak@nist.gov

MAGIk, Off-Specular Reflectometer (NG-D):
- B. B. Maranville, 6034, brian.maranville@nist.gov
- J. A. Dura, 6251, joseph.dura@nist.gov

Neutron reflectometer-horizontal sample (NG-7):
- S. K. Satija, 5250, satija@nist.gov

Double-focusing triple-axis Spectrometer (BT-7):
- Y. Zhao, 2164, yang.zhao@nist.gov
- J. W. Lynn, 6246, jeff.lynn@nist.gov

SPINS, Spin-polarized triple-axis spectrometer (NG-5):
- L. Harriger, 8360, leland.harriger@nist.gov

Triple-axis spectrometer (BT-4):
- W. Ratcliff, 4316, william.ratcliff@nist.gov

DCS, Disk-chopper time-of-flight spectrometer (NG-4) (CHRNS):
- J. R. D. Copley, 5133, jcopley@nist.gov
- D. Pajerowski, 5660, daniel.pajerowski@nist.gov
- N. Butch, 4863, nicholas.butch@nist.gov
- C. M. Brown, 5134, craig.brown@nist.gov

FANS, Filter-analyzer neutron spectrometer (BT-4):
- T. J. Udovic, 6241, udovic@nist.gov

HFBS, High-flux backscattering spectrometer (NG-2) (CHRNS):
- M. Tyagi, 2046, madhusudan.tyagi@nist.gov
- W. Zhou, 8169, wei.zhou@nist.gov

NSE, Neutron spin echo spectrometer (NG-5) (CHRNS):
- A. Faraone, 5254, antonio.faraone@nist.gov
- M. Nagao, 5505, michihiro.nagao@nist.gov

MACS, Multi-angle crystal spectrometer (BT-9) (CHRNS):
- J. A. Rodriguez-Rivera, 6019, jose.rodriguez@nist.gov
- Y. Qiu, 3274, yiming.qiu@nist.gov

Cold-neutron prompt-gamma neutron activation analysis (NG-D):
- R. L. Paul, 6287, rpaul@nist.gov
- D. J. O'Kelly, 8793, donna.okelly@nist.gov

Thermal-neutron prompt-gamma activation analysis (VT-5):
- R. L. Paul, 6287, rpaul@nist.gov
- D. J. O'Kelly, 8793, donna.okelly@nist.gov

Cold neutron depth profiling (NG-1):
- R. G. Downing, 3782, gregory.downing@nist.gov

Neutron activation analysis facilities:
- D. J. O'Kelly, 8793, donna.okelly@nist.gov

Neutron Imaging Station (BT-2):
- D. Jacobson, 6207, david.jacobson@nist.gov
- D. Hussey, 6465, daniel.hussey@nist.gov
- M. Arif, 6303, muhammad.arif@nist.gov

Neutron interferometer (NG-7):
- M. Arif, 6303, muhammad.arif@nist.gov
- D. Jacobson, 6207, david.jacobson@nist.gov
- D. Hussey, 6465, daniel.hussey@nist.gov

Fundamental neutron physics station (NG-6):
- NG-6M: M. S. Dewey, 4843, mdewey@nist.gov
- NG-6U: H. P. Mumm, 8355, pieter.mumm@nist.gov
- NG-6: J. Nico, 4663, nico@nist.gov

Theory and modeling:
- J. E. Curtis, 3959, joseph.curtis@nist.gov
- T. Yildirim, 6228, taner@nist.gov

INSTRUMENTS UNDER DEVELOPMENT:

vSANS instrument:
- J. G. Barker, 6732, john.barker@nist.gov
- C. G. Glinka, 6242, charles.glinka@nist.gov

CANDOR, White-beam reflectometer/diffractometer:
- F. Heinrich, 4507, frank.heinrich@nist.gov
- C. F. Majkrzak, 5251, charles.majkrzak@nist.gov

NIST Center for Neutron Research Contacts

Copies of annual reports, facility information, user information, and research proposal guidelines are available electronically.

Please visit our website: http://www.ncnr.nist.gov

FOR A PAPER COPY OF THIS REPORT:

Steve Kline
301-975-6243
steven.kline@nist.gov

FOR GENERAL INFORMATION ON THE FACILITY:

Rob Dimeo
301-975-6210
robert.dimeo@nist.gov

Dan Neumann
301-975-5252
dan.neumann@nist.gov

FOR INFORMATION ON VISITING THE FACILITY AND/OR USER ACCESS QUESTIONS:

Julie Keyser
301-975-8200
julie.keyser@nist.gov

Mary Ann FitzGerald
301-975-8200
maryann.fitzgerald@nist.gov

For information on performing research at the facility:

Bill Kamitakahara
301-975-6878
william.kamitakahara@nist.gov

FACILITY ADDRESS:

NIST Center for Neutron Research
National Institute of Standards and Technology
100 Bureau Drive, Mail Stop 6100
Gaithersburg, MD 20899-6100 USA

NIST CENTER FOR NEUTRON RESEARCH
National Institute of Standards and Technology
100 Bureau Drive, MS 6100
Gaithersburg, MD 20899-6100

www.ncnr.nist.gov